Osaka University Knowledge Archive

Title	Structure and function of copper-containing nitrite reductases from thermophilic denitrifiers
Author(s)	福田, 庸太
Citation	大阪大学, 2014, 博士論文
Version Type	VoR
URL	https://doi.org/10.18910/34468
rights	
Note	

Osaka University Knowledge Archive : OUKA

https://ir.library.osaka-u.ac.jp/

Osaka University

Doctoral Dissertation

Structure and function of copper-containing nitrite reductases from thermophilic denitrifiers

FUKUDA Yohta

January 2014

Department of Applied Chemistry

Graduate School of Engineering

Osaka University

Preface

The studies presented here have been carried out under the direction of Professor Tsuyoshi Inoue from April 2011 to March 2014 at Department of Applied Chemistry, Graduate School of Engineering, Osaka University.

The object of the thesis is the structure-function relationship of copper-containing nitrite reductases from thermostable bacteria.

FUKUDA Yohta

Department of Applied Chemistry
Graduate School of Engineering
Osaka University
Suita, Osaka
Japan

January 2014

Contents

Introduction

0.1 Copper and organisms 1

0.2. Copper-containing nitrite reductase 2

0.3. Type 2 copper enzymes 5

Chapter 1

Atomic resolution structure of GkNIR and structural insights into protein-protein electron transfer

1.1. Introduction 11

1.2. Methods

1.2.1. Cloning, expression, and purification of CuNIR and Cyt c_{551} 13

1.2.2. Construction and preparation of the *Gk*NIR Mutants 16

1.2.3. X-ray crystallography 16

1.2.4. Stopped-Flow Kinetics 21

1.3. Results and discussion

1.3.1. Atomic resolution structure of the copper centers of *Gk*NIR 21

1.3.2. The unique N-terminal structure is involved in protein-protein electron transfer 30

Chapter 2

Structural insights into the nitrite reduction of GtNIR

2.1. Introduction 39

2.2. Methods

2.2.1. Expression and purification of WT *Gt*NIR and the C135A mutant 43

2.2.2. Crystallization of *Gt*NIR 45

2.2.3. X-ray diffraction data collection, phasing, and refinement 45

2.3. Results

2.3.1. The copper centers in *Gt*NIR 50

2.3.2. Accessibility of solvent molecules to the T2Cu site 55

2.3.3. Tight hydrogen bond networks around the T2Cu site 57

2.4. Discussion

2.4.1. The rigid and compacted catalytic site in *Gt*NIR compels the unique η^1-O nitrito Cu complex 60

2.4.2. The role of His244cat in the reaction mechanism 62

2.4.3. The flow of protons required for nitrite reduction 64

Chapter 3

High-temperature and High-resolution X-ray crystallography of GtNIR

3.1. Introduction 73

3.2. Methods 74

3.3. Results

3.3.1. High-temperature structure of WT *Gt*NIR 76

3.3.2. High-temperature structure of the C135A-nitrite complex 78

3.4. Discussion 79

Chapter 4

Do copper-containing nitrite reductases dream of peptidylglycine α-hydroxylating monooxygenase?

4.1. Introduction 82

4.2. Methods

4.2.1. Expression and purification of WT *Gt*NIR and the H294M mutant 86

4.2.2. Microspectroscopy 86

4.2.3. EPR Spectroscopy 86

4.2.4. Crystallization, X-ray diffraction data collection, phasing, and refinement 87

4.3. Results

4.3.1. Microspectroscopic analysis 88

4.3.2. The X-ray crystal structures of WT and H294M 90

4.3.3. EPR spectroscopy 93

4.4. Discussion

4.4.1. Side-on oxygen species was trapped on the T2Cu atom during X-ray irradiation and visualized by the crystallographic method 95

4.4.2. A comparison of the mutated T2Cu site in H294M with the Cu_M site in PHM 98

4.4.3. Can CuNIRs be utilized for a mold of a novel copper enzyme? 99

Conclusion 104

List of publications 106

List of supplementary publications 107

Acknowledgements 108

Structure and function of copper-containing nitrite reductases from thermophilic denitrifiers

Introduction

0.1 Copper and organisms

Long, long—three billion or more years—ago, the first photosynthetic organisms, which is considered to be cyanobacteria, were born on the Earth. It drove precipitation of iron on the bottom of the ocean in forms of iron ores, because oxygen produced by photosynthetic bacteria oxidized Fe(II) to Fe(III), which can easily form insoluble iron hydroxide ($Fe(OH)_3$) (1). Iron was doubtlessly important element for primitive organisms as it is for modern living systems because it acted and acts as a practical redox center. Thus, after the amount of available iron ions decreased, nature had to find out an alternative metal element. She, finally, did. Now, copper is one of the most ubiquitous transition metal elements in living systems. It has been adopted by all three biological domains, archaea, bacteria, and eukaryote, in the form of copper-containing proteins that take part in various essential processes such as electron transfer, oxygen transfer, and redox reactions of a variety of substrates (2, 3). Recently, some researchers have raised the hypothesis that cumulative heavy metal ions including copper ions in a brain cause Alzheimer's disease because they can induce accumulation of beta amyloid (4). Therefore, the chemistry involved in copper-organism relationships attracts rising attention more and more.

The reason why copper-containing proteins are widely utilized by living systems is that copper shows a broad spectrum of electronic states, Cu(I), Cu(II), Cu(III) in organisms. The changes in electronic states of the copper center are closely related to the structural changes in amino acid residues around the copper center. Therefore, it is essential to the

study of copper-containing proteins to precisely observe slight structural changes of residues especially in the first and second coordination spheres. Besides, copper-containing enzymes undergo the structural changes when they form enzyme-substrate complexes. In this study, one of the strongest method to directly visualize the structures of proteins, X-ray crystallography, was used. Moreover, spectroscopic analysis utilized in this study can sensitively detect the change in electronic states of copper atoms.

0.2. Copper-containing nitrite reductase

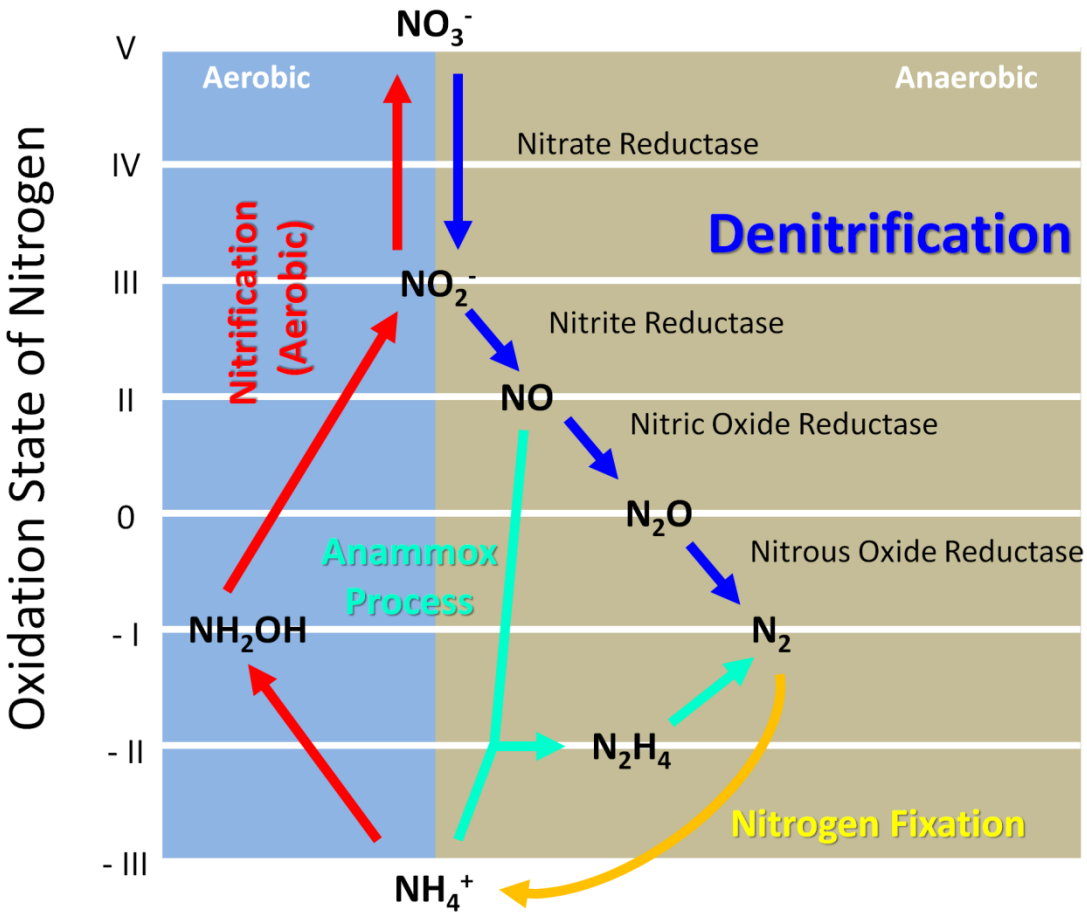

Figure 1. The nitrogen cycle mediated by organisms.

INTRODUCTION

Denitrification is a part of the geobiochemical nitrogen cycle and is the process by which some organisms (denitrifier) couple the respiratory system to the gradual reduction of nitrate or nitrite (NO_3^- or NO_2^-) to gaseous dinitrogen (N_2) via the respective formation of nitric oxide (NO) and nitrous oxide (N_2O) (Figure 1) (5). Due mainly to the invention of the Haber-Bosch process, the amount of nitrogen oxides contained in soils and waters have been increasing enough that the balance of the nitrogen cycle is at stake (6, 7). Additionally, denitrifier has been applied in the industrial field to remove nitrogen oxides in polluted water bodies (8). Denitrification is, therefore, attracting attention because of its potential agronomic, environmental, and industrial impacts.

Each step of denitrification is catalyzed by a distinct metal-containing reductase, the structures of which have been elucidated at an atomic level. Despite the global contribution of the denitrification process in thermophiles as well as mesophilic organisms and its potential industrial application, little attention has been paid to enzymes originating from thermophilic denitrifiers (9). In fact, the crystal structure of only one enzyme has been elucidated to date: a nitric oxide reductase from the thermophilic bacterium, *Geobacillus stearothermophilus* (10).

This study is focusing on dissimilatory nitrite reductase, which catalyses the one-electron reduction of NO_2^- to NO ($NO_2^- + 2H^+ + e^- \rightarrow NO + H_2O$), a key reaction in denitrification as the nitrogen compound is changed from an ionic state to a gaseous molecule, which is a precursor of nitrous oxide (N_2O), an ozone-depletion gas with the strong greenhouse effect. There are two types of nitrite reductase. The one is iron-containing nitrite reductase (*cd*$_1$-NIR), which has a homodimeric β-propeller structure containing one cytochrome *c* and one cytochrome *d*$_1$ cofactor per monomer (11). The other is copper-containing nitrite reductase (CuNIR), which is a homotrimeric

enzyme having one type 1 (T1Cu) and one type 2 Cu (T2Cu) site per monomer (Figure 2) (12). The T1Cu atom is coordinated by four amino acid residues (two histidine residues, cysteine and methionine) and functions as a receptor site for the electron supplied by an electron-donor protein such as *c*-type heme-containing cytochrome or blue-copper proteins. The T2Cu site is a catalytic center composed of three histidine residues and an axial ligand water molecule. The two Cu sites are spaced ~12.5 Å away from each other but are connected through adjacent residues, that is, cysteine and histidine, which are the ligands of the T1Cu and T2Cu centers, respectively. Such a structure enables efficient intramolecular electron transfer (ET) from the T1Cu center to the T2Cu center.

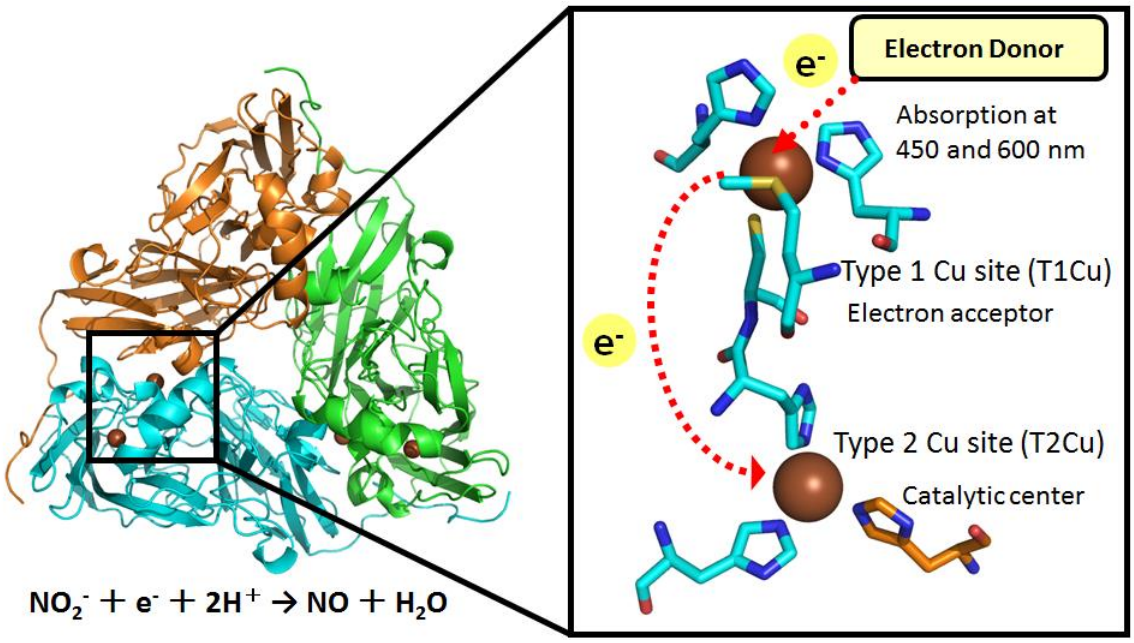

Figure 2. The trimeric structure of a typical CuNIR (from *Achromobacter xylosoxidans*, *Ax*NIR PDB code 1OE1) and its copper centers.

Additionally, CuNIR is known to catalyze the two-electron reduction of dioxygen to hydrogen peroxide (13). Production of hydrogen peroxide results in its own inactivation, but the activity is kept by addition of catalase, which decomposes hydrogen peroxide. While the mechanism of the nitrite reduction in CuNIR has been extensively studied by

determining the crystal structures of CuNIR:NO_2^- and CuNIR:NO complexes (14, 15), the detailed mechanism of the oxygen reduction is unknown because Cu-O_2 complexes decompose so readily that their visualization has been difficult to obtain.

0.3. Type 2 copper enzymes

Copper-binding sites in proteins are generally fall into three groups, type 1, type 2 and type 3 copper (16). The type 3 Cu site, which is the dinuclear centers and thus EPR silent, does not appear in this thesis. The type 1 Cu site (T1Cu) consists of two histidines, one cysteine, and typically one methionine. It shows an intense absorption band near 600 nm and relatively weak one near 450 nm due to the charge-transfer transition from the ligand cysteine S atom to Cu (II) (17). The type 2 Cu site (T2Cu) is three to four coordinate and one or more of the Cu ligands are imidazole side chains of histidines (Figure 3). When molecular oxygen (O_2) binds to the T2Cu centres, they act as oxidases or oxygenases. In other cases, T2Cu centres can perform the dismutation of superoxide and reduce nitrite (NO_2^-) to nitric oxide (NO). It is interesting that despite substrates of reactions are different from each other, those reactions can occur at similar, if not identical, T2Cu (18). During the past few decades, de novo design of metalloenzymes has attracted much attention because this technique not only allows the reproduction of essential reactions in nature, but also provides novel reactions which do not normally take place in living systems (19). The first step toward achieving artificial enzymes which catalyze intended reactions is to reveal why similar catalytic sites can function much differently from each other.

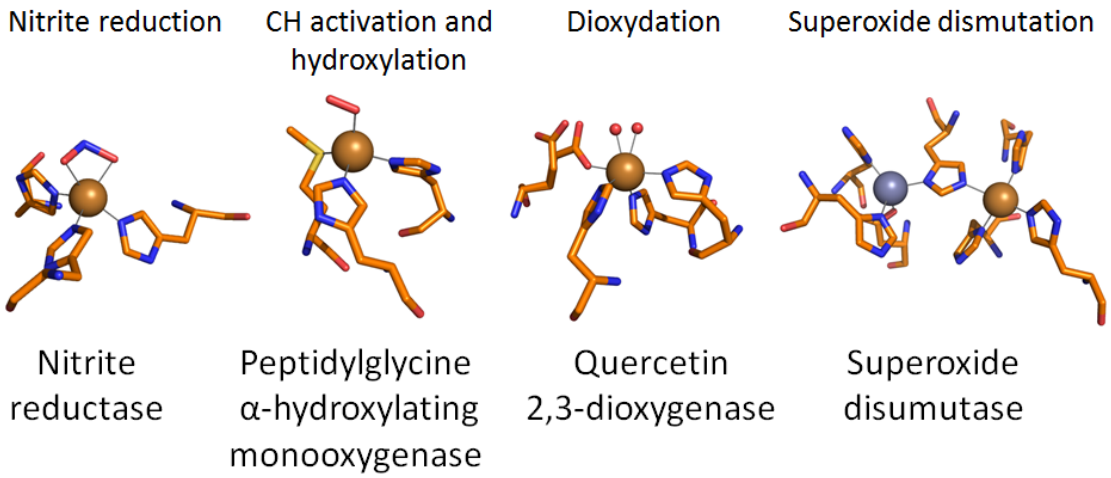

Figure 3. The specimen of T2Cu-containing enzymes. Nitrite reductase (PDB code 1SJM), peptidylglycine α-hydroxylating monooxygenase (PDB code 1SDW), quercetine 2,3-dioxygenase (PDB code 1JUH), superoxide disumutase (PDB code 2SOD)

Because CuNIR contains T2Cu, it is classified into the large copper enzyme family called T2Cu-containing enzyme. As described above, CuNIR is thought to interact with dioxigen; however, a dioxygen molecule functions as an inhibitor of CuNIR. On the other hand, it plays another role in a small class of T2Cu-containing monooxygenases such as peptidylglycine α-hydroxylating monooxygenase (PHM) and dopamine β-monooxygenase (DβM) (20). These mononuclear-copper oxygenases catalyze the activation of dioxigen to abstract a hydrogen atom on a carbon atom of a substrate to yield imperative chemicals associated with neurotransmission and behavioral development. These monooxygenases contain two non-coupled T2Cu sites, namely, the Cu_H and Cu_M site (21). The Cu_H site is composed of three histidyl residues and is thought to be the electron-acceptor center. The Cu_M site, the catalytic site, is ~11 Å away from the Cu_H site without direct connection such as peptide bond; thus, two copper sites have no electronic coupling. The structure of the Cu_M site is slightly different from the T2Cu site in CuNIR. It is coordinated by two histidyl residues and one methionyl

residue and one water molecule in a resting state. Although all members of the monooxygenase family of PHM and DβM have a methionine ligand at the Cu_M site, the function of it unfortunately remains controversial and one of the main topics of studies. In the crystal structure of PHM equipped with a substrate and a dioxygen species, dioxigen was found to bind to the Cu_M site in an end-on manner (22). However, both oxygen atoms were too distant from the C^{α} atom in the substrate to abstract the hydrogen atom. Therefore, the oxygen molecule is thought to change its direction on the Cu_M site. Theoretical chemistry predicted that a superoxo-Cu(II) complex is one of the intermediate of the reaction and it can adopt the side-on binding mode as well as the end-on manner (23). Although the side-on superoxide bound to the mononuclear copper center has not yet been observed in protein crystal structures, the recently-reported structure of PHM with hydrogen peroxide shows its side-on binding mode (23). Despite intensive efforts, the detailed mechanisms of PHM and DβM have been ambiguous.

In this thesis, following topics are discussed. In chapter 1, a crystal structure of CuNIR from *Geobacillus kaustophilus* (*Gk*NIR) was determined at an atomic resolution and a comparison of it with other known CuNIR was carried out. Especially, a unique N-terminal structure was found to be deeply involved in a protein-protein electron transfer reaction between *Gt*NIR and its physiological electron donor protein. In chapter 2, a crystal structure of CuNIR from *Geobacillus thermodenitrificans* (GtNIR) in complex with nitrite was determined and it was revealed that nitrite adopt an η^1-O monodentate binding mode to the T2Cu, which was different from an η^2-O,O bidentate binding mode observed in other CuNIRs. Chapter 3 is about a novel X-ray crystallographic method, high-temperature and high-resolution X-ray crystallography

for studies on thermostable proteins. This new technique was applied to *Gt*NIR to investigate dynamics of protein structures at high temperature, which is closer to thermophilic *Geobacillus*'s physiological environment. The high-temperature complex structure of *Gt*NIR with nitrite showed that nitrite bound to the T2Cu atom in the similar manner as that observed other CuNIRs. Chapter 4 is composed of two topics. First, the high-resolution complex structure of *Gt*NIR with an oxygen molecule was determined. Although the ability of CuNIR to reduce oxygen and the inhibitory effect of oxygen molecules on the activity of CuNIR were discovered more than 30 years ago, oxygen species bound to the T2Cu atom in CuNIR is visualized for the first time in this study. Second, the mutant CuNIR (H294M) was constructed, in which one of the three histidyl ligands of T2Cu is substituted with methionine in imitation of Cu_M in PHM. The high-resolution structure and EPR parameters of H294M suggested that modified T2Cu shared striking similarities with Cu_M in terms of geometry and electronic state, which indicates that methionine is essential to activation of oxygen at the Cu_M site. These results will supply a new foundation for creating a novel artificial copper enzyme.

References

1. Williams R. J. P., Fraústo da Silva J. J. R. (2006) The Chemistry of Evolution: The Development of our Ecosystem. The Netherlands: Elsevier BV. pp 253–262.
2. Ridge, P. G., Zhang, Y. & Gladyshev, V. N. (2008). Comparative Genomic Analyses of Copper Transporters and Cuproproteomes Reveal Evolutionary Dynamics of Copper Utilization and Its Link to Oxygen. *PLoS ONE* **3**, e1378.
3. Andreini, C., Banci, L., Bertini, I. & Rosato, A. (2008). Occurrence of Copper Proteins through the Three Domains of Life: A Bioinformatic Approach. *The Journal of Proteome Research* **7**, 209–216.
4. Kepp, K. P. (2012). Bioinorganic chemistry of Alzheimer's disease. *Chem Rev* **112**,

5193-239.

5. Zumft, W. G. (1997). Cell biology and molecular basis of denitrification. *Microbiol. Mol. Biol. Rev.* **61**, 533-616.
6. Gruber, N. & Galloway, J. N. (2008). An Earth-system perspective of the global nitrogen cycle. *Nature* **451**, 293-6.
7. Galloway, J. N., Townsend, A. R., Erisman, J. W., Bekunda, M., Cai, Z., Freney, J. R., Martinelli, L. A., Seitzinger, S. P. & Sutton, M. A. (2008). Transformation of the Nitrogen Cycle: Recent Trends, Questions, and Potential Solutions. *Science* **320**, 889-892.
8. De Lucas, A., Rodriguez, L., Villasenor, J. & Fernandez, F. J. (2005). Denitrification potential of industrial wastewaters. *Water Res* **39**, 3715-26.
9. Vries, S. d. & Schröder, I. (2008). *Thermophiles: Biology and Technology at High Temperatures*, CRC Press Boca Raton, Florida.
10. Matsumoto, Y., Tosha, T., Pisliakov, A. V., Hino, T., Sugimoto, H., Nagano, S., Sugita, Y. & Shiro, Y. (2012). Crystal structure of quinol-dependent nitric oxide reductase from Geobacillus stearothermophilus. *Nat Struct Mol Biol* **19**, 238-45.
11. Williams, P. A., Fülöp, V., Garman, E. F., Saunders, N. F. W., Ferguson, S. J. & Hajdu, J. (1997). Haem-ligand switching during catalysis in crystals of a nitrogen-cycle enzyme. *Nature* **389**, 406-412.
12. Suzuki, S., Kataoka, K. & Yamaguchi, K. (2000). Metal Coordination and Mechanism of Multicopper Nitrite Reductase. *Acc. Chem. Res.* **33**, 728-735.
13. Kakutani, T., Beppu, T. & Arima, K. (1981). Regulation of Nitrite Reductase in the Denitrifying Bacterium Alcaligenes faecalis S-6. *Agric. Biol. Chem.* **45**, 23-28.
14. Tocheva, E. I., Rosell, F. I., Mauk, A. G. & Murphy, M. E. (2004). Side-on copper-nitrosyl coordination by nitrite reductase. *Science* **304**, 867-870.
15. Antonyuk, S. V., Strange, R. W., Sawers, G., Eady, R. R. & Hasnain, S. S. (2005). Atomic resolution structures of resting-state, substrate- and product-complexed Cu-nitrite reductase provide insight into catalytic mechanism. *Proc Natl Acad Sci U S A* **102**, 12041-12046.
16. Solomon, E. I., Sundaram, U. M. & Machonkin, T. E. (1996). Multicopper Oxidases and Oxygenases. *Chemical Reviews* **96**, 2563–2605.
17. Solomon, E. I., Baldwin, M. J. & Lowery, M. D. (1992). Electronic Structures of Active Sites in Copper Proteins: Contributions to Reactivity. *Chem Rev* **92**, 521-542.
18. MacPherson, I. S. & Murphy, M. E. (2007). Type-2 copper-containing enzymes. *Cell Mol Life Sci* **64**, 2887-99.
19. Lu, Y., Yeung, N., Sieracki, N. & Marshall, N. M. (2009). Design of functional

metalloproteins. *Nature* **460**, 855-62.

20. Itoh, S. (2006). Mononuclear copper active-oxygen complexes. *Curr Opin Chem Biol* **10**, 115-22.
21. Prigge, S. T., Kolhekar, A. S., Eipper, B. A., Mains, R. E. & Amzel, L. M. (1997). Amidation of Bioactive Peptides: The Structure of Peptidylglycine -Hydroxylating Monooxygenase. *Science* **278**, 1300-1305.
22. Prigge, S. T., Eipper, B. A., Mains, R. E. & Amzel, L. M. (2004). Dioxygen binds end-on to mononuclear copper in a precatalytic enzyme complex. *Science* **304**, 864-7.
23. Chen, P. & Solomon, E. I. (2004). O2 activation by binuclear Cu sites: noncoupled versus exchange coupled reaction mechanisms. *Proc Natl Acad Sci U S A* **101**, 13105-10.
24. Rudzka, K., Moreno, D. M., Eipper, B., Mains, R., Estrin, D. A. & Amzel, L. M. (2013). Coordination of peroxide to the Cu(M) center of peptidylglycine alpha-hydroxylating monooxygenase (PHM): structural and computational study. *J Biol Inorg Chem* **18**, 223-32.

Chapter 1

Atomic resolution structure of *Gk*NIR and structural insights into protein-protein electron transfer

Summary

The crystal structures of copper-containing nitrite reductase (CuNIR) from the thermophilic Gram-positive bacterium *Geobacillus kaustophilus* HTA426 and its mutant in which the N-terminal 37 residues were deleted were determined at resolutions of 1.04 Å and 1.77 Å, respectively. Both structures show a striking resemblance with the overall structure of the well-known CuNIRs composed of two Greek key ß-barrel domains; however, a remarkable structural difference was found in the N-terminal region. The unique region extended to the northern surface of the type-1 copper site. The superposition of the *Gk*NIR model on the complex structure of CuNIR with the electron-transfer partner, cytochrome *c*551, in other denitrifier indicated that this region contributes to the transient binding of *Gk*NIR with the partner protein during the interprotein electron-transfer reaction. Furthermore, electron-transfer kinetics experiments using N-terminal residue-deleted mutants and the redox partner, *Geobacillus* cytochrome *c*551, were carried out. These structural and kinetics studies demonstrate that that region is directly involved in the specific partner recognition.

1.1. Introduction

Copper-containing nitrite reductase (CuNIR) is one of two dissimilarly nitrite reductases on the earth (The other is iron-containing nitrite reductase housing *c*- and

d$_1$-type cytochromes). It is responsible for one electron reduction of NO_2^- to NO ($NO_2^- + 2H^+ + e^- \rightarrow NO + H_2O$) in the denitrification process where nitrogen oxides are reduced to dinitrogen ($NO_3^- \rightarrow NO_2^- \rightarrow NO \rightarrow N_2O \rightarrow N_2$), and typically shows a homotrimeric structure containing one T1 and one T2 Cu site per monomer (1). Recent genomic analyses have revealed that a wide variety of microorganisms is involved in denitrification and has *nirK* gene encoding CuNIR. Some of these CuNIRs show unique structures with extra domains including blue copper domain, *c*-type cytochrome domain and transmembrane helices (2, 3). *Geobacillus* including *Geobacillus kaustophilus* HTA426 is a genus of extremophilic gram-positive bacterium and several species in it are denitrifiers which have *nirK* gene in their genomes (4, 5). Amino acid sequences of CuNIR from genus *Geobacillus* show high similarity to each other (80-95%). On the other hand, the sequences show low similarities (20-40%) to other CuNIRs, albeit the conserved residues related to Cu-binding and enzymatic functions. This indicates that *Geobacillus* CuNIR can perform nitrite reduction but has a unique structure. A ClustalW alignment analysis (Thompson *et al.*, 1994) between *Gk*NIR, *Achromobacter xylosoxidans* CuNIR (*Ax*NIR; 19% identity to *Gk*NIR) (6) and *Neisseria gonorrhoeae* CuNIR (*Ng*NIR; 27% identity to *Gk*NIR) (7) reveals amino acid deletion and insertion in *Gk*NIR (8). Moreover, though every previously determined CuNIR has isoleucine (Ile) which is highly conserved above the T2 Cu, controls the binding mode of and selects substrate, it is substituted by valine (Val) in *Gk*NIR. While there are previous studies where the conserved Ile was replaced with Val (9-11), there is no case that CuNIR, Ile of which is naturally substituted with Val, is analysed in detail.

Here, the crystal structure of *Gk*NIR at a resolution of 1.04 Å is reported. This is not only the first CuNIR structure from a thermophilic organism but also the first one from

a gram-positive bacterium. The substantially higher resolution allows precise refinement of the Cu site structures including H atoms. The contribution of weak hydrogen bonds such as CH-O, CH-π, NH-π hydrogen bonds to the structure of Cu centres will be discussed circumstantially using revealed positions of H atoms. In addition, the differences between *Gk*NIR and other CuNIRs are investigated in reference to spectroscopic data. The relatively large space and unusual electron density observed above the T2 Cu implies the possibility of easily binding of molecules other than nitrite to the T2 Cu and some reaction can occur there. Thus, the present structure may provide information about the common properties of T2 Cu-containing enzymes. Moreover, the unique N-terminal structure of *Gk*NIR at near the T1Cu site is investigated. Using stopped-flow kinetics with the cognate cytochrome c_{551} (*Gk*Cyt c_{551}) as a possible redox-partner for *Gk*NIR, it has been demonstrated that the N-terminal region of *Gk*NIR greatly contributes to the partner recognition during the interprotein ET reaction between *Gk*NIR and *Gk*Cyt c_{551}.

1.2. Methods

1.2.1. Cloning, expression, and purification of CuNIR and Cyt c_{551}

The *nirK* gene from *G. kaustophilus* HTA426 was previously cloned into the pET-20b (+) vector (Merck) between the *Nde*I and *Hin*dIII restriction sites. Moreover, the *nirK* gene from *Achromobacter xylosoxidans* GIFU1051 was cloned into the pMal-c2x vector (New England Biolab) between the *Xmn*I and *Bam*HI restriction sites. Their expression and purification protocols were the same to the procedures described previously.

The gene encoding the putative soluble region (between residues Ala26 and Lys111 of GK3102) annotated with the cytochrome *c*551 gene was amplified by PCR using the

genomic DNA of *G. kaustophilus* HTA426 as the template. The N-terminal region from Met1 to Asn25 was predicte to act as a signal peptide for secretion by using the amino acid sequence-based predictor server SignalP4.1 (http://www.cbs.dtu.dk/services/SignalP/). Moreover, the lipobox motif (12) for the lipid-modified cysteine site (L16AAC19), functioning as an anchor into the cell membrane, was also found in this region. In this study the N-terminal region was replaced with the *pelB* leader peptide from the pET-20b (+) vector by genetic engineering to achieve an efficient over-production in *E. coli*. The restriction enzymes sites for *Nco*I (CCATGG) and *Hind*III (AAGCTT) sites were incorporated into the sequences of the forward and reverse primers, 5'-TTCCATGGCCGGGGAGAAAAACGACGCAGC-3' and 5'-ATAAGCTTATTTTTTCGCAGCCAGCCATTCCG-3', respectively. The DNA product fragment was cloned into pET-20b (+) opened by digestion with *Nco*I and *Hind*III. The presence of the insert was confirmed by DNA-sequence analysis. The *pelB* leader peptide (Met1 to Met23) was added before the Ala26 residue of *Gk*Cyt *c*551, and the peptide was digested before Met23 with an *E. coli* signal peptidase for secretion into the periplasm. Furthermore, the gene encoding the region from Ala27 to Arg108 of NirM (*Ax*Cyt c_{551}) from *A. xylosoxidans* GIFU1051 (13) was also amplified by PCR using the cognate genomic DNA as the template. The N-terminal region (Met1 to Pro26) was replaced with the *pelB* leader peptide from the pET-20b (+) vector to achieve an efficient over-production in *E. coli*. The restriction enzymes *Nco*I (CCATGG) and *Hind*III (AAGCTT) sites were incorporated into the sequences of the forward and reverse primers, 5'-CCCCATGGCCCAGCTCGACCCGGCCGGTGAAAA-3' and 5'-CCAAGCTTAGCGCGCGGCGTCCATCATGTAC-3', respectively. The DNA product

fragment was cloned into the pET-20b (+) opened by digestion with *Nco*I and *Hind*III. As a result, the *pelB* leader peptide from Met1 to Met23 was added before the Ala27 of AxCyt *c*551. For both Cyt *c*551 sequences, the expression strains were cotransformed with plasmid pEC86 (14). The proteins were produced in *E. coli* strain Rosetta-gami (DE3). The expression protocols were the same in both cases, and 100 μM IPTG was used for induction. For the purification of *Gk*Cyt c_{551}, the harvested cells were resuspended in 40 mM Tris-HCl buffer (pH 8.0) containing 0.5 mM phenylmethanesulfonyl fluoride. The suspension was sonicated at 160 W for 30 min, and the debris was removed by centrifugation at 15,000 rpm for 1 h at 4 ℃. Ammonium sulfate (AS) was added to 35%-saturated concentration to the supernatant, and the resulting precipitate was separated by centrifugation. The supernatant was loaded onto a Phenyl-Sepharose Fast Flow column (2.5 cm × 25 cm; GE Healthcare) pre-equilibrated with 40 mM Tris-HCl buffer (pH 8.0) containing a 35% saturated concentration of AS. After washing the column with 1 L of the same buffer, the red-colored cytochromes were eluted with a linear gradient from 35% to 0% saturated AS in the same buffer. The cytochrome-containing fractions were collected and dialyzed against 40 mM Tris-HCl buffer (pH 8.0) containing 20% AS. After removing the precipitate by centrifugation, the supernatant was loaded onto an HPLC hydrophobic Phenyl-5PW column (0.9 × 5.0 cm; Tosoh) pre-equilibrated with 40 mM Tris-HCl buffer (pH 8.0) containing 20% AS. The single hemoprotein was then eluted with a linear gradient from 20% to 0% AS. The fractions were collected, concentrated, and desalted with a Centriprep-YM3 device (Millipore). The purity, estimated by SDS-PAGE and spectrophotometrically, was observed to be >95%. In addition, AxCyt *c*551 was purified by cation exchange and hydrophobic column chromatography according to the

procedures described previously.

1.2.2. Construction and preparation of the *Gk*NIR Mutants

Two GkNiR mutants with a deletion of the N-terminal amino acid residues from 1 to 20 and 1 to 37, ⊿1-20 and ⊿1-37, were constructed. They were obtained by a PCR method using the following primers; 5'- TACATATGCACAAAAGGGGTGAATCAAGCACCGG-3' for ⊿1-20 and 5'- TACATATGCCTCATGATGTCCACATCGAAATGACA-3', for ⊿1-37. The reverse primers for the PCRs were the same as those used in a previous report detailing the construction of WT GkNIR. The PCR products of two mutants were digested with *Nde*I and *Hin*dIII, and then cloned into the expression vector pET20-b (+) opened by digestion with the same restriction enzymes. The expression and purification protocols were the same for WT *Gk*NIR.

1.2.3. X-ray crystallography

*Gk*NIR crystals were grown in hanging drops consisting of 2μl protein solution (100 mg ml^{-1}) and 2 μl well solution and the drops were equilibrated against 0.3 ml well solution (0.1 M acetate buffer pH 4.6, 5.5% (w/v) PEG 4000 and 150 mM $CuSO_4$) at 293 K. The approximate dimensions of the *Gk*NIR crystals were 0.5 x 0.3 x 0.2 mm^3. Greenish-blue crystals separated out after one day at 289 K. For data collection at 100 K, the crystals were flash-frozen in liquid nitrogen after being moved into a reservoir solution supplemented with 35% (w/v) 2-methyl-2,4-pentanediol as a cryoprotectant. Diffraction data sets were collected from the *Gk*NIR crystal on beamline 44XU of SPring-8 (Japan Synchrotron Radiation Research Institute, Hyogo, Japan) using a radiation wavelength of 0.9 Å and a Bruker DIP-6040 detector system. Diffraction data were collected from

three positions of a single crystal; that is, after one data collection, the crystal was translated by 0.05 mm along the spindle axis and the next collection was started. Crystal-to-detector distance was kept 90 mm so that diffraction spots could be recorded up to 1.03 Å resolution. 90 frames of diffraction images were collected from each position with an oscillation range of 1° and an exposure time of 1.5 s per frame. Besides, to cover the entire range of intensities, the middle and low-resolution data were collected differing crystal-to-detector distances (180 mm and 360 mm with corresponding highest possible resolutions of 1.60, and 2.92 Å, respectively) and positions exposed by X-rays with an oscillation range of 1° and an exposure time of 1 s per frame. When middle and low-resolution images were collected, aluminum attenuator (0.8 and 1.7 mm in thickness, respectively) was used to reduce X-rays. The X-ray beam size was 0.05 x 0.05 mm, which was smaller than the crystal size. The data were processed with the HKL program suite (15). The highest resolution of 1.04 Å was chosen on the basis of the criteria that more than 85 % of reflections in the highest shell satisfied $I/\sigma(I) > 2$ and the average $I/\sigma(I)$ was greater than 2.0 for all reflections in the shell. The crystal belonged to space group $R3$, with a *Gk*NIR molecule per asymmetric unit. The crystal structure was determined by molecular replacement using the program MOLREP (16) from the CCP4 suite (17). The *Gk*NIR structure of 1.30 Å resolution structure determined in the previous study (8) was used as the search model after first omitting Cu, Zn, Na, waters and multiple conformations of the side chains which could differ between the two proteins. The *Gk*NIR model was subject to a cycle of positional and individual B-factor refinement in REFMAC using data from 64.74 to 1.50 Å. This yielded an *R*-factor of 20.2% (*R*-free 21.6%). The model consisted of 2565 protein atoms, seven Cu atoms and nine Na atoms. Manual model building of the molecule was

carried out using COOT (18) thorough the refinement process. After 20 refinement cycles in REFMAC and the inclusion of a total of 452 water molecules the R-factor was reduced to 15.0% (R_{free} 16.4%) at 1.04 Å resolution. At this point anisotropic refinement in REFMAC was carried out. This reduced the R-factor to 12.1% (R-free 13.6%) with a total of 469 water molecules included. This model was further refined using SHELX97 (19). When moving from REFMAC to SHELX, all the water molecules, Na atoms and alternative conformations was removed and anisotropic parameters were changed into isotropic ones. After 20 cycles of conjugate-gradient least squares refinement with isotropic thermal parameters, the model was thoroughly examined for possible errors using $2m|F_o| - D|F_c|$ ($2F_o$-F_c) (1.5 σ) and $|F_o| - |F_c|$ (F_o-F_c) (±3.0 σ) difference maps. Water molecules were added to the model using the automated water-searching program built into COOT and were then further refined. Progress was made with conjugate-gradient anisotropic refinement using six-parameter anisotropic displacement parameters with bond-length, bond-angle, planarity, chirality and antibumping restraints. The copper coordination geometry was not restrained. The occupancies (0.2-0.8) of the atoms modelled in two or three alternative conformations were determined based on agreement with electron density map and in reference to the result of occupancy refinement using PHENIX (20). The final values of R_{work} and R_{free} for the model with implemented riding H atoms were 8.85% and 10.5%, respectively, for 157 240 reflections with $|F_o| > 4\sigma(F_o)$ and were 10.3% and 12.1%, respectively, for all 189,861 reflections in the working data set. The final model was checked for stereochemical quality using PROCHECK (21) and MolProbity (22). Data-collection and refinement statistics are summarized in Table I-I.

Table I-I. Data collection and refinement statistics for *Gt*NIR WT, C135A-NO_2, and WT-formate

	WT	Δ 1-37
Data collection		
Synchrotron beamline	SPring-8 BL44XU	SPring-8 BL44XU
Wavelength (Å)	0.9	0.9
Space group	*R*3	$P2_1$
Unit cell		
a, b, c (Å)	115.3, 115.3, 85.0	89.3, 165.0, 126.6
α, β, γ (°)	90, 90, 120	90, 126.6, 90
Resolution range (Å)	64.74-1.04 (1.06-1.04)[a]	124.7-1.77 (1.80-1.77)
R_{merge} (%)[b]	9.7 (49.4)	8.0 (56.0)
Completeness (%)	98.7 (89.3)	98.6 (98.4)
Unique reflections	141,618 (6786)	30,251 (1461)
$<I/\sigma(I)>$	37.9 (2.3)	25.4 (2.1)
Redundancy	3.5 (2.5)	3.3 (2.9)
Refinement		
Resolution range (Å)	22.06-1.15	25.18-1.90
No. of Reflections	134,511	28,714
R_{work} (%)[c]/ R_{free} (%)[d]	10.3/12.1	17.2/19.2
RMSD bond length (Å)	0.014	0.013
RMSD bond angle (°)	2.0	1.4
Ramachandran (%)[e]		
Favored	98.3	98.6
Allowed	1.7	1.4

[a] Values in parentheses are for the highest-resolution shell.. [b] R_{merge} is calculated as $\Sigma_{hkl}\Sigma_i | I_i(hkl)-<I(hkl)> | / \Sigma_{hkl}\Sigma_i I(hkl)$, where $I_i(hkl)$ is the intensity of an individual measurement of the reflection with Miller indices *hkl* and <I(hkl)> is the average intensity from multiple observations. [c] $R_{work} = \Sigma_{hkl} | |F_{obs}| - |F_{calc}| | / \Sigma_{hkl} |F_{obs}|$, where F_{obs} and F_{calc} are the observed and calculated structure-factor amplitudes, respectively. [d] The free *R* factor, R_{free}, is computed in the same manner as R_{work} but using only a small set (5%) of randomly chosen intensities that were not used in the refinement of the model. [e] MolProbity statistics (22).

The crystals of the ⊿1-37 mutant were obtained by using the hanging-drop vapor-diffusion technique. Droplets containing 10 mg/mL protein in 0.05 M HEPES-NaOH (pH 7.5) and 1.0 M ammonium formate were equilibrated over wells containing a reservoir solution [0.1 M Hepes-NaOH (pH 7.5) and 2.0 M ammonium formate]. The sample dishes were stored for crystallization in an incubator from 1 week to 1 month at 16.0 ℃. The crystals were rinsed in a cryoprotectant solution (the reservoir solution supplemented with 30.0% v/v glycerol) before flash-freezing in liquid nitrogen. The diffraction data were collected at the beamline BL44XU at SPring-8 (Hyogo, Japan) equipped with an MX225-HE detector (Rayonix). The image data were processed and scaled using the HKL package (15). The crystals of the ⊿1-37 mutant belong to the space group *P*21 with the following cell parameters: a = 89.3 Å, b = 165.0 Å, c = 126.6 Å, and β = 102.3°. The data set was 98.6% complete overall to a resolution of 1.77 Å with an R_{merge} of 8.0 %. The data processing statistics are summarized in Table I-I. The structure was determined through molecular replacement using the model of wt *Gk*NIR model as a search model after omitting the N-terminal region. MOLREP gave a unique solution, which was rigid-body refined using CNS (23). Three trimer molecules (i.e., 9 monomeric subunits) were found in the asymmetric unit, and the resulting initial model gave an R_{factor} of 36% at a resolution of 2.5 Å after rigid-body refinement and minimization. Several stages of refinement were performed using Coot and Refmac5. The model was then thoroughly examined for possible errors using both maps at contour levels of 1.2 σ ($2F_O - F_C$) and ±3.5 σ ($F_O - F_C$). The structure was refined to obtain R_{work} and R_{free} values of 0.17 and 0.19, respectively. The refined model was assessed using Procheck and Molprobity. The average *B*-factors for all the atoms of each monomer (chain A, B, C, D, E, F, G, H, and I) and water molecules were 24.4, 24.5, 23.8,

25.0, 24.0, 23.5, 24.7, 27.0, 25.1 and 37.5 Å^2, respectively. Some amino acid residues of the model showed slightly elevated *B*-factors and somewhat diffuse electron density. The refinement statistics are summarized in Table I-I.

1.2.4. Stopped-Flow Kinetics

Stopped-flow kinetics experiments of the ET reaction from the reduced Cyt c_{551} to CuNIR were performed in a 10 mM Tris-HCl buffer (pH 8.0) at 25°C under anaerobic conditions. To maintain pseudo-first-order conditions, the concentration ratios of CuNIR to Cyt c_{551} was always more than 10 times [CuNIR, 30 μM (as a monomer); Cyt c_{551}, 1.0 μM]. The pseudo-first-order rate constants (k_{obs}) were obtained by fitting the experimental data with a single exponential function. The kinetic traces were acquired with an RA-2000 stopped-flow spectrophotometer (Otsuka Electronics) using the single-wavelength mode of the machine.

1.3. Results and discussion

1.3.1. Atomic resolution structure of the copper centers of *Gk*NIR

The type 1 Cu atoms are buried within the N-terminal domain of the *Gk*NIR monomer and are positioned approximately 6 Å below the surface of the protein. Two histidine nitrogen atoms (His95 Nδ1 and His143 Nδ1), and two sulphur atoms, one from Cys135 (S^{γ}) and the other from Met148 (S^{δ}), coordinate the T1 Cu. Four out of three residues (Cys135, His143 and Met148) are on the same loop (C-H-M loop). The His and the Cys ligands are positioned approximately in plane with the copper atom while the weaker methionine adopts an axial coordination, so the T1 Cu site shows distorted tetrahedral geometry (Fig. 1-1). His143 is positioned on the surface, and the Nε2 atom

of it is solvent-exposed and forms a hydrogen bond (2.73 Å) with a surface water molecule. The coordination $N^{\delta 1}$ of His143 significantly deviates from the centre of T1Cu and this structure thought to be maintained by some weak interactions. One of those interactions is a CH-π hydrogen bond between Trp63 and His 143 (Fig. 1-1). The

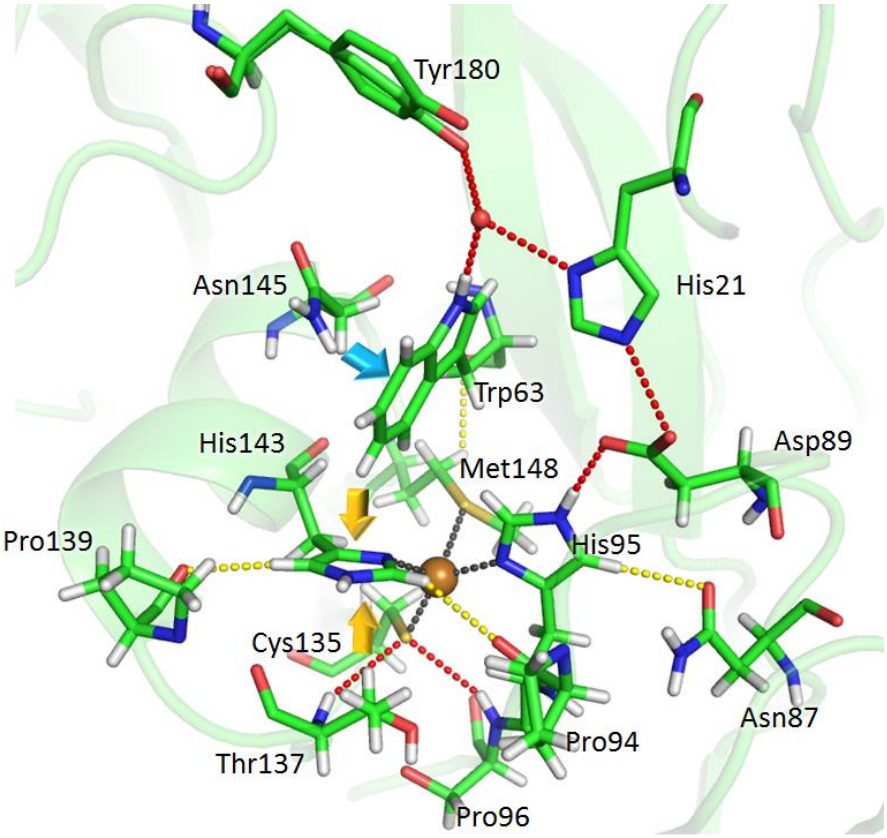

Figure 1-1. The hydrogen bond network around the T1Cu site of *Gk*NIR. Traditional and CH-O hydrogen bonds are shown as red and yellow dotted lines, respectively. CH-π and NH-π hydrogen bonds are illustrated by yellow and sky blue arrows, respectively.

existence of a CH-π hydrogen bond is supported by following structural evidence. The angle between the C^{ζ} of Trp63, the H atom on it and the foot of the perpendicular from the CH end to the imidazole plane is ~154° and the H atom on the Cζ atom in the indole ring is ~2.7 Å from the centre of the imidazole ring. These values are typical of CH-π hydrogen bonding. Likewise, the CβH of Thr137 and the π orbital of the His143

imidazole ring form a weak hydrogen bond on the other side (The angle between the Cβ of Thr137, the H atom on it and the foot of the perpendicular from the CH end to the imidazole plane is ~150° and the H atom on the C^{β} atom is ~2.9 Å from the centre of the imidazole ring). Because the first bond is shorter than the second, the first is stronger than the second.

Besides, the H atoms on the C^{δ} and C^{ε} of His143 form CH-O hydrogen bonds between the carbonyl O of Pro139 and Pro94, respectively. The distances between H and O are 2.43 and 2.48 Å, respectively. All these weak interactions must fix the geometry of His143. These interactions may exist in other CuNIRs. Especially, *Ng*NIR, *Ph*NIR and *Hyphomicrobium denitrificans* CuNIR (*Hd*NIR) (24) which are defined as class II CuNIR showing the shorter tower loop than class I, have the Trp residue above the solvent-exposed His ligand. On the other hand, class I CuNIRs such as *Ax*NIR, *Achromobacter cycloclastes* CuNIR (*Ac*NIR) (25), *Alcaligenes faecalis* CuNIR (*Af*NIR) (26) and *Rhodobacter sphaeroides* CuNIR (*Rs*NIR) (27) have the Met residue at the corresponding position and this Met, too, may control the geometry of the His ligand by non-covalent interaction. The other histidine ligand, His95, is linked by a hydrogen bond to the $O^{\delta 1}$ atom of Asp89, $O^{\delta 2}$ atom of which can form the other hydrogen bond with the $N^{\varepsilon 2}$ atom of His21 located near the N-terminal end of the determined peptide chain (Fig. 1-1). On top of that, His21 is linked to Tyr180 on the short tower loop and Trp63 above the T1Cu site via a water molecule which is a hub of the hydrogen bond network. This network is found only in *Gk*NIR, so far. The indole ring of Trp63 acts as an acceptor of H atom; that is, the NH of Asn145, which is on the C-H-M loop, forms an NH-π hydrogen bond with Trp63. Because Trp63 is involved in several interactions

which indirectly connect the Cu centre to the N-terminal region, the tower loop and the C-H-M ligand loop, it must be a key residue in an outer-sphere of the T1 Cu in *Gk*NIR.

In all the T1Cu-containing proteins, the S^{γ} atom of ligand Cys has been thought to accept one hydrogen bond from the backbone amide of the residue which is usually adjacent to the first His ligand. In the *Gk*NIR *F*o-*F*c map omitting H atoms, the electron density representing the H atom on the amide N of Ser96 next to His95 was clearly observed and it is included in the model at the distance of 2.6 Å from the S^{γ} atom of Cys135, demonstrating the existence of a hydrogen bond. In many T1 Cu containing proteins without rusticyanin and *Hd*NIR, the residue involving in this hydrogen bond is highly conserved Asn, not Ser. The O^{δ} atom in the conserved Asn forms a hydrogen bond to the backbone amide of the residue next to the ligand Cys. So does Ser in rusticyanin, *Hd*NIR and *Gk*NIR. An H atom of a hydroxyl group is so mobile that it often disorder in a protein structure and fail to be determined by X-ray crystallography. Unfortunately, the H atom on the tip of Ser96 was not observed in the *F*o-*F*c map omitting H atoms. However, the H atom on the amide N of Gly136 next to the ligand Cys was found at the distance of 2.16 Å from the O^{γ} atom of Ser96 and there may be a hydrogen bond like that observed in rusticyanin. The H atom of hydroxyl group in Ser96 therefore is thought to direct to the hydroxyl O in Thr137 (The O^{γ} of Ser96 and the O^{γ} of Thr137 is 2.87 Å apart from each other). In fact, the H atom on the O^{γ} of Thr137 is seem to be toward the carboxyl O atom in Asp112 which connects to surface waters, and consequently the O^{γ} of Thr137 can accept a hydrogen atom from Ser96. The replacement of Asn with Ser has been proposed to raise the redox potential of the T1 Cu by strengthening the interactions between two ligand-containing loops to add rigidity to these loops, influencing the direct hydrogen bonds between the backbone of the protein

and the thiolate of Cys ligand (28, 29) and modulating an electric dipole (30). Though Ser96 in *Gk*NIR may have the same function as Ser in ructicyanin, this residue is on the equivalent position to Asn90 in *Ax*NIR, which is thought to consist of one of two putative channels to relay a proton toward the T2 Cu for nitrite reduction. Thus, we will return to discussion about the function of Ser96 and a proton channel in the next section 3.3. Because the H atom on the amide N of Thr137 appears 2.7 Å away from the S^{γ} atom, there must be the second hydrogen bond (Fig. 1-1). This second hydrogen bond between Cys and the residue two after it is found in several blue copper proteins such as azurin, stellacyanin and rusticyanin. On the other hand, it is not found in some blue copper proteins including amicyanin, plastcyanin and pseudoazurin, because they have proline two after the Cys ligand. In CuNIRs structures of which have been determined, class I CuNIRs have only the first hydrogen bond while class II CuNIIRs have also the second hydrogen bond. Because of the existence of the second hydrogen bond, the distance of the first hydrogen bond in *Gk*NIR is slightly longer than in *Ax*NIR. H-bonds to a thiolate ligand can be classified into the active or the passive hydrogen bond based on the involvement of the hydrogen bond acceptor orbital in thiolate-metal bonding (31). In the active hydrogen bond, the orbital of acceptor is involved in bonding between the metal centre and the S ligand and active hydrogen bonding significantly changes the electronic property of the metal center. On the other hand, when the hydrogen bond acceptor orbital is not a thiolate donor orbital, it is passive and does not affect thiolate-metal covalency or tune reactivity. Recently, Hadt *et al.* have demonstrated the difference between active and passive hydrogen bonding to Cys thiolate coordinated to the T1 Cu. In *Gk*NIR, the first hydrogen bond is active, the second passive. Though, according to Hadt *et al.*, passive hydrogen bond is electronically less effective than

active one, the second hydrogen bond in the T1 Cu-containing protein is known for affecting the property of the T1 Cu centre such as colour, redox potential and reorganization energy during an electron transfer reaction (28, 29).

The fourth ligand of the T1Cu, Met148, represents *gauche* conformation as found in other all known CuNIRs but *Ac*NIR and *Af*NIR. Because *gauche* conformation is slightly less stable than *anti* conformation, T1 Cu-containing proteins should favour *anti* conformation in a Met residue. Azurin and amicyanin, however, house *gauche* Met at the Cu site and this has remained to be explored (32). In known CuNIRs, *gauche* conformation seems to be prevalent (6 species out of 8 contain *gauche* Met.). According to typical interpretation of the *gauche* effect, these phenomena are explained that the lone-pair electrons on the S atom interact with the σ* orbital of the $C^{\delta}C^{\gamma}$ bond to stabilize *gauche* conformation. But, why seemingly identical Met residues in CuNIRs represent two different conformations? These phenomena are probably because of stabilization of *gauche* conformation by CH-O hydrogen bonds. CH-O hydrogen bonds between the CγH of Met148 and the carbonyl O of Trp63 and between the CγH and the carbonyl O of His143 were observed in the *Gk*NIR structure. The former one is noteworthy, for superposing the *Gk*NIR structure on *Af*NIR and *Ac*NIR structures, which have *anti* conformation Met, shows that if *Af*NIR or *Ac*NIR adopts *gauche* conformation the CH-O hydrogen bond between the CγH of Met and the carbonyl O of the residue corresponding to Trp63 would not be formed due to too short distance between the CγH and the carbonyl O atom. On the other hand, all CuNIR structures which represent *gauche* conformation at the ligand Met shows the possibility of the CH-O hydrogen bond at the same position. This difference comes from the difference between backbone structures around the Met ligands. CuNIRs housing an *anti* Met

ligand is known to have bulky Tyr in the vicinity of a peptide chain containing the Met ligand, whereas the Tyr residue is replaced with other smaller residues in CuNIRs housing a *gauche* Met ligand (33). In addition, the neutron crystallography has recently shown that this CH-O hydrogen bond exists in amicyanin showing *gauche* Met (34). The energy gap between *gauche* and *anti* conformation, which is at most 5 kcal mol^{-1}, can be easily compensated with the energy of weak hydrogen bonding, which is typically more than -10 kcal mol^{-1}.

T1Cu-containing proteins that have the same Cys, two His, and Met ligand set vary from blue to green. In contrast to *Ax*NIR which have very little absorption at about 450 nm in their UV/Vis spectra, *Af*NIR, *Ac*NIR and *Rs*NIR show increased absorbance at about 450 nm and green color. *Gk*NIR shows an intermediate colour between blue and green. The spectroscopic analysis can be coupled with the crystallographic one to investigate the relation between the intensity ratio of the 450 and 600 nm bands in the optical spectrum of a T1Cu site and the value of the dihedral angle, θ, between the S(Met)-Cu-S(Cys) plane and the plane containing the N(His)-Cu-fourth ligand (35, 36). When correlation plots between the absorption ratios ($\varepsilon_{450}/\varepsilon_{600}$) and the θ values and between the θ values and the distance ratios of S(Met)-Cu to S(Cys)-Cu are depicted, *Gk*NIR is located about midway between blue proteins and green ones. This result demonstrates the good agreement between the present crystal structure model and the spectroscopic data. Though conformation of the axial Met has been thought to be involved in a colour of the T1 Cu in CuNIR, the difference in conformation (*gauche* or *anti*) is not essential to a colour of the T1 Cu centre, because blue *Ax*NIR, green *Rs*NIR and greenish-blue *Gk*NIR, all adopt *gauche* conformation. What is more important is the overall structure of the T1 Cu made of a lot of weak interactions. It has been known

that a single weak hydrogen bond or non-covalent interaction in the outer-sphere of the T1 Cu contributes to the geometry and the property of the T1 Cu centre (37, 38), the present *Gk*NIR structure indicates that the interaction network around the T1 Cu is involved in many weak hydrogen bonds such as CH-π, CH-O and NH-π hydrogen bonds and thus more complicated than ever thought.

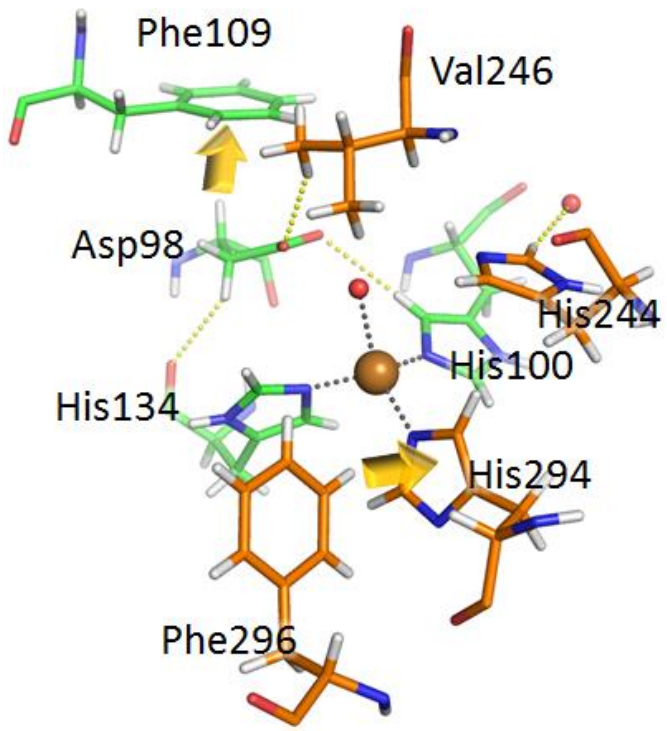

Figure 1-2. The hydrogen bond network around the T2Cu site of *Gk*NIR. CH-O hydrogen bonds are shown as yellow dotted lines. CH-π hydrogen bonds are illustrated by yellow arrows.

The catalytic T2Cu is located in the interdomain cleft ~12 Å from the protein surface and liganded through the $N^{\varepsilon 2}$ atoms of three histidine residues, two provided by the N-terminal domain of one monomer (His100 and His134) and the third provided by the C-terminal domain of the adjacent monomer (His294), forming a trigonal geometry (Fig. 1-2). The T2Cu site is approximately 12.6 Å apart from the T1Cu, and two Cu sites are connected through a peptide chain incorporating residues His134 and Cys135, the T1Cu ligand. Interestingly, CH-π type interaction was found in the T2 site as observed at the T1 Cu. The phenyl group of Phe296, which is situated about 3.6 Å above the imidazole ring of His294, is nearly perpendicular to the plane formed by the

imidazole ring of His294 (Fig. 1-2). Since corresponding residues in other CuNIRs are Ile or Leu, which can form the CH-π hydrogen bond with the His imidazole, this CH-π hydrogen bond is necessary for maintaining the geometry of the T2 Cu. Two catalytic residues, His244 and Asp98, are conserved. H atoms which are on the Nε atom of His244 and Oδ atom of Asp98 are thought to be involved in feeding protons during nitrite reduction. The $C^{\alpha}H$ of Asp98 displays the CH-π hydrogen bond with Phe109 (Fig. 1-2), which has not been observed in other CuNIRs. This CH-π hydrogen bond provides the catalytic centre with rigidity and enables *Gk*NIR to function even at high temperature. According to the proposed mechanism, the side chain of His244 should be protonated (39). Unfortunately, the H atom on the N^{ε} atom of His244 could not be detected in the *F*o-*F*c map. Furthermore, the protonation state of Asp98 was not revealed in our structure because no H atoms are observed on the O^{δ} atom of Asp98 and water molecules close to Asp98. This is probably because that an H atom on an imidazole group or carboxyl group in a protein molecule is often undetectable even using high resolution analysis. We thus need further analyses, e.g., neutron crystallography, to determine the protonation state around the T2 Cu.

The highly conserved Ile controlling the binding mode of and selecting substrate in the active site is replaced by Val in *Gk*NIR. The crystal structure of *Af*NIR in which Ile was mutated to Val was determined by Boulanger & Murphy (PDB code 1L9T) (10) and the T2Cu site in *Gk*NIR is similar to that in the mutated *Af*NIR. CuNIRs which contain naturally substituted Val residues are found in both gram-positive and gram-negative bacterium as well as found in both thermophilic and mesophilic bacterium. This substitution may be rather the mutation fixed by chance than the result of adaptation to environment. Kinetic and X-ray crystallographic analyses using *Af*NIR and its

Ile-to-Val mutant revealed that not only activity of nitrite reduction did not drop but also the coordination mode of the substrate molecule rarely changed even if Ile above the T2Cu was substituted with Val, advocating our speculation.

1.3.2. The unique N-terminal structure is involved in protein-protein electron transfer

The overall structure for *Gk*NIR can be roughly divided with the N- and C-terminal domains, each of which folds into a Greek key ß-barrel domain (Fig. 1-3). As would be predicted by comparing the sequences (8), the Tower loops of *Gk*NIR was shorter than those found in class I CuNIRs. Interestingly, they were also shorter than those of *Ng*NIR, a typical class II CuNIR.

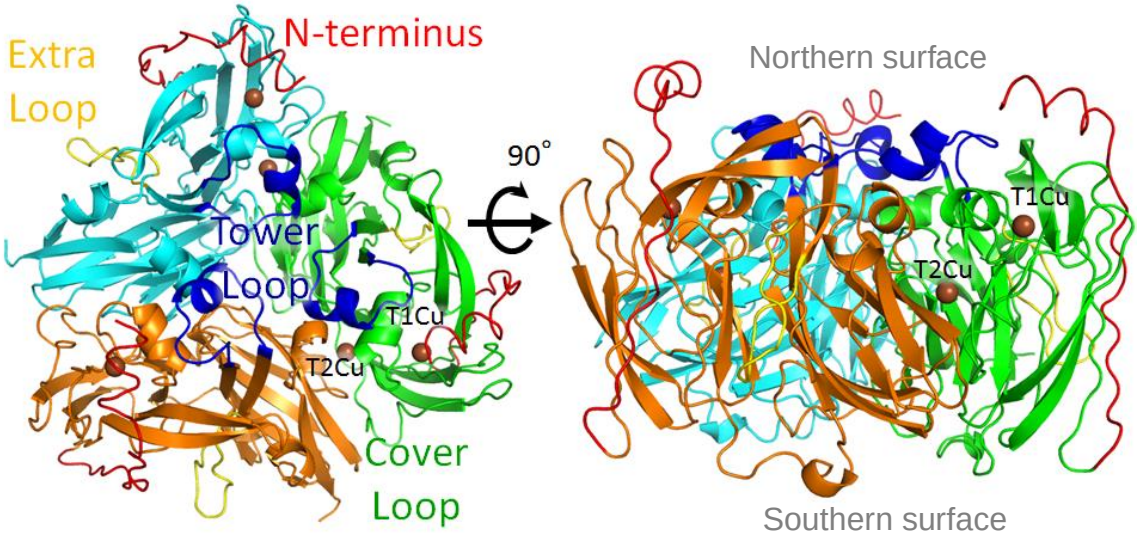

Figure 1-3. The overall trimeric structure of *Gt*NIR. The monomers are illustrated in green, orange, and cyan, respectively. The characteristic N-terminal arm structure, tower loop, and extra loop are shown in red, blue, and yellow, respectively.

Generally, the Tower loop of class I CuNIR adopts a random-coiled structure leading to a four-turned α-helix, which extended toward the T1Cu. Moreover, the seven-residues

deletion in the corresponding Tower loop in the class-II CuNIR results in a shortened α-helix with one and a half turns (7). The 10-residues deletion in the Tower loop region of *Gk*NIR results in a shorter structure. In particular, the random-coiled region of the Tower loop of *Gk*NIR is shorter 10 than those of all the other CuNIRs. Moreover, the unique Extra loop structure suggested by a previous sequence alignment analysis (8), composed of 11 residues of the downstream of the Tower loop, was also confirmed in the *Gk*NIR model. Here, the Extra loop is more than 20 Å apart from both T1Cu and T2Cu and, that it is positioned in the space occupied by the N-terminal polypeptides of all CuNIRs. As mentioned below, the position and the structure of the N-terminus of *Gk*NIR is distinct from other CuNIRs and it does not occupy the same space. Besides the existence of the extra 11 residues in the downstream region of the deleted Tower loop, the overall ß-barrel structure of *Gk*NIR well-overlaps with the tertiary structures of other CuNIRs, including class I CuNIRs. The most unique feature of the structure of *Gk*NIR is its novel N-terminal arm structure composed of 37 residues. While both the N- and C-termini of the typical trimeric CuNIRs are directed towards the southern side of the molecule, the N-terminus of *Gk*NIR extends in the direction of the northern side of the surface of T1Cu and forms an α-helix structure (Fig. 1-3). The place where this α-helix is positioned in CuNIRs corresponds to the interaction surface with the physiological redox-partner proteins (13, 40) and the superposition of *Gk*NIR on the well-known complex structure of *Ax*NIR with its partner *Ax*Cyt c_{551} indicates that the N-terminal α-helix of *Gk*NIR significantly overlaps with *Ax*Cyt c_{551} (Fig. 1-4). Furthermore, to evaluate how this unique structure affects the overall structure of *Gk*NIR, the crystal structure of the N-terminal 37-residues deletion mutant was determined at 1.77-Å resolution (Table. I-I). The refined model of the mutant shows a

very good consistency with the WT *Gk*NIR model, clearly indicating that the folding of the core region of *Gk*NIR is independent on the unique N-terminal region.

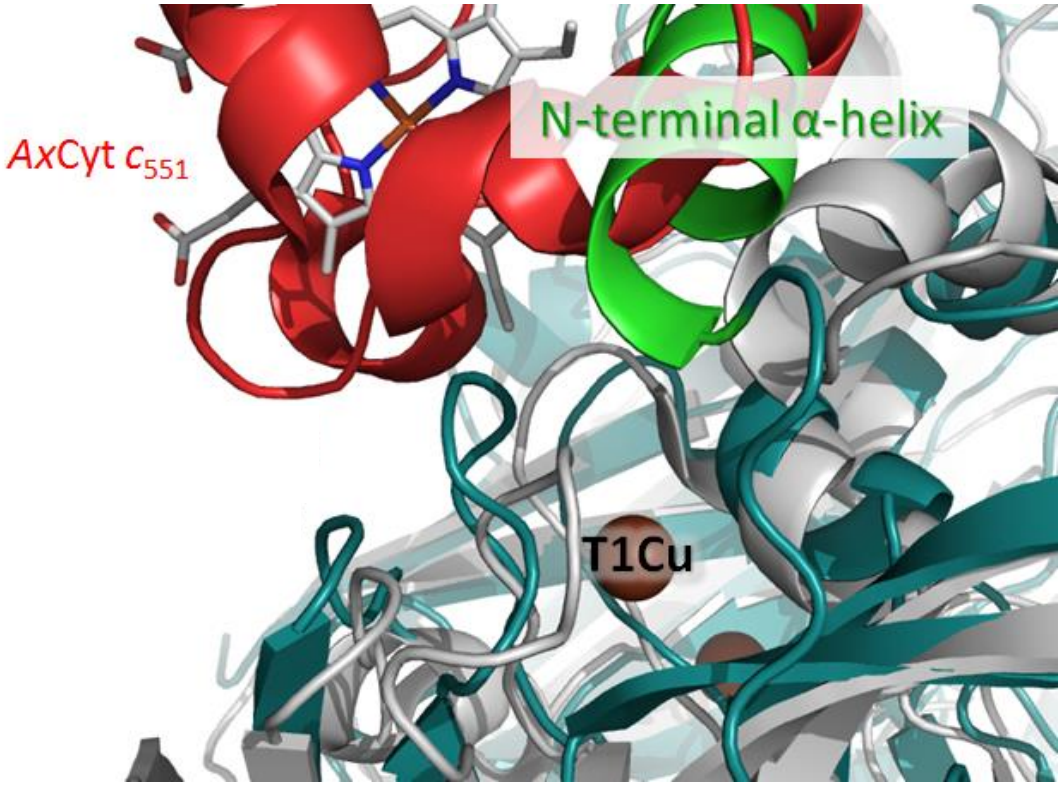

Figure 1-4. Superposition on the electron-transfer complex structure of CuNIR with cytochrome c_{551}. *Gk*NIR, *Ax*NIR, and Cytochrome c_{551} are shown as green, gray, and red.

The nitrite-reducing activity of *Gk*NIR was estimated by a standard assay for CuNIR using methylviologen as the artificial electron donor (39). The resultant k_{cat} was 796 ± 49 s^{-1} at pH 6.5 at 25.0 °C, corresponding to about half of that for *Ax*NIR under the same condition (Table I-II). Furthermore, to elucidate the function of the N-terminal α-helix upon the interprotein ET reaction, the kinetic analysis of ET between CuNIRs and its physiological electron donors was carried out by stopped-flow techniques at 25 °C. Not

only *Ax*NIR, *Ax*Cyt c_{551} and WT *Gk*NIR but also Δ1-20, a N-terminal 13 α-helix deletion mutant of *Gk*NIR, and *Gk*Cyt c_{551}, were used and experiments on all six combinations of CuNIRs and cytochromes were performed. The results for four of the six combinations are shown in Table I-II.

Table I-II. Parameters of interprotein ET kinetics and nitrite reductase activity

	GkCyt c_{551}	AxCyt c_{551}	k_{cat} (s^{-1})	K_m (μM)	k_{cat}/K_m ($s^{-1}\mu M^{-1}$)
GkNiR	3.68[a]	1.60×10^{-1}[a]	7.96×10^{2}	79	10.1
AxNiR	2.05×10[a]	1.09×10^{3}[a]	1.51×10^{3}	42	36.0
Δ1-20	1.28[a]	1.03[a]	—	—	—

[a]Pseudo-first-order ET rate constants between CuNIRs and its redox partners (s^{-1}) measured using stopped-flow spectrophotometer

The pseudo first-order ET rate constant (k_{obs}) of *Ax*Cyt c_{551}-*Gk*NIR is about three orders of magnitude lower than that of *Ax*Cyt c_{551}-*Ax*NIR, while k_{obs} of *Ax*Cyt c_{551}-Δ1-20 is about an order of magnitude larger than that of *Ax*Cyt c_{551}-*Gk*NIR. On the other hand, the comparison of k_{obs} of *Gk*Cyt c_{551}-*Gk*NIR with that of *Gk*Cyt c_{551}-Δ1-20 revealed a 2.8-fold faster ET. These kinetics results clearly indicate that the Δ1-20 mutant loosely recognizes the partner. Because it is assumed that the rate-determining step is the protein-protein association process, the observed differences between the k_{obs} measured in the present experiment reflect the differences of the association processes in which the electron-transfer complexes are formed transiently. The classical Marcus theory describes the rate of the ET accompanying the increase of the distance between two redox centers as an exponential decay (41). In other words, the dramatic decrease in the rate of the ET implies a slight increase of the distance between the two proteins.

Accordingly, it seems that the N-terminal α-helix of *Gk*NIR prevents *Ax*Cyt c_{551} from approaching the neighborhood of the *Gk*NIR T1Cu to form the electron-transfer complex, as predicted by structural analysis. On the other hand, the comparison of the k_{obs} of *Gk*Cyt c_{551}-*Gk*NIR with that of *Gk*Cyt c_{551}-Δ1-20 shows that the former combination achieved 2.8-fold faster ET, meaning that the intermolecular electron transfer between the native proteins pair is faster than that between *Gk*Cyt c_{551} and Δ1-20 mutant. This suggests not only that the N-terminal α-helix structure does not prevent the protein-protein interaction between *Ax*Cyt c_{551} and *Gk*NIR but also that it is necessary to achieve an effective electron transfer in physiological redox-partners pairs. Furthermore, both proteins, *Gk*NIR and *Gk*Cyt c_{551}, are likely to express as membrane-anchored protein in the living *G. kaustophilus* cell, because they have a lipobox motif in the sequences. The present structure and kinetics data clearly indicate that they can form transiently an ET complex using the similar interaction sites to the already-known CuNiR:Cyt c_{551} complex structure.

References

1. Suzuki, S., Kataoka, K. & Yamaguchi, K. (2000). Metal Coordination and Mechanism of Multicopper Nitrite Reductase. *Acc. Chem. Res.* **33**, 728-735.
2. Nakamura, K. & Go, N. (2005). Function and molecular evolution of multicopper blue proteins. *Cellular and Molecular Life Sciences* **62**, 2050-2066.
3. Ellis, M. J., Grossmann, J. G., Eady, R. R. & Hasnain, S. S. (2007). Genomic analysis reveals widespread occurrence of new classes of copper nitrite reductases. *J Biol Inorg Chem* **12**, 1119-27.
4. Feng, L., Wang, W., Cheng, J., Ren, Y., Zhao, G., Gao, C., Tang, Y., Liu, X., Han, W., Peng, X., Liu, R. & Wang, L. (2007). Genome and proteome of long-chain alkane degrading Geobacillus thermodenitrificans NG80-2 isolated from a deep-subsurface

oil reservoir. *Proc Natl Acad Sci U S A* **104**, 5602-7.

5. Manachini, P. L., Mora, D., Nicastro, G., Parini, C., Stackebrandt, E., and, R. P. & Fortina, M. G. (2000). Bacillus thermodenitrificans sp. nov., nom. rev. *International Journal of Systematic and Evolutionary Microbiology* **50**, 1331-1337.
6. Suzuki, S., Kataoka, K., Yamaguchi, K., Inoue, T. & Kai, Y. (1999). Structure–function relationships of copper-containing nitrite reductases. *Coordination Chemistry Reviews* **190-192**, 245-265.
7. Boulanger, M. J. & Murphy, M. E. P. (2002). Crystal Structure of the Soluble Domain of the Major Anaerobically Induced Outer Membrane Protein (AniA) from Pathogenic Neisseria: A New Class of Coppercontaining Nitrite Reductases. *Journal of Molecular Biology* **315**, 1111-1127.
8. Fukuda, Y., Tamada, T., Takami, H., Suzuki, S., Inoue, T. & Nojiri, M. (2011). Cloning, expression, purification, crystallization and preliminary X-ray crystallographic study of GK0767, the copper-containing nitrite reductase from Geobacillus kaustophilus. *Acta Crystallogr Sect F Struct Biol Cryst Commun* **67**, 692-5.
9. Zhao, Y., Lukoyanov, D. A., Toropov, Y. V., Wu, K., Shapleigh, J. P. & Scholes, C. P. (2002). Catalytic Function and Local Proton Structure at the Type 2 Copper of Nitrite Reductase: The Correlation of Enzymatic pH Dependence, Conserved Residues, and Proton Hyperfine Structure. *Biochemistry* **41**, 7464-7474.
10. Boulanger, M. J. & Murphy, M. E. (2003). Directing the mode of nitrite binding to a copper-containing nitrite reductase from Alcaligenes faecalis S-6: characterization of an active site isoleucine. *Protein Sci* **12**, 248-56.
11. Usov, O. M., Sun, Y., Grigoryants, V. M., Shapleigh, J. P. & Scholes, C. P. (2006). EPR-ENDOR of the Cu(I)NO Complex of Nitrite Reductase. *J. Am. Chem. Soc.* **128**.
12. Babu, M. M., Priya, M. L., Selvan, A. T., Madera, M., Gough, J., Aravind, L. & Sankaran, K. (2006). A database of bacterial lipoproteins (DOLOP) with functional assignments to predicted lipoproteins. *J Bacteriol* **188**, 2761-73.
13. Nojiri, M., Koteishi, H., Nakagami, T., Kobayashi, K., Inoue, T., Yamaguchi, K. & Suzuki, S. (2009). Structural basis of inter-protein electron transfer for nitrite reduction in denitrification. *Nature* **462**, 117-20.
14. Engin Arslan, Schulz, H., Zufferey, R., Künzler, P. & Thöny-Meyer, L. (1998). Overproduction of the *Bradyrhizobium japonicum c*-Type Cytochrome Subunits of the *cbb*$_3$ Oxidase in *Escherichia coli. Biochem Biophys Res Commun.* **251**, 744-747.
15. Otwinowski, Z. & Minor, W. (1997). [20] Processing of X-ray diffraction data collected in oscillation mode. *Methods Enzymol.* **276**, 307-326.

16. Vagin, A. & Teplyakov, A. (2010). Molecular replacement with MOLREP. *Acta Crystallogr D Biol Crystallogr* **66**, 22-5.

17. Winn, M. D., Ballard, C. C., Cowtan, K. D., Dodson, E. J., Emsley, P., Evans, P. R., Keegan, R. M., Krissinel, E. B., Leslie, A. G., McCoy, A., McNicholas, S. J., Murshudov, G. N., Pannu, N. S., Potterton, E. A., Powell, H. R., Read, R. J., Vagin, A. & Wilson, K. S. (2011). Overview of the CCP4 suite and current developments. *Acta Crystallogr D Biol Crystallogr* **67**, 235-42.

18. Emsley, P., Lohkamp, B., Scott, W. G. & Cowtan, K. (2010). Features and development of Coot. *Acta Crystallogr D Biol Crystallogr* **66**, 486-501.

19. Sheldrick, G. M. (2008). A short history of SHELX. *Acta Crystallogr A* **64**, 112-22.

20. Adams, P. D., Afonine, P. V., Bunkoczi, G., Chen, V. B., Davis, I. W., Echols, N., Headd, J. J., Hung, L. W., Kapral, G. J., Grosse-Kunstleve, R. W., McCoy, A. J., Moriarty, N. W., Oeffner, R., Read, R. J., Richardson, D. C., Richardson, J. S., Terwilliger, T. C. & Zwart, P. H. (2010). PHENIX: a comprehensive Python-based system for macromolecular structure solution. *Acta Crystallogr D Biol Crystallogr* **66**, 213-21.

21. Laskowski. R. A., MacArthur. M. W., Moss. D. S. and Thornton. J. M. (1993). PROCHECK - a program to check the stereochemical quality of protein structures. *J. App. Cryst.* **26**, 283-291.

22. Chen, V. B., Arendall, W. B., 3rd, Headd, J. J., Keedy, D. A., Immormino, R. M., Kapral, G. J., Murray, L. W., Richardson, J. S. & Richardson, D. C. (2010). MolProbity: all-atom structure validation for macromolecular crystallography. *Acta Crystallogr D Biol Crystallogr* **66**, 12-21.

23. Brünger, A. T., Adams, P. D., Clore, G. M., DeLano, W. L., Gros, P., Grosse-Kunstleve, R., Jiang, J.-S., Kuszewski, J., Nilges, M., Pannu, N. S., Read, R. J., Rice, L. M., Simonson, T. & Warren, G. L. (1998). Crystallography & NMR System: A New Software Suite for Macromolecular Structure Determination. *Acta Crystallogr D Biol Crystallogr* **54**, 905-921.

24. Nojiri, M., Xie, Y., Inoue, T., Yamamoto, T., Matsumura, H., Kataoka, K., Deligeer, Yamaguchi, K., Kai, Y. & Suzuki, S. (2007). Structure and function of a hexameric copper-containing nitrite reductase. *Proc Natl Acad Sci U S A* **104**, 4315-20.

25. Godden, J., Turley, S., Teller, D., Adman, E., Liu, M., Payne, W. & LeGall, J. (1991). The 2.3 angstrom X-ray structure of nitrite reductase from Achromobacter cycloclastes. *Science* **253**, 438-442.

26. Kukimoto, M., Nishiyama, M., Murphy, M. E. P., Turley, S., Adman, E. T., Horinouchi, S. & Beppu, T. (1994). X-ray Structure and Site-Directed Mutagenesis of a Nitrite

Reductase from Alcaligenes Faecalis S-6: Roles of Two Copper Atoms in Nitrite Reduction. *Biochemistry* **33**, 5246-5252.

27. Jacobson, F., Guo, H., Olesen, K., Okvist, M., Neutze, R. & Sjolin, L. (2005). Structures of the oxidized and reduced forms of nitrite reductase from Rhodobacter sphaeroides 2.4.3 at high pH: changes in the interactions of the type 2 copper. *Acta Crystallogr D Biol Crystallogr* **61**, 1190-8.
28. Kanbi, L. D., Antonyuk, S., Hough, M. A., Hall, J. F., Dodd, F. E. & Hasnain, S. S. (2002). Crystal Structures of the Met148Leu and Ser86Asp Mutants of Rusticyanin from Thiobacillus ferrooxidans: Insights into the Structural Relationship with the Cupredoxins and the Multi Copper Proteins. *Journal of Molecular Biology* **320**, 263-275.
29. Marshall, N. M., Garner, D. K., Wilson, T. D., Gao, Y. G., Robinson, H., Nilges, M. J. & Lu, Y. (2009). Rationally tuning the reduction potential of a single cupredoxin beyond the natural range. *Nature* **462**, 113-6.
30. Hadt, R. G., Sun, N., Marshall, N. M., Hodgson, K. O., Hedman, B., Lu, Y. & Solomon, E. I. (2012). Spectroscopic and DFT studies of second-sphere variants of the type 1 copper site in azurin: covalent and nonlocal electrostatic contributions to reduction potentials. *J Am Chem Soc* **134**, 16701-16.
31. Dey, A., Jenney, F. E., Jr., Adams, M. W., Babini, E., Takahashi, Y., Fukuyama, K., Hodgson, K. O., Hedman, B. & Solomon, E. I. (2007). Solvent tuning of electrochemical potentials in the active sites of HiPIP versus ferredoxin. *Science* **318**, 1464-8.
32. Guss, J. M., Merritt, E. A., Phizackerley, R. P. & Freeman, H. C. (1996). The Structure of a Phytocyanin, the Basic Blue Protein from Cucumber, Refined at 1.8 Å Resolution. *Journal of Molecular Biology* **262**, 686-705.
33. Inoue, T., Gotowda, M., Deligeer, Kataoka, K., Yamaguchi, K., Suzuki, S., Watanabe, H., Gohow, M. & Kai, Y. (1998). Type 1 Cu Structure of Blue Nitrite Reductase from Alcaligenes xylosoxidans GIFU 1051 at 2.05 A Resolution: Comparison of Blue and Green Nitrite Reductases. *J. Biochem* **124**, 876-879.
34. Sukumar, N., Mathews, F. S., Langan, P. & Davidson, V. L. (2010). A joint x-ray and neutron study on amicyanin reveals the role of protein dynamics in electron transfer. *Proc Natl Acad Sci U S A* **107**, 6817-22.
35. LaCroix, L. B., Shadl, S. E., Wang, Y., Averill, B. A., Hedman, B., Hodgson, K. O. & Solomon, E. I. (1996). Electronic Structure of the Perturbed Blue Copper Site in Nitrite Reductase: Spectroscopic Properties, Bonding, and Implications for the Entatic/Rack State. *J Am Chem Soc* **118**, 7755-7768.

36. Pierloot, K., Kerpel, J. O. A. D., Ryde, U., Olsson, M. H. M. & Roos, B. O. (1998). Relation between the Structure and Spectroscopic Properties of Blue Copper Proteins. *J Am Chem Soc* **120**, 13156-13166.

37. Kohzuma, T. (1999). The Structure and Unusual pH Dependence of Plastocyanin from the Fern Dryopteris crassirhizoma. The protonation of an active site histidine is hindered by pi - pi interactions. *Journal of Biological Chemistry* **274**, 11817-11823.

38. Fitzpatrick, M. B., Obara, Y., Fujita, K., Brown, D. E., Dooley, D. M., Kohzuma, T. & Czernuszewicz, R. S. (2010). Non-covalent interactions in blue copper protein probed by Met16 mutation and electronic and resonance Raman spectroscopy of Achromobacter cycloclastes pseudoazurin. *J Inorg Biochem* **104**, 250-60.

39. Kataoka, K., Furusawa, H., Takagi, K., Yamaguchi, K. & Suzuki, S. (2000). Functional Analysis of Conserved Aspartate and Histidine Residues Located Around the Type 2 Copper Site of Copper-Containing Nitrite Reductase. *J. Biochem* **127**, 345-350.

40. Vlasie, M. D., Fernandez-Busnadiego, R., Prudencio, M. & Ubbink, M. (2008). Conformation of pseudoazurin in the 152 kDa electron transfer complex with nitrite reductase determined by paramagnetic NMR. *J Mol Biol* **375**, 1405-15.

41. Marcus, R.A., Sutin, N. (1985). Electron transfers in chemistry and biology, *Biochim. Biophys. Acta,* **811**, 265-322.

Chapter 2

Structural insights into the nitrite reduction of *Gt*NIR

Summary

Copper-containing nitrite reductase (CuNIR) catalyzes the reduction of nitrite (NO_2^-) to nitric oxide (NO) during denitrification. We determined the crystal structures of CuNIR from thermophilic gram-positive bacterium, *Geobacillus thermodenitrificans* (*Gt*NIR) in chloride- and formate-bound forms of wild type at 1.15 Å resolution and the nitrite-bound form of the C135A mutant at 1.90 Å resolution. The structure of C135A with nitrite displays a unique η^1-O coordination mode of nitrite at the catalytic copper site (T2Cu), which has never been observed at the T2Cu site in known wild-type CuNIRs, because the mobility of two residues essential to catalytic activity, Asp98 and His244, are sterically restricted in *Gt*NIR by Phe109 on a characteristic loop structure that is found above Asp98 and by an unusually short CH-O hydrogen bond observed between His244 and water, respectively. A detailed comparison of the WT structure with the nitrite-bound C135A structure implies the replacement of hydrogen-bond networks around His244 and predicts the flow path of protons consumed by nitrite reduction. Based on these observations, the reaction mechanism of *Gt*NIR through the η^1-O coordination manner is proposed.

2.1. Introduction

Denitrification is a part of the geobiochemical nitrogen cycle and is the process by which some organisms couple the respiratory system to the gradual reduction of nitrate or

nitrite (NO_3^- or NO_2^-) to gaseous dinitrogen (N_2) via the respective formation of nitric oxide (NO) and nitrous oxide (N_2O) (1). Due mainly to the invention of the Haber-Bosch process, the amount of nitrogen oxides contained in soils and waters have been increasing enough that the balance of the nitrogen cycle is at stake (2, 3). Denitrification is, therefore, attracting attention because of its potential agronomic and environmental impacts (2, 4). Each step of denitrification is catalyzed by a distinct metal-containing reductase, the structures of which have been elucidated at an atomic level. Despite the global contribution of the denitrification process in extremophiles as well as mesophilic organisms, little attention has been paid to enzymes originating from extremophilic denitrifiers (5). In fact, the crystal structures of only two enzymes have been elucidated to date: a nitric oxide reductase from the thermophilic bacterium, *Geobacillus stearothermophilus* (6), and a copper-containing nitrite reductase (CuNIR) from the psychrophilic bacterium, *Pseudoalteromonas haloplanktis* (7).

CuNIR is a periplasmic enzyme responsible for the one-electron reduction of NO_2^- to NO ($NO_2^- + 2H^+ + e^- \rightarrow NO + H_2O$), a key reaction in denitrification as the nitrogen compound is changed from an ionic state to a gaseous molecule. CuNIR typically has a homotrimeric structure containing one type 1 (T1Cu) and one type 2 Cu (T2Cu) site per monomer. The T1Cu atom is coordinated by four amino acid residues (two histidine residues, cysteine and methionine) and functions as a receptor site for the electron supplied by an electron-donor protein such as *c*-type heme-containing cytochrome (8, 9) or blue-copper proteins (10, 11). The T2Cu site is a catalytic center composed of three histidine residues and an axial ligand water molecule. The two Cu sites are spaced ~12.5 Å away from each other but are connected through adjacent residues, that is, cysteine and histidine, which are the ligands of the T1Cu and T2Cu centers, respectively.

Such a structure enables efficient intramolecular electron transfer (ET) from the T1Cu center to the T2Cu center. A great number of spectroscopic, kinetic, and crystallographic studies have shown that the conserved aspartate and histidine (hereafter named as Asp^{cat} and His^{cat}) located above the T2Cu center are undoubtedly essential for enzymatic activity (12-18). The reaction mechanism of CuNIR has been proposed by several groups based on the crystal structures of the NO_2^-- and NO-bound forms (14, 17, 18). Although there are small differences between the suggested mechanisms, a common view is that NO_2^- binds to the T2Cu atom in an η^2-O,O side-on manner and forms a hydrogen bond with Asp^{cat} to form an intermediate, HONO, which is quickly reduced and drives the release of NO. One of the most important insights into the mechanism, which has been recently provided by Hasnain, Scrutton, and colleagues, is that the ET reaction is coupled with the proton transfer reaction (19, 20). However, the detailed reaction mechanism is still a topic of discussion.

Recent genomic analyses have revealed that a wide variety of organisms from all three taxonomic domains contains at least one gene encoding CuNIR (*nirK*) (21, 22). Among them, we have been focusing on thermostable CuNIRs because denitrification in thermophiles has a great deal of potential in industry; that is, the denitrification process at high temperatures can be applied to speeding up the removal of nitrogen oxides in polluted water bodies. *Geobacillus* is a genus of an extremophilic gram-positive bacterium (23) and several species within this group are known to be denitrifiers (24-26). The amino acid sequences of *Geobacillus* CuNIRs show high similarity to each other (80-95 %) but in contrast, the sequences show low similarities (20-40 %) to CuNIRs from other species (27); therefore, *Geobacillus* CuNIR likely possesses a structure different from other CuNIRs. Although the crystal structure of a

thermotolerant CuNIR from the thermophilic *Geobacillus kaustophilus* HTA426 (*Gk*NIR) has recently been determined (submitted), the detailed structure of the catalytic T2Cu site and the associated reaction mechanism has yet to be explored. *Geobacillus* CuNIR can perform nitrite reduction even at room temperature (28); however, it remains unknown whether thermostable CuNIR will follow the same mechanism as that of other CuNIRs from mesophilic organisms.

In this chapter, the high-resolution crystal structures of a soluble domain of another thermophilic *Geobacillus* CuNIR from *Geobacillus thermodenitrificans* NG80-2 (*Gt*NIR) are reported. In contrast with *G. kaustophilus*, which is devoid of the terminal enzyme, nitrous oxide reductase (29), *G. thermodenitrificans* possesses a complete set of all genes needed for absolute denitrification (30). As reported herein, the structure of wild type *Gt*NIR (WT) was determined at near atomic resolution (1.15 Å resolution). We then tried to determine the complex structure of *Gt*NIR with substrate. However, it is known that in nitrite-soaked CuNIR crystals, NO_2^- bound to the T2Cu center was reduced to NO (18). The combined microspectroscopic and crystallographic analyses revealed that hydrated electrons produced upon X-ray irradiation rapidly reduce the T1Cu sites (31). When nitrite is bound to the T2Cu site, an electron gained by the T1Cu site can be effectively transferred to the T2Cu site and consumed during the reduction of NO_2^- to NO. Therefore, interpretation of electron density above the T2Cu sites in the nitrite-soaked crystal structure is usually difficult because it can be assigned as a mixture of NO_2^-, NO, and water. To avoid a faulty judgment, we employed two methods. First, we determined the complex structure of WT with formate, which is an analog of nitrite and is unlikely to be reduced during data collection. Second, we made a mutant in which Cys135, one of the T1Cu ligands, is replaced with alanine based on a previous

report that such a mutant lacks the T1Cu atom and hence the ability to capture an electron (32). The complex structure of the C135A mutant with nitrite has been successfully determined and shows a unique monodentate Cu(II)-nitrito complex at the T2Cu site. Our structures provide new insights into the detailed structure of the T2Cu site as well as the reaction mechanism in a thermostable CuNIR.

2.2. Methods

2.2.1. Expression and purification of WT *Gt*NIR and the C135A mutant

The coding sequence of the putative soluble domain of *Geobacillus thermodenitrificans* NG80-2 CuNIR (NCBI Reference Sequence: NC_009328.1) from nucleotides 251 to 1377 was synthesized, by Fasmac Co.,Ltd, with *Nco*I and *Hind*III sequences to be cloned into the pET-22b vector. The resulting pET-22b-*Gt*NIR construct was used to transform BL21 (DE3) *E. coli*. The cells were grown from a single colony in six 1500 mL Luria-Bertani cultures containing ampicillin at 200 μg ml^{-1} to an A_{600} of 0.35 at 39 °C with shaking at 180 rpm. The temperature was then reduced to 20 °C, and the cells were allowed to grow further to an A_{600} of 0.6–0.7 when expression was induced by the addition of IPTG to a final concentration of 1 mM. The cultures were left for 18 h before the cells were harvested by centrifugation. Cells were immediately resuspended in 40 mL of ice cold resuspension buffer (40 mM HEPES pH 8.0 for samples of WT-formate and C135A-NO_2, 40 mM Tris-HCl pH 8.0 for the sample of WT, buffer A). The cells were disrupted by sonication in a chilled water bath and the cell lysate was incubated at 343 K for 120 min or 353 K for 30 min. The sample was centrifuged at 15000 g for 60 min and 10 mL of 10 mM $CuSO_4$ was added to the supernatant. The resulting greenish blue

solution was loaded onto a HiLoad 16/600 Superdex 200 column (GE Healthcare UK Ltd., Buckinghamshire, UK) pre-equilibrated with buffer A. The fractions containing *Gt*NIR were collected and ammonium sulfate was added to the sample solution up to 40% w/v. After incubation at 277 K for 30 min, the solution was centrifuged at 15 000g for 30 min and the supernatant was applied onto a HiTrap Phenyl HP column (GE Healthcare UK Ltd.) pre-equilibrated with buffer A containing 40% w/v ammonium sulfate. The protein was eluted with a linear gradient of ammonium sulfate concentration from 40 % to 0 % w/v. The fractions containing *Gt*NIR were collected and dialyzed with buffer A at 277 K for 12 h. The sample was loaded onto a HiTrap Q HP column (GE Healthcare UK Ltd.) pre-equilibrated with buffer A and after washing with buffer A, the protein was eluted with a linear gradient of ammonium sulfate concentration from 0 to 0.5 M (the sample for WT was eluted with a linear gradient of NaCl concentration from 0 to 0.5 M). The fractions containing *Gt*NIR were combined together and loaded onto a HiLoad 16/60 Superdex 200 column (GE Healthcare UK Ltd.) pre-equilibrated with buffer A. *Gt*NIR were collected and estimated to be >95% pure using SDS-PAGE; the absorption ratio of A_{280} to A_{600} was ~11. Protein concentrations for all subsequent experiments were determined by measuring the A_{280} using an extinction coefficient of 27390 M^{-1} cm^{-1} and a molecular weight of 35478 Da.

The forward and reverse primers for the C135A mutant were 5'-TTATGTACCATGCAGGTACGAAGCCA-3' and 5'-TGGCTTCGTACCTGCATGGTACATAA-3', respectively. The mutant plasmids were confirmed by DNA sequencing before transformation into *E. coli* strain BL21 (DE3) *E. coli*. The mutant was expressed and purified following the wild-type protein protocol.

2.2.2. Crystallization of *Gt*NIR

X-ray diffraction-quality greenish blue crystals of the wild type (WT) were grown in hanging drops consisting of 1.5 µl protein solution (100 mg ml^{-1}) and 1.5 µl well solution and the drops were equilibrated in 0.45 ml well solution [0.1M acetate buffer pH 4.5, 5.0 % (w/v) PEG 4000, and 75 mM $CuSO_4$] at 293 K. The very important difference from the previously reported crystallization conditions for *Gk*NIR was the use of $CuSO_4$ instead of $ZnSO_4$. This minor difference resulted in a drastic improvement of quality of crystals. Crystals of WT with formate (WT-formate) were grown in hanging drops consisting of 1.5 µl protein solution (100 mg ml^{-1}) and 1.5 µl well solution and the drops were equilibrated in 0.45 ml well solution [0.1M acetate buffer pH 4.5, 5.0 % (w/v) PEG 4000, 75 mM $CuSO_4$, 200 mM sodium formate] at 293 K. Nitrite-soaked C135A crystals (C135A-NO_2) were obtained by soaking the colorless crystals of C135A, which was grown in the same condition as WT, in 200 mM sodium nitrite for 20 minutes.

2.2.3. X-ray diffraction data collection, phasing, and refinement

Prior to synchrotron data collection, all crystals were rinsed with well solution containing 35 % (v/v) 2-methyl-2,4-pentanediol as a cryoprotectant and then flash-cooled by immersion in liquid nitrogen. Data sets were collected from a single crystal at 100 K on beamline BL44XU (for WT) and BL38B1 (for C135A-NO_2) at SPring-8 (Hyogo, Japan) using a MX-225HE and an ADSC Quantum 315 CCD detector (Area Detector Systems Co., California, USA), respectively, and on beamline BL1A (for WT-formate) at Photon Factory (Tsukuba, Ibaraki, Japan) using a Pilatus 2M-F detector (DECTRIS Ltd., Baden, Switzerland). The HKL-2000 package (33) was used to

reduce, integrate and scale the collected data. The crystals belonged to space group *R*3, with a *Gt*NIR monomeric molecule per asymmetric unit. The crystal structure was determined by molecular replacement using the program MOLREP (34) from the CCP4 suite (35). A monomeric subunit of *Gk*NIR (sequence identity between *Gk*NIR and *Gt*NIR is 94 %) described in the previous chapter was used as the search model. The resulting *Gt*NIR models were subject to a cycle of positional and individual *B*-factor refinement in REFMAC5 (36). Manual model building was carried out using COOT (37) thorough the refinement process. Water molecules were added to the model using the automated water-searching program built into COOT, and during the refinement of the WT and WT-formate structures, anisotropic refinement parameters were introduced. When the structure of WT was refined, electron density on the T2Cu atom was first assigned to fully occupied water. The *B*-factor of the resulting water molecule was, however, unusually small and positive electron density remained at the position in the resulting F_o-F_c map. Therefore, partially occupied chloride was assigned instead because Tris-HCl buffer was used in the purification of the sample for WT. To be more exact, this axial ligand may be a mixture of chloride and water; that is, there are actually several states of axial ligands of the T2Cu atom in WT. However, we regarded it as one chloride ion in the refinement for simplicity. When the structure of the WT-formate structure was being refined, electron density on the T2Cu center was first assigned to formate with two predominant binding modes (η^1-O and η^2-O,O).However, formate in the η^2-O,O binding mode showed a distance between the carbon atom of formate and the T2 Cu atom (2.13 Å), which is shorter than that between the oxygen atoms of nitrite and the T2Cu atom [2.27 (O1-Cu) and 2.22 (O2-Cu) Å]. Therefore, partially occupied formate and water molecules were assigned to this position. The

copper coordination geometry was not restrained. To calculate the correct distances between the C^{γ} atom and O^{δ} atoms of Asp98, the unrestrained refinement was executed for the WT and WT-formate structures. The final models were checked for stereochemical quality using PROCHECK (38) and MolProbity (39). Data-collection and refinement statistics are summarized in Table II-I.

Table II-I. Data collection and refinement statistics for *Gt*NIR WT, C135A-NO_2, and WT-formate

	WT	C135A-NO2	WT-formate
Data collection			
Beamline	SPring-8 BL44XU	SPring-8 BL38B1	PF BL1A
Wavelength (Å)	0.9	0.9	0.9
Space group	*R*3	*R*3	*R*3
Unit cell			
a = *b*, *c* (Å)	115.05, 84.42	114.87, 84.04	114.98, 84.43
Resolution range (Å)	50.0-1.15	50.0-1.90	100.0-1.15
	(1.17-1.15)[a]	(1.94-1.90)	(1.17-1.15)
R_{merge} (%)[b]	7.3 (28.5)	10.5 (24.6)	8.6 (31.7)
Completeness (%)	95.7 (91.7)	93.2 (90.7)	97.3 (98.9)
Unique reflections	141,618 (6786)	30,251 (1461)	143,313 (7283)
$\langle I/\sigma(I)\rangle$	13.2 (1.6)	9.5 (2.0)	19.7 (2.8)
Redundancy	2.6 (2.1)	2.3 (2.0)	3.3 (2.9)
Refinement			
Resolution range (Å)	22.06-1.15	25.18-1.90	26.25-1.15
No. of Reflections	134,511	28,714	136,148
R_{work} (%)[c]/ R_{free} (%)[d]	13.1/16.3	15.6/20.6	11.8/13.7
RMSD bond length (Å)	0.029	0.023	0.023
RMSD bond angle (°)	2.499	2.088	2.322
Ramachandran (%)[e]			
Favored	98.3	96.9	98.3
Allowed	1.7	3.1	1.7
Outliers	0	0	0
ESU based on ML (Å)[f]	0.023	0.078	0.012

[a] Values in parentheses are for the highest-resolution shell.. [b] R_{merge} is calculated as $\Sigma_{hkl}\Sigma_i | I_i(hkl)-\langle I(hkl)\rangle | / \Sigma_{hkl}\Sigma_i I(hkl)$, where $I_i(hkl)$ is the intensity of an individual measurement of the reflection with Miller indices *hkl* and $\langle I(hkl)\rangle$ is the average intensity from multiple observations. [c] $R_{work} = \Sigma_{hkl} | \, | F_{obs} | - | F_{calc} | \, | / \Sigma_{hkl} | F_{obs} |$, where F_{obs} and F_{calc} are the observed and calculated structure-factor amplitudes, respectively. [d] The free *R* factor, R_{free}, is computed in the same manner as R_{work} but using only a small set (5%) of randomly chosen intensities that were not used in the refinement of the model. [e] MolProbity statistics (39). [f] ESU, estimated standard uncertainty; ML, maximum likelihood.

Table II-II. Copper site ligand and hydrogen-bond distances

parameter	WT	C135A-NO_2	WT-formate
I. Type 1 Cu-Ligand Distances (Å)			
T1Cu-H95N$^{\delta 1}$	2.03	2.14	2.05
T1Cu-C135S$^{\gamma}$	2.17	3.55[a]	2.22
T1Cu-H143N$^{\delta 1}$	2.01	1.96	2.01
T1Cu-M148S$^{\delta}$	2.61	2.07	2.59
II. Type 1 Cu-Ligand Angles (°)			
H95N$^{\delta 1}$-T1Cu-C135S$^{\gamma}$	138.9	n/a	135.2
H95N$^{\delta 1}$-T1Cu-H143N$^{\delta 1}$	100.4	102.9	102.8
His95N$^{\delta 1}$-T1Cu-M148S$^{\delta}$	81.7	101.7	81.7
C135S$^{\gamma}$-T1Cu-H143N$^{\delta 1}$	105.0	n/a	107.2
C135S$^{\gamma}$-T1Cu-M148S$^{\delta}$	113.6	n/a	113.0
H143N$^{\delta 1}$-T1Cu-M148S$^{\delta}$	116.5	155.3	115.7
III. Type 2 Cu-Ligand Distances (Å)			
T2Cu-H100N$^{\varepsilon 2}$	1.93	1.96	1.98
T2Cu-H134N$^{\varepsilon 2}$	1.97	1.95	1.99
T2Cu-H294N$^{\varepsilon 2}$	1.96	2.01	1.98
T2Cu-Wat0/Cl	2.23/2.22	n/a	2.19
T2Cu-$N_{nitrite}$ or $C_{formate}$	n/a	2.85	3.27
T2Cu-$O1_{nitrite}$ or $O1_{formate}$	n/a	3.41	4.11
T2Cu-$O2_{nitrite}$ or $O2_{formate}$	n/a	1.97	2.21
IV. H-Bond Distances around the Active Site (Å)			
D98O$^{\delta 2}$-Wat0	2.48	n/a	2.35
D98 O$^{\delta 2}$-$O2_{nitrite}$ or $O2_{formate}$	n/a	3.38	3.72
D98O$^{\delta 1}$-Wat1	2.90	3.15	2.85
D98O$^{\delta 2}$-Wat1	3.41	3.31	3.44
H244N$^{\varepsilon 2}$-Wat1	2.94	2.75	2.99
H244C$^{\varepsilon 1}$-Wat3[c]	3.12	3.03	3.09
Wat1-Wat2 (Wat2A/2B)	2.76/2.69	2.68	2.76/2.69
Wat3-Wat2 (Wat2A/2B)	3.49/4.39[d]	3.85[d]	3.57/4.61[d]

[a] The distance between the T1Cu and the methyl carbon of Ala135. [b] Left, values from molecule A; right, values from molecule B. [c] Unusual short CH-O hydrogen bond. [d] Longer than accepted hydrogen bond distance.

2.3. Results

2.3.1. The copper centers in *Gt*NIR

The structure of C135A in complex with nitrite (C135A-NO_2) was determined at 1.90 Å resolution. In addition, two other crystal structures of *Gt*NIR, wild type (WT) and a WT structure in complex with formic acid (an analog of nitrite, WT-formate), were both determined at near atomic resolution (1.15 Å). Data-collection and refinement statistics are summarized in Table 1. The overall structure of *Gt*NIR composed of 294 amino acid residues resembles those of other known homotrimeric CuNIRs. As expected from the exclusively high similarity of the amino acid sequences between CuNIRs from *G. thermodenitrificans* and *G. kaustophilus* (94 %), the structure of *Gt*NIR is very similar to that of *Gk*NIR as indicated by root mean square deviation of 0.07 Å calculated for superposed 277 C^{α} atoms and has a unique N-terminal arm structure, a short tower loop, and an extra loop, which were also found in *Gk*NIR. The RMSD (C^{α}) between the WT and WT-formate complex structures is 0.08 Å, which indicates that binding of a small molecule to the T2Cu center did not dramatically affect the overall structure of *Gt*NIR. The geometry of the T1Cu sites in the WT and WT-formate structures are almost the same as that of previously analyzed *Gk*NIR (submitted). Therefore, we will not describe these details in this paper. The geometric parameters of the Cu centers of *Gt*NIR are shown in Table II-II.

The crystal structure of C135A-NO_2 contains a fully occupied Cu atom at the T1Cu site (Figure 2-1A), although in the C130A mutant of CuNIR from *Achromobacter xylosoxidans* (*Ax*NIR), which is equivalent to our C135A mutant, the T1Cu site is completely devoid of a metal ion (32). Three ligands, His95, His143 and Met148,

contribute to the formation of a slightly distorted T-shaped center. Figure 2-1B presents a comparison of the T1Cu site in C135A-NO_2 with that in WT. The distance between Cu–S^{Met148} is 2.07 Å, which is much shorter than that in WT (2.61 Å). Although the methyl carbon of Ala135 is unexpectedly close to the T1Cu atom (3.55 Å), no coordination bond is observed between the T1Cu center and

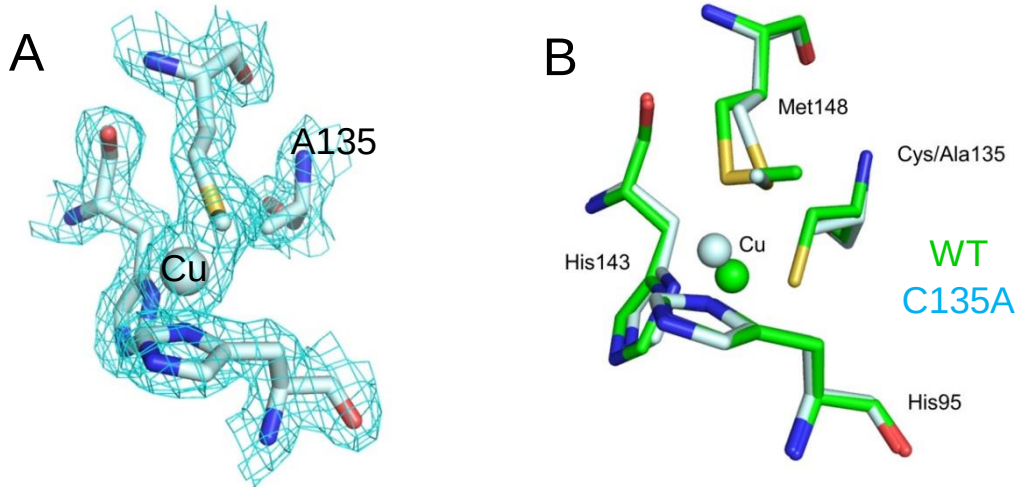

Figure 2-1. (A) The T1Cu site of C135A-NO2. (B) Superposition of C135A-NO_2 on WT

Ala135. As compared with WT, no structural changes except minimal shift (0.4 Å) of the carbonyl oxygen atom of Gly136 was observed in the second coordination sphere of the T1Cu center in C135A despite the drastic conformational change in the first coordination sphere. The RMSD between the WT and C135A-NO_2 structures is only 0.12 Å, which reveals that the protein backbone is barely affected by the point mutation and soaking of nitrite. A well-defined omit electron density map in the region of the T2Cu site revealed density in the apical position of the copper that could best be modeled as a nonlinear molecule of three atoms. This density was modeled as fully occupied nitrite coordinated to the T2Cu center in an η^1-O coordination manner (Figure 2-2). A monodentate coordination mode has never been observed in other wild-type

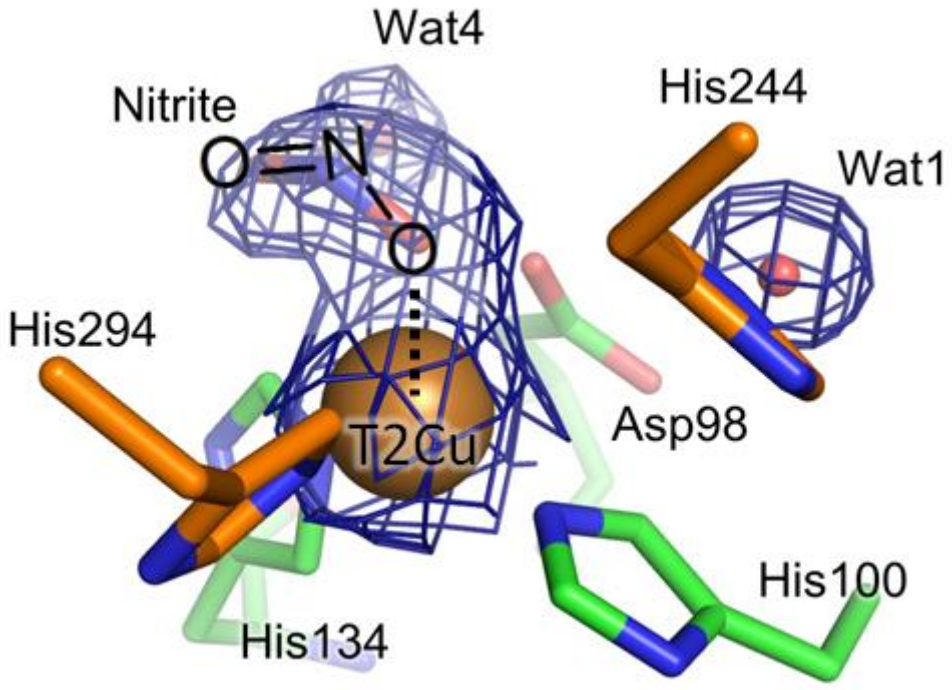

Figure 2-2. The η^1-O binding mode of nitrite at the T2Cu site in C135A-NO_2. The $2F_o$-F_c (contoured at 1.0 σ) is represented by a dark blue mesh. The Cu ion is shown as a brown sphere. Carbon, oxygen, and nitrogen atoms are shown in green, red, and blue, respectively. Carbon atoms of residues originating from an adjacent monomer in the crystallographic asymmetric unit are shown in orange.

T2Cu sites in CuNIR structures in which nitrite adopts an η^2-O,O binding mode.(17, 18) The distance between the O2 atom (closest to the T2Cu atom) of nitrite and the T2Cu atom is 1.97 Å, which is slightly shorter than the distances observed in the η^2-O,O binding mode in structures of CuNIR from *Alcaligenes faecalis* (*Af*NIR) [2.04-2.08 Å (Cu-O2), 2.29-2.38 Å (Cu-O1)] and is consistent with those seen in model complexes showing the η^1-O coordination manner of nitrite (1.94-2.01 Å) (40, 41). A refined average *B*-factor of 31 $Å^2$ indicates that the nitrite ion is well ordered. A slightly larger *B*-factor of the non-coordinated O1 atom (42 $Å^2$), however, indicates that it is more disordered than the other two atoms of nitrite. A hydrogen bond can be formed between the O2 atom of nitrite and the $O^{\delta 2}$ atom of Asp98 (3.38 Å) and between the O1 atom of nitrite

and Wat4 (3.07 Å). Figure 2-3 illustrates a comparison of the nitrite-bound T2Cu site in *Gt*NIR with those in *Af*NIR and CuNIR from *Achromobacter cycloclastes* (*Ac*NIR).The

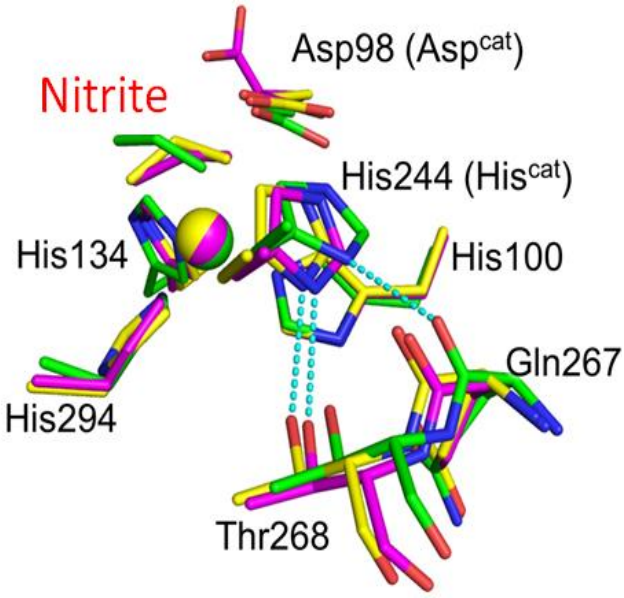

Figure 2-3. Comparison of the coordination mode of nitrite and the environment around the T2Cu site. Wat1 between Asp^{cat} and His^{cat} is omitted for clarity. Three coordinating N$^{\varepsilon}$ atoms of His100, His134, and His294 and Cu ions are superimposed. Oxygen and nitrogen atoms are represented by red and blue sticks, respectively, other than those in the nitrite molecules. Carbon atoms are colored by green, yellow, magenta in *Gt*NIR, *Af*NIR (PDB code 1SJM) and *Ac*NIR (PDB code 2BWI) respectively. H-bonds are represented by cyan dashed lines.

N$^{\delta 1}$ atom of His244 in *Gt*NIR forms a hydrogen bond with the carbonyl oxygen of Gln267 whereas the N$^{\delta 1}$ atoms of corresponding His^{cat} in *Af*NIR and *Ac*NIR are connected to the O$^{\gamma 1}$ atom of threonine. The former conformation of His^{cat} observed in *Gt*NIR henceforth will be referred to as a "horizontal" conformation and the latter observed in *Af*NIR and *Ac*NIR as a "vertical" conformation. Threonine connected to His^{cat} in the vertical conformation is highly conserved in most CuNIRs except CuNIRs from *Neisseria gonorrhoeae* (*Ng*NIR) (42) and an ammonia-oxidizing bacterium, *Nitrosomonas europaea* (*Ne*NIR) (43) in which the threonyl residues are replaced by seryl ones.

In the WT structure, a partially occupied chloride ion (70 % occupancy) is bound to the T2Cu center with a Cl-Cu distance of 2.22 Å. The chloride ion is unusually close to a nearby fully occupied water molecule (Wat6) with a distance of 3.05 Å, which is shorter than the sum of the van der Waals radii of Cl and O atoms. Formic acid in WT-formate was bound to the T2Cu center in the η^1-O coordination manner but with occupancy of

50 %.

The backbone structure located above the T2Cu site in *Gt*NIR differs from those in almost all CuNIRs (Figure 2-4A). A single known exception, which has the same backbone structure as *Gt*NIR, is recently-reported *Ne*NIR. This region is hereinafter referred to as a "cover loop" for convenience. The unique structure of the cover loop provides a distinct shape of the substrate pocket from other typical CuNIRs (Figure 2-4B). As can be seen in Figure 2-4A, Phe109 on the cover loop extends just above Asp98. The hydrogen atom on the C^{α} atom of Asp98 can form a CH-π hydrogen bond with the aromatic ring of Phe109.

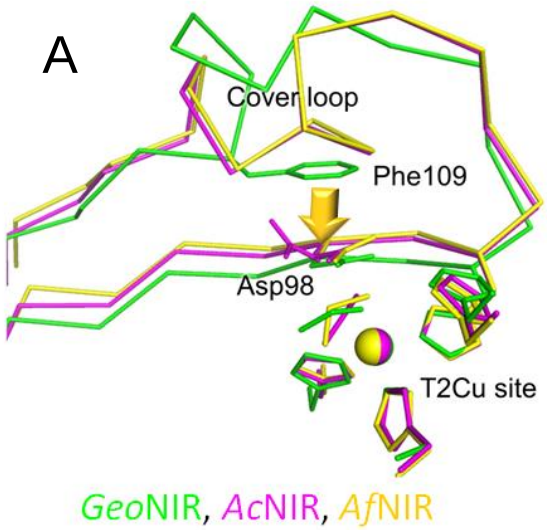

Figure 2-4. (A) Comparison of the environment above the T2 Cu site of *Gt*NIR (green) with *Af*NIR (yellow) and *Ac*NIR (magenta). (B) Molecular surfaces around the T2Cu site and the substrate pockets of *Gt*NIR (left) and *Ax*NIR (right, PDB code 1OE1). The different monomers are shown in different colors.

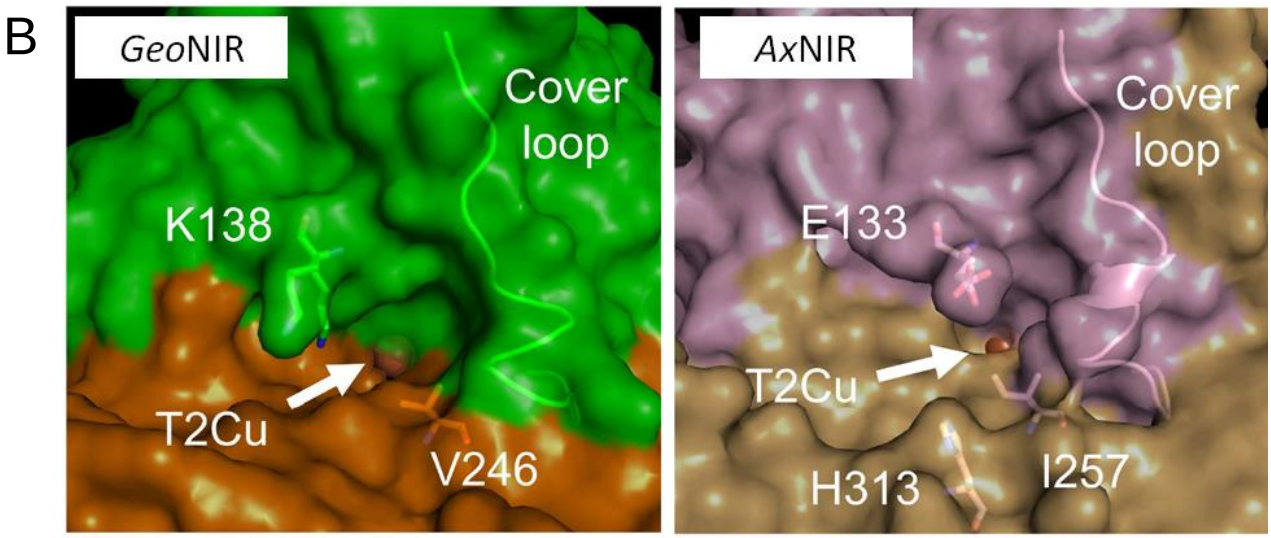

2.3.2. Accessibility of solvent molecules to the T2Cu site

On a wall of the substrate channel in *Gt*NIR, as with other CuNIRs, sit the hydrophobic residues: Pro106, Val140, Val246, Pro290, Val292, Phe296, Ala299, Val304, and Met306. Positive-charged Lys138 is located at the entrance of the substrate channel (Figure 2-4B). In *Ax*NIR, two polar residues, Glu133 and His313, are positioned at the entrance of the substrate pocket, both of which are thought to be involved in the uptake of small molecules including the substrate (44, 45) (Figure 2-4B). *Geobacillus* CuNIR is the first natural CuNIR which has valine, Val246, instead of isoleucine above the T2Cu center. Ile257 above the T2Cu center in *Ax*NIR and the equivalent isoleucine in other CuNIRs are thought to be key residues involved in controlling the binding mode of the substrate/intermediate and discriminating the substrate from other small molecules (46-48). Replacement of isoleucine with valine had no significant effect on activity and the binding mode of nitrite (46). However, it is obvious that a combination of the difference of the cover loop described above and existence of valine instead of isoleucine will provide a wider substrate channel (Figure 2-4B) which can accommodate more water molecules than other CuNIRs (channel A in Figure 2-5). Although *Ne*NIR has the same type of cover loop as *Gt*NIR, Met128 in *Ne*NIR at the other side of isoleucine above the T2Cu site yields a bottleneck (43). Thus, *Geobacillus* CuNIR has the most spacious substrate pocket in all known CuNIRs.

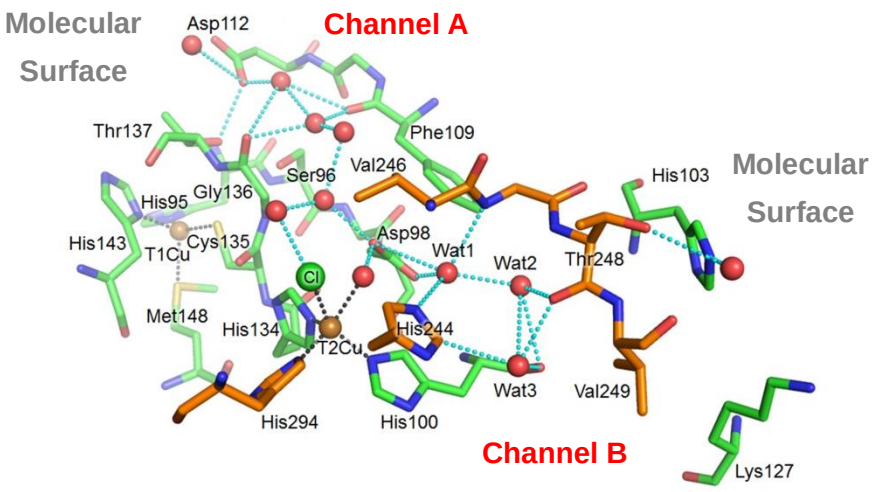

Figure 2-5. H-bonding networks in *Gt*NIR (dotted cyan lines). Residues originating from an adjacent monomer of the same trimer are shown in orange. Cu ions are shown as brown spheres, and water molecules red spheres. Distances from Cu atoms to coordinating protein atoms are shown as dotted black lines.

Nitrite reduction requires two protons and all CuNIRs contain a so-called "proton channel", which lines up water molecules from the molecular surface to the catalytic site so as to effectively supply protons to the catalytic site (18, 49, 50). A putative proton channel (channel A) is composed of water molecules located along the side of the substrate channel in *Gt*NIR (Figure 2-5). *Ax*NIR has two proton channels, channel A and B (Figure 2-6).

There exists Asn90 in channel A of *Ax*NIR, which is one of the most important residues to sustain a water network. An N90S mutant of *Ax*NIR showed a serious decrease of activity because of disruption of a hydrogen bond network (50). By comparison, *Gt*NIR has Ser96 at the same position as Asn90 of *Ax*NIR, and Ser96 is not utilized to construct the hydrogen bond network. Instead, the network in *Gt*NIR is maintained by the carbonyl oxygen atoms of Phe109 and Gly136 juxtaposed to Cys135 (Figure 2C). Gly136 and Thr137 are connected via a peptide bond and the amide nitrogen of Thr137 forms a hydrogen bond with the S atom of Cys135 (3.45 Å). That is, channel A is connected to the T1Cu site albeit indirectly. Incidentally, this region is quite close to the region where CuNIR and an electron-donor protein interact with each other (8, 10). Channel B in

*Gt*NIR is blocked up by hydrophobic Val249 at the middle of channel B although in *Ax*NIR, the equivalent residue His254 maintains the flow of protons in the channel (Figure 2-5).

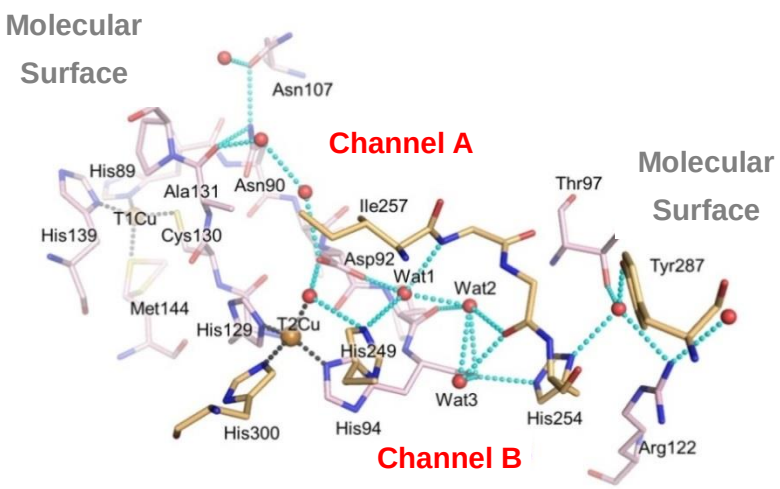

Figure 2-6. H-bonding networks in *Ax*NIR. H-bond networks are indicated by dotted cyan lines. Residues originating from an adjacent monomer are shown in light-orange. Cu ions are shown as brown spheres, and water molecules as red spheres. Distances from Cu atoms to coordinating protein atoms are shown as dotted black lines.

2.3.3. Tight hydrogen bond networks around the T2Cu site

Water molecules in the substrate pocket of *Gt*NIR make tighter hydrogen bond networks than other CuNIRs. Wat1 bridging Asp98 and His244 can form hydrogen bonds with the $O^{\delta 2}$ atom as well as the $O^{\delta 1}$ atom of Asp98 (Figure 2-7A, Table 2). Wat1 in other CuNIRs such as *Ax*NIR can form only one hydrogen bond with Asp^{cat} because Wat1 is about 3.9 Å away from the $O^{\delta 2}$ atom of Asp^{cat} (Figure 2-7C). In C135A-NO_2, Wat1 remains at the position where it can be connected to both $O^{\delta 1}$ and $O^{\delta 2}$ atoms of Asp98 through hydrogen bonds (Figure 2-7B). The distance between the $O^{\delta 1}$ atom and Wat1 in C135A-NO_2 is longer than in WT; conversely, the distance between the $O^{\delta 2}$ atom and Wat1 in C135A-NO_2 is shorter than in WT (Table 2). In all CuNIRs Wat1 is also connected to Wat2. Electron density observed around Wat2 in data of WT and WT-formate shows an ellipsoidal form, which indicates that Wat2 adopts two conformations with 50 % occupancy (Wat2A and Wat2B in Figure 2-7A). Wat2 can also be linked to Wat3 and the carbonyl oxygen atoms of Phe99, Val102, Thr248, and ligand

His100 via hydrogen bonding. Although Wat3 is found in all CuNIRs, Wat3 in *Gt*NIR is peculiar; that is, it is so close to the $C^{\varepsilon 1}$ atom of His244 that the distance between two atoms (3.12 Å in WT and 3.03 Å in C135A-NO_2) are shorter than the sum of the van der Waals radii of C and O atoms. There was no alternative conformer of His244 in which the imidazole ring flips 180 degrees because the $C^{\delta 1}$ atom of the conformer would be located ~2.6 Å away from the carbonyl oxygen atom of Gln267. The short distance between Wat3 and the $C^{\varepsilon 1}$ atom of His244 indicates the existence of a CH-O hydrogen bond. Since a typical donor-acceptor distance of CH-O hydrogen bonding is 3.2-3.6 Å,

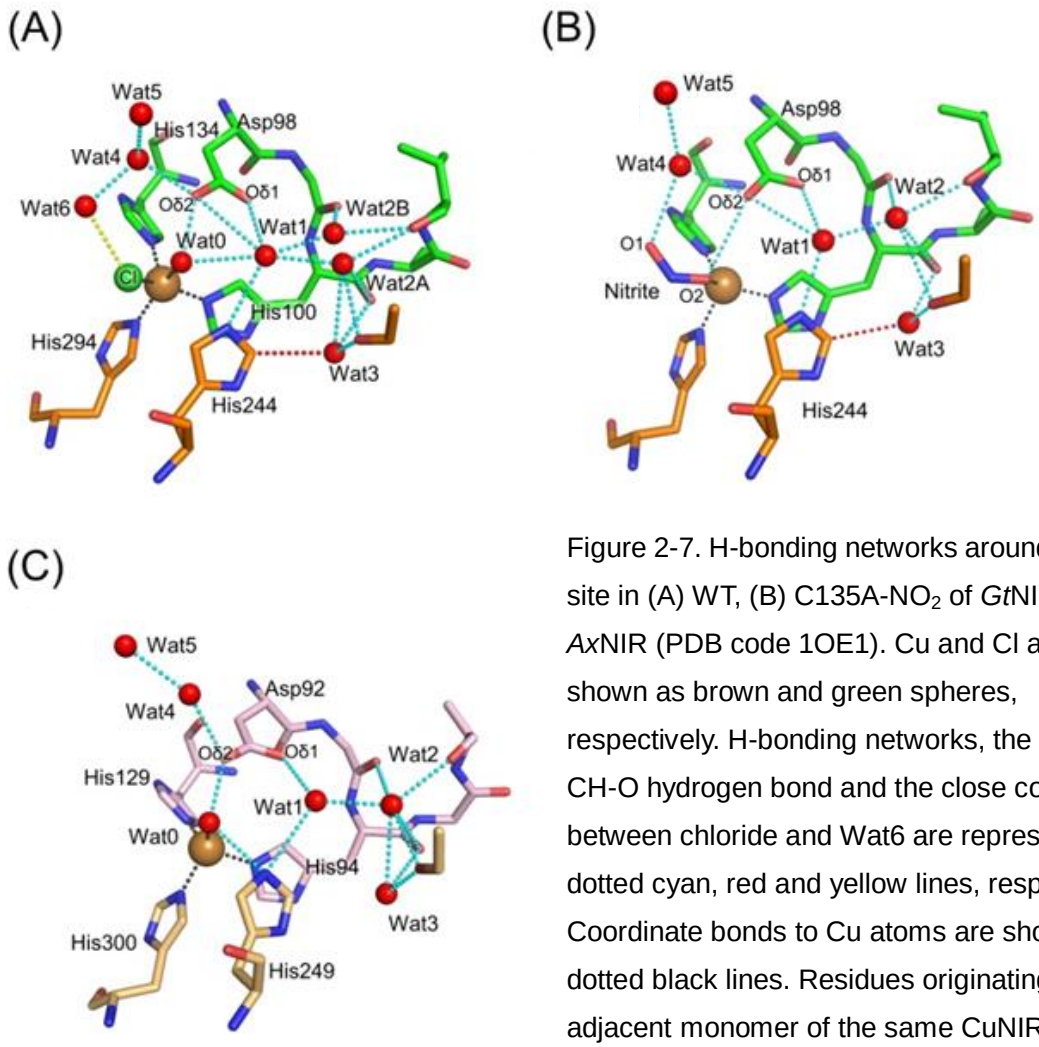

Figure 2-7. H-bonding networks around the T2Cu site in (A) WT, (B) C135A-NO_2 of *Gt*NIR, and (C) *Ax*NIR (PDB code 1OE1). Cu and Cl atoms are shown as brown and green spheres, respectively. H-bonding networks, the unusual CH-O hydrogen bond and the close contact between chloride and Wat6 are represented by dotted cyan, red and yellow lines, respectively. Coordinate bonds to Cu atoms are shown as dotted black lines. Residues originating from an adjacent monomer of the same CuNIR trimer are shown in orange (A, B) or light orange (C).

the CH-O hydrogen bond between Wat3 and the $C^{\varepsilon 1}$ atom of His244 is classified into a short and relatively strong CH-O hydrogen bond (51). Wat3 is also connected to the carbonyl oxygen atom of ligand His100.

Crystal structures of oxidized CuNIRs show a water molecule axially coordinated to the T2Cu atom (Wat0 shown in Figure 2-7A, 2-7C). Wat0 usually forms a hydrogen bond with the $O^{\delta 2}$ atom of Asp^{cat}. As described above, the WT structure of *Gt*NIR accommodates not only Wat0 but also chloride. This chloride is connected to Wat6 specific to *Gt*NIR and linked to Asp98 and Wat5 through Wat4. The near atomic resolution data of WT shows that the bond lengths between the C^{γ} atom and two O^{δ} atoms of Asp98 are different: 1.24 (C^{γ}-$O^{\delta 1}$) and 1.33 (C^{γ}-$O^{\delta 2}$) Å, respectively. This difference in bond lengths is significantly larger than the value of estimated coordinate error (Table 1), indicating that a negative charge on the carboxyl moiety is localized and the $O^{\delta 2}$ atom is protonated (52, 53). On the other hand, the carboxyl group in WT-formate is no longer protonated because WT-formate shows no significant difference between those lengths: 1.23 (C^{γ}-$O^{\delta 1}$) and 1.26 (C^{γ}-$O^{\delta 2}$) Å, respectively. These two bond lengths are also not different in the C135A-NO_2 structure: 1.23 (C^{γ}-$O^{\delta 1}$) and 1.26 (C^{γ}-$O^{\delta 2}$) Å, respectively. However, the coordinate error of C135A-NO_2 was too large to judge whether the two bond lengths are truly equivalent. When nitrite binds to the T2Cu center, Wat0 and Wat6 are expelled and instead, the O2 and O1 atoms of nitrite can form hydrogen bonds with the $O^{\delta 2}$ atom of Asp98 and Wat4, respectively. Electron density reveals that Wat2 occupies only one position in C135A-NO_2.

2.4. Discussion

2.4.1. The rigid and compacted catalytic site in *Gt*NIR compels the unique η^1-O nitrito Cu complex

We made the C135A mutant to obtain the crystal structure in complex with NO_2^- as it can never be reduced to yield NO. The T1Cu and T2Cu sites in the C135A mutant are not directly connected hence intra-copper ET must be inhibited. Blocking intramolecular ET leads to observation of fully occupied nitrite on the T2Cu center. However, unexpectedly, the observed binding mode of nitrite in the C135A structure was unique. Our present structure is the first case that the η^1-O nitrito complex is observed in the wild type T2Cu site of CuNIR. Following, we discuss the reason the η^1-O coordination manner of nitrite was observed in C135A-NO_2.

Asp^{cat} located above the T2Cu site in *Af*NIR and *Ac*NIR is known to be able to adopt two conformations (Figure 2-3). Antonyuk *et al.* annotated them as a proximal and gatekeeper conformation (18). The proximal conformation is also found in *Gt*NIR. In *Ac*NIR, this conformation results in very close contact between the $O^{\delta 2}$ atom of Asp^{cat} and the atoms of nitrite. Antonyuk *et al.* concluded that when Asp^{cat} adopts this position, there should be a water molecule (Wat0) at the T2Cu site in place of nitrite because, in the extreme case, the $O^{\delta 2}$ atom of Asp^{cat} is only 1.9 Å away from the O2 atom of nitrite. In other words, Asp^{cat} has to change its conformation from proximal to gatekeeper to accommodate nitrite at the catalytic site. However, for *Af*NIR, although some structures with small molecules at the T2Cu site demonstrate the gatekeeper conformation of Asp^{cat} (47), nitrite can bind to the T2Cu center in the η^2-O,O side-on manner without collision with Asp^{cat} in the proximal conformation (17) (Figure 2-3). This inconsistency can be resolved when the conformation of the other catalytic residue His^{cat} is considered.

His^{cat} in both *At*NIR and *Ac*NIR adopts a vertical conformation that interacts with nearby threonine (Figure 2-3), which creates a wider space at the catalytic site than the case when His^{cat} adopts a horizontal conformation in which a hydrogen bond is formed with the carbonyl oxygen atom of the main chain. Consequently, *At*NIR is able to accommodate nitrite at the catalytic center without adopting the gatekeeper conformation of Asp^{cat}. Conversely, *Gt*NIR cannot adopt the gatekeeper conformation of Asp98 or the vertical conformation of His244 probably because of steric hindrance created by Phe109 on the cover loop and the unusual CH-O hydrogen bond with Wat3, respectively. It is known that not only classical hydrogen bonding but also non-classical hydrogen bonding including CH-O and CH-π hydrogen bonding is one of the important keys to thermostability (54). As a result, the catalytic site is more rigid and the space above the T2Cu site is more compacted in *Gt*NIR than in other CuNIRs. The rigid and compacted catalytic site of *Gt*NIR, therefore, works for *G. thermodenitrificans*, which grows between 45 °C and 73 °C (optimum is 65 °C) (55). However, the rigid and compacted catalytic site will easily result in steric hindrance for nitrite in an environment where the thermal mobility of atoms is restricted. Since, in our experiment, crystallization and soaking of nitrite were performed at 293 K (20 °C) and the diffraction data was collected at 100 K (−173 °C), nitrite would not be able to intrude into the narrow space above the T2Cu site. Thus, it has no choice but to bind in the η^1-O coordination manner.

The η^1-O binding mode was also observed in the WT-formate structure. Although, during the crystallization of WT-formate, the *Gt*NIR molecules were exposed to a high concentration (200 m*M*) of formate for long periods of time (5 days), formate could not bind to the T2Cu atom in a bidentate manner. This fact indicates that it is difficult for a

nonlinear molecule composed of three atoms, such as nitrite and formate, to bind to the T2Cu center of *Gt*NIR in the side-on η^2-O,O mode. It is also worth noting that the bulkiness of ligands is correlated with the binding mode of nitrite in the Cu(II)-NO_2^- model complexes (56). The sterically bulky complex adopts an asymmetric η^2-O,O binding mode whereas the less sterically bulky complex shows a symmetric η^2-O,O nitrite coordination. When taken together, it is reasonable that the steric obstruction at the catalytic site in *Gt*NIR compels substrate to bind to the T2Cu site in an asymmetric monodentate coordination manner.

2.4.2. The role of His244^{cat} in the reaction mechanism

There is a good possibility that NO_2^- can be reduced to NO from the η^1-O binding mode

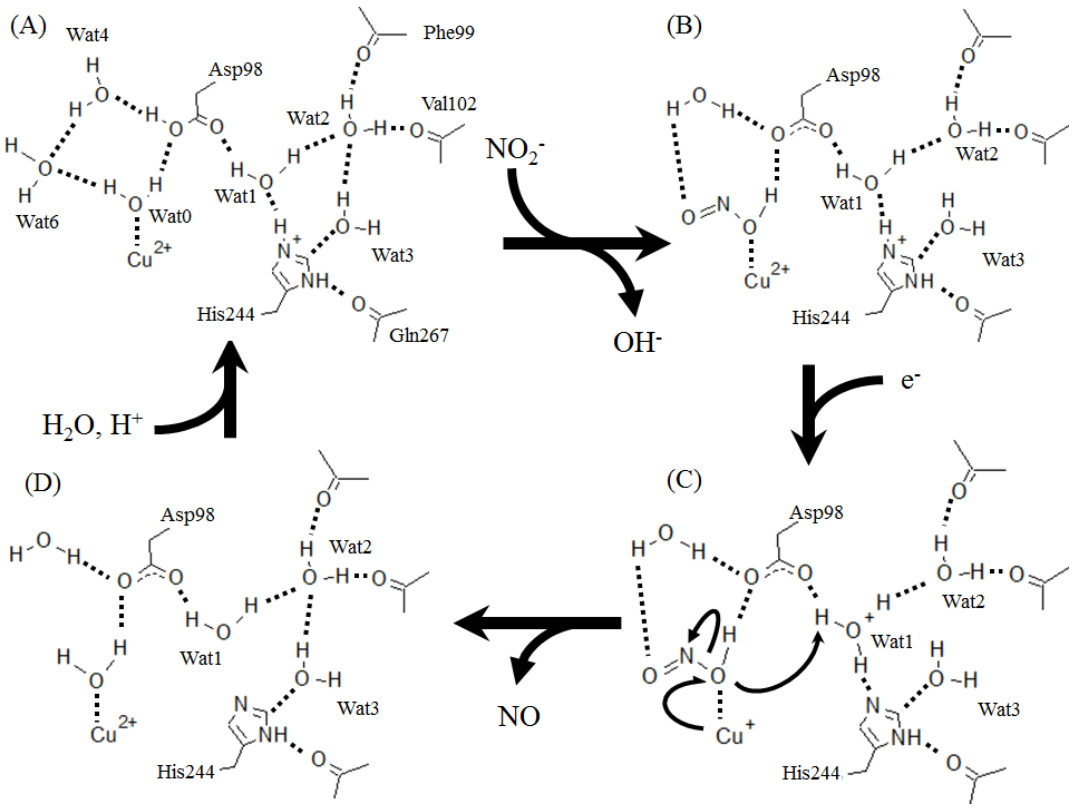

Scheme 2-1 Proposed mechanism of nitrite reduction by *Gt*NIR at ambient temperature.

since *Geobacillus* CuNIR can also function at room temperature (28). The first step in which water on the T2Cu atom (Wat0) is substituted with nitrite is similar to the usual mechanism except nitrite adopts the monodentate mode (Scheme 2-1A, 2-1B). Our present crystal structures imply that the $O^{\delta 2}$ atom of Asp98 is protonated in the resting state while it is deprotonated in the substrate-bound form. The proton may move from Asp98 to nitrite to produce HONO, and a hydrogen bond between Asp98 and nitrite is formed as is observed in the crystal structure of C135A-NO_2. At the same time as the electron transferred from the T1Cu site to the T2Cu site moves on the oxygen atom of nitrite, nitrite has to gain the second proton to produce H_2O and NO. In the mechanism proposed by Suzuki and coworkers (14), the second proton is provided directly by the $N^{\varepsilon 2}$ atom of His^{cat}. However, our present crystal structures reveal that the imidazole ring of His244 in *Gt*NIR is fixed and scarcely moves, indicating that His244 is not able to directly give a proton to nitrite. Instead, the proton on the $N^{\varepsilon 2}$ atom of His244 is thought to first be shifted to Wat1 to produce a hydronium cation and then the proton is relayed to nitrite as is pointed out by Murphy and Boulanger (16). In the case of *Gt*NIR, the delivery of the proton from Wat1 to nitrite may be mediated by the $O^{\delta 2}$ atom of Asp98 because Wat1 moves closer to the $O^{\delta 2}$ atom when the substrate binds to the T2Cu center than in the resting state.

We must admit that it may be feasible for nitrite to bind to the T2Cu site in an η^2-O,O side-on manner at high temperatures whereby the high flexibility of the protein structure may widen the catalytic site and allow accommodation of bidentate nitrite. His244 should be in focus in considering a reaction mechanism at high temperatures. The imidazole ring of it should be able to easily rotate at high temperatures to form a hydrogen bond with Thr268. This threonine must be an important one for enzymatic

function because this residue is highly conserved in most CuNIRs except *Ng*NIR and *Ne*NIR in which serine exists in place of threonine. Although serine can form a hydrogen bond with His^{cat} as with threonine, in some instances it does not. Serine can adopt more conformations in the protein structure than threonine because it is sterically less bulky than threonine. As a matter of fact, the imidazole ring of His227^{cat} in *Ne*NIR only has to rotate to form a hydrogen bond with Ser251 because the Oγ atom of Ser251 points to His227^{cat}, whereas the Oγ atom of Ser263 in *Ng*NIR somehow faces the opposite direction of His240^{cat} and hence it is less probable that Ser263 forms a hydrogen bond with His240^{cat}. The activity of *Ne*NIR is similar to other CuNIRs (43); on the other hand, the activity of *Ng*NIR is approximately half that measured for *Af*NIR using the same assay system (42). These facts support the significance of forming a hydrogen bond between His^{cat} and threonine (or serine), which has been an ignored residue for long.

2.4.3. The flow of protons required for nitrite reduction

All CuNIRs have proton channels in which water molecules are spotted for the effective supply of protons to the catalytic site because nitrite reduction consumes two protons. Some CuNIRs such as *Ax*NIR have two proton channels, channel A and channel B. However, proton channel B in *Gt*NIR is blocked-up because of the presence of Val249 in the middle of the channel. However, channel B of *Ne*NIR is filled with water molecules regardless of the existence of Ile232 at the same position. Two novel CuNIRs from *Pseudoalteromonas haloplanktis* (*Ph*NIR) (7) and *Ralstonia pickettii* (*Rp*NIR) (23) have been recently reported, and both have isoleucine in channel B as with *Ne*NIR. Interestingly, *Ph*NIR has a blocked-up channel B like *Gt*NIR, while *Rp*NIR contains a

fully hydrated one like *Ne*NIR. Crystal structures of *Rp*NIR and *Ne*NIR imply that the channel B of *Gt*NIR can be opened up to function as long as Val249 changes its conformation. Nevertheless, we believe that channel A plays the principal role in *Gt*NIR for the following reasons. First, channel A is thought to be the primary one in *Ax*NIR because a mutant, H254F, in which channel B was broken, showed no significant decrease of activity (50). Secondly, the conformation of Val249 is restricted by nearby bulky Lys127 (Figure 2-5), which occupies the entrance of channel B and forms a salt bridge with Asp251. Thus, it is difficult for Val249 to assume the conformation observed for Ile232 in *Ne*NIR, which affords enough space for the water molecules lined up in channel B. Lastly, channel A must be profitable for the proton-coupled ET reaction. The end of channel A at the molecular surface of *Gt*NIR is close to an interaction interface between CuNIR and an electron-donor protein. In addition, two water molecules in the channel A of *Gt*NIR are connected to the carbonyl oxygen atom of Gly136 next to the ligand residue of the T1Cu center, Cys135. C135A-NO_2 showed a small shift of the carbonyl oxygen atom of Gly136 because of the perturbation of the T1Cu site. On the opposite side of the oxygen atom of Gly136 exists that of Phe109, which is located above catalytic Asp98. These observations suggest that changes in environmental conditions around the T1Cu site upon docking of the electron-donor, information about redox states of the T1Cu site, and states around the catalytic residue are efficiently transmitted to channel A. Thus, usage of channel A will facilitate intramolecular ET coupled with proton transfer in *Gt*NIR.

Instead, the blocked-up channel B of *Gt*NIR may act as a pool of protons. Indeed, Wat2 is surrounded by many proton-acceptor atoms, the carbonyl oxygen atoms of Phe99, His100, Val102 and Thr248, all located within distances of typical hydrogen bonding,

which indicates that Wat2 can easily receive a proton to become a hydronium ion. Thus, the proton on Wat1 in Scheme 2-1C is thought to be in an equilibrium state between Wat1 and Wat2; that is, the proton on Wat1 can be transferred to and transiently stored on Wat2. The replacement of hydrogen bonds is coupled with the states of the T2Cu site partly because Wat2 can directly form a hydrogen bond with ligand His100. For example, when the axial ligands of the T2Cu center show only one predominant structure as is seen in C135A-NO_2, the position of Wat2 is fixed and it does not form a hydrogen bond with Wat3 (Figure 2-7A, 2-7B), which forms the unusual CH-O hydrogen bond with His244 and is also linked to ligand His100. Considering these observations, although channel B is truncated in *Gt*NIR and hence does not supply protons from bulk water, the hydrogen bond network sustained by water molecules in this channel can be partly involved in proton-coupled ET. Hydrogen bond networks related to Wat2 and Wat3 have drawn little attention until now; however, we strongly believe that they are an important piece of the puzzle of mechanism because all CuNIRs have Wat2 and Wat3.

Our proposed mechanism is summarized as follows. First, nitrite binds to the T2Cu atom in the η^1-O coordination manner due to restricted conformations of Asp98 and His244. However, our result does not exclude the possibility that nitrite adopts the η^2-O,O binding mode at high temperatures. The first proton is provided by Asp98 when Wat0 is substituted by nitrite, and the second one is supplied by His244 or Wat2, but through Wat1, after intramolecular ET, which is coupled with replacement of hydrogen bonds around the T2Cu site. NO is generated and released without forming the copper-nitrosyl complex. The final step is reconstruction of the hydrogen bond networks by a water molecule and a proton supplied through channel A (Scheme 2-1D, 2-1A).

Molecular dynamics simulations showed that the rotation of the imidazole ring of His244 was related to whether nitrite can go into the narrow space above the T2Cu site to bind to the copper atom in the η^2-O,O binding mode. The more detailed QM/MM calculation will help to support the validity of our hypothesis. This experiment is in progress and the results will be reported in due course.

References

1. Zumft, W. G. (1997). Cell biology and molecular basis of denitrification. *Microbiol. Mol. Biol. Rev.* **61**, 533-616.
2. Gruber, N. & Galloway, J. N. (2008). An Earth-system perspective of the global nitrogen cycle. *Nature* **451**, 293-6.
3. Galloway, J. N., Townsend, A. R., Erisman, J. W., Bekunda, M., Cai, Z., Freney, J. R., Martinelli, L. A., Seitzinger, S. P. & Sutton, M. A. (2008). Transformation of the Nitrogen Cycle: Recent Trends, Questions, and Potential Solutions. *Science* **320**, 889-892.
4. Suzuki, S., Kataoka, K., Yamaguchi, K., Inoue, T. & Kai, Y. (1999). Structure–function relationships of copper-containing nitrite reductases. *Coordination Chemistry Reviews* **190-192**, 245-265.
5. Vries, S. d. & Schröder, I. (2008). *Thermophiles: Biology and Technology at High Temperatures*, CRC Press Boca Raton, Florida.
6. Matsumoto, Y., Tosha, T., Pisliakov, A. V., Hino, T., Sugimoto, H., Nagano, S., Sugita, Y. & Shiro, Y. (2012). Crystal structure of quinol-dependent nitric oxide reductase from Geobacillus stearothermophilus. *Nat Struct Mol Biol* **19**, 238-45.
7. Tsuda, A., Ishikawa, R., Koteishi, H., Tange, K., Fukuda, Y., Kobayashi, K., Inoue, T. & Nojiri, M. (2013). Structural and mechanistic insights into the electron flow through protein for cytochrome c-tethering copper nitrite reductase. *J Biochem* **154**, 51-60.
8. Nojiri, M., Koteishi, H., Nakagami, T., Kobayashi, K., Inoue, T., Yamaguchi, K. & Suzuki, S. (2009). Structural basis of inter-protein electron transfer for nitrite reduction in denitrification. *Nature* **462**, 117-20.
9. Koteishi, H., Nojiri, M., Nakagami, T., Yamaguchi, K. & Suzuki, S. (2009).

Cytochrome c551 Is a Mediator of Electron Transfer between Copper-Containing Nitrite Reductase and Azurin in a Denitrifying Bacterium, Achromobacter xylosoxidans. *Bulletin of the Chemical Society of Japan* **82**, 1003-1005.

10. Vlasie, M. D., Fernandez-Busnadiego, R., Prudencio, M. & Ubbink, M. (2008). Conformation of pseudoazurin in the 152 kDa electron transfer complex with nitrite reductase determined by paramagnetic NMR. *J Mol Biol* **375**, 1405-15.
11. Kukimoto, M., Nishiyama, M., Ohnuki, T., Turley, S., Adman, E. T., Horinouchi, S. & Beppu, T. (1995). Identification of interaction site of pseudoazurin with its redox partner, copper-containing nitrite reductase from Alcaligenes faecalis S-6. *Prot. Engin.* **8**, 153-158.
12. Abraham, Z. H. L., Smith, B. E., Howes, B. D., Lowe, D. J. & Eady, R. R. (1997). pH-dependence for binding a single nitrite ion to each type-2 copper centre in the copper-containing nitrite reductase of Alcaligenes xylosoxidans. *Biochem. J.* **324**, 511–516.
13. Murphy, M. E. P., Turley, S. & Adman, E. T. (1997). Structure of Nitrite Bound to Copper-containing Nitrite Reductase from Alcaligenes faecalis. *Journal of Biological Chemistry* **272**, 28455-28460.
14. Kataoka, K., Furusawa, H., Takagi, K., Yamaguchi, K. & Suzuki, S. (2000). Functional Analysis of Conserved Aspartate and Histidine Residues Located Around the Type 2 Copper Site of Copper-Containing Nitrite Reductase. *J. Biochem* **127**, 345-350.
15. Boulanger, M. J., Kukimoto, M., Nishiyama, M., Horinouchi, S. & Murphy, M. E. (2000). Catalytic roles for two water bridged residues (Asp-98 and His-255) in the active site of copper-containing nitrite reductase. *J Biol Chem* **275**, 23957-64.
16. Boulanger, M. J. & Murphy, M. E. P. (2001). Alternate Substrate Binding Modes to Two Mutant (D98N and H255N) Forms of Nitrite Reductase from Alcaligenes faecalis S-6: Structural Model of a Transient Catalytic Intermediate. *Biochemistry* **40**, 9132-9141.
17. Tocheva, E. I., Rosell, F. I., Mauk, A. G. & Murphy, M. E. (2004). Side-on copper-nitrosyl coordination by nitrite reductase. *Science* **304**, 867-870.
18. Antonyuk, S. V., Strange, R. W., Sawers, G., Eady, R. R. & Hasnain, S. S. (2005). Atomic resolution structures of resting-state, substrate- and product-complexed Cu-nitrite reductase provide insight into catalytic mechanism. *Proc Natl Acad Sci U S A* **102**, 12041-12046.
19. Brenner, S., Heyes, D. J., Hay, S., Hough, M. A., Eady, R. R., Hasnain, S. S. & Scrutton, N. S. (2009). Demonstration of proton-coupled electron transfer in the

copper-containing nitrite reductases. *J Biol Chem* **284**, 25973-83.

20. Leferink, N. G., Han, C., Antonyuk, S. V., Heyes, D. J., Rigby, S. E., Hough, M. A., Eady, R. R., Scrutton, N. S. & Hasnain, S. S. (2011). Proton-coupled electron transfer in the catalytic cycle of Alcaligenes xylosoxidans copper-dependent nitrite reductase. *Biochemistry* **50**, 4121-31.
21. Jones, C. M., Stres, B., Rosenquist, M. & Hallin, S. (2008). Phylogenetic analysis of nitrite, nitric oxide, and nitrous oxide respiratory enzymes reveal a complex evolutionary history for denitrification. *Mol Biol Evol* **25**, 1955-66.
22. Kim, S. W., Fushinobu, S., Zhou, S., Wakagi, T. & Shoun, H. (2009). Eukaryotic nirK genes encoding copper-containing nitrite reductase: originating from the protomitochondrion? *Appl Environ Microbiol* **75**, 2652-8.
23. Antonyuk, S. V., Han, C., Eady, R. R. & Hasnain, S. S. (2013). Structures of protein-protein complexes involved in electron transfer. *Nature* **496**, 123-6.
24. Manachini, P. L., Mora, D., Nicastro, G., Parini, C., Stackebrandt, E., and, R. P. & Fortina, M. G. (2000). Bacillus thermodenitrificans sp. nov., nom. rev. *International Journal of Systematic and Evolutionary Microbiology* **50**, 1331-1337.
25. Romano, I., Poli, A., Lama, L., Gambacorta, A. & Nicolaus, B. (2005). Geobacillus thermoleovorans subsp. stromboliensis subsp. nov., isolated from the geothermal volcanic environment. *J. Gen. Appl. Microbiol.* **51**, 183-189.
26. Mishima, M., Iwata, K., Nara, K., Matsui, T., Shigeno, T. & Omori, T. (2009). Cultivation characteristics of denitrifi cation by thermophilic Geobacillus sp. strain TDN01. *J. Gen. Appl. Microbiol.* **55**, 81-86.
27. Fukuda, Y., Tamada, T., Takami, H., Suzuki, S., Inoue, T. & Nojiri, M. (2011). Cloning, expression, purification, crystallization and preliminary X-ray crystallographic study of GK0767, the copper-containing nitrite reductase from Geobacillus kaustophilus. *Acta Crystallogr Sect F Struct Biol Cryst Commun* **67**, 692-5.
28. Fukuda, Y., Nojiri, M., Yamaguchi, K. & Suzuki, S. (2009). Structure and function of a copper-containing nitrite reductase from a marine thermophilic Gram-positive bacterium, Geobacillus kaustophilus HTA426. *J. Biol. Inorg. Chem.* **14**, S201.
29. Takami, H., Takaki, Y., Chee, G. J., Nishi, S., Shimamura, S., Suzuki, H., Matsui, S. & Uchiyama, I. (2004). Thermoadaptation trait revealed by the genome sequence of thermophilic Geobacillus kaustophilus. *Nucleic Acids Res* **32**, 6292-303.
30. Feng, L., Wang, W., Cheng, J., Ren, Y., Zhao, G., Gao, C., Tang, Y., Liu, X., Han, W., Peng, X., Liu, R. & Wang, L. (2007). Genome and proteome of long-chain alkane degrading Geobacillus thermodenitrificans NG80-2 isolated from a deep-subsurface

oil reservoir. *Proc Natl Acad Sci U S A* **104**, 5602-7.

31. Hough, M. A., Antonyuk, S. V., Strange, R. W., Eady, R. R. & Hasnain, S. S. (2008). Crystallography with online optical and X-ray absorption spectroscopies demonstrates an ordered mechanism in copper nitrite reductase. *J Mol. Biol.* **378**, 353-61.
32. Hough, M. A., Ellis, M. J., Antonyuk, S., Strange, R. W., Sawers, G., Eady, R. R. & Samar Hasnain, S. (2005). High resolution structural studies of mutants provide insights into catalysis and electron transfer processes in copper nitrite reductase. *J Mol Biol* **350**, 300-9.
33. Otwinowski, Z. & Minor, W. (1997). [20] Processing of X-ray diffraction data collected in oscillation mode. *Methods Enzymol.* **276**, 307-326.
34. A.Vagin & A.Teplyakov. (1997). MOLREP: an Automated Program for Molecular Replacement. *J. Appl. Cryst.* **30**, 1022-1025.
35. Winn, M. D., Ballard, C. C., Cowtan, K. D., Dodson, E. J., Emsley, P., Evans, P. R., Keegan, R. M., Krissinel, E. B., Leslie, A. G., McCoy, A., McNicholas, S. J., Murshudov, G. N., Pannu, N. S., Potterton, E. A., Powell, H. R., Read, R. J., Vagin, A. & Wilson, K. S. (2011). Overview of the CCP4 suite and current developments. *Acta Crystallogr D Biol Crystallogr* **67**, 235-42.
36. Murshudov, G. N., Skubak, P., Lebedev, A. A., Pannu, N. S., Steiner, R. A., Nicholls, R. A., Winn, M. D., Long, F. & Vagin, A. A. (2011). REFMAC5 for the refinement of macromolecular crystal structures. *Acta Crystallogr D Biol Crystallogr* **67**, 355-67.
37. Emsley, P., Lohkamp, B., Scott, W. G. & Cowtan, K. (2010). Features and development of Coot. *Acta Crystallogr D Biol Crystallogr* **66**, 486-501.
38. Laskowski. R. A., MacArthur. M. W., Moss. D. S. and Thornton. J. M. (1993). PROCHECK - a program to check the stereochemical quality of protein structures. *J. App. Cryst.* **26**, 283-291.
39. Chen, V. B., Arendall, W. B., 3rd, Headd, J. J., Keedy, D. A., Immormino, R. M., Kapral, G. J., Murray, L. W., Richardson, J. S. & Richardson, D. C. (2010). MolProbity: all-atom structure validation for macromolecular crystallography. *Acta Crystallogr D Biol Crystallogr* **66**, 12-21.
40. Jiang, F., Conry, R. R., Bubacco, L., Tyeklar, Z., Jacobson, R. R., Karlin, K. D. & Peisach, J. (1993). Crystal structure and electron spin echo envelope modulation study of [Cu(II)(TEPA)(NO2)]PF6 (TEPA = tris[2-(2-pyridyl)ethyl]amine): a model for the purported structure of the nitrite derivative of hemocyanin. *J. Am. Chem. Soc.* **115**, 2093-2102.
41. Komeda, N., Nagao, H., Kushi, Y., Adachi, G.-y., Suzuki, M., Uehara, A. & Tanaka, K.

(1995). Molecular Structure of Nitro- and Nitrito-Copper Complexes as Reaction Intermediates in Electrochemical Reduction of Nitrite to Dinitrogen Oxide. *Bulletin of the Chemical Society of Japan* **68**, 581-589.

42. Boulanger, M. J. & Murphy, M. E. P. (2002). Crystal Structure of the Soluble Domain of the Major Anaerobically Induced Outer Membrane Protein (AniA) from Pathogenic Neisseria: A New Class of Coppercontaining Nitrite Reductases. *Journal of Molecular Biology* **315**, 1111-1127.
43. Lawton, T. J., Bowen, K. E., Sayavedra-Soto, L. A., Arp, D. J. & Rosenzweig, A. C. (2013). Characterization of a Nitrite Reductase Involved in Nitrifier Denitrification. *J Biol Chem*.
44. Dodd, F. E., Beeumen, J. V., Eady, R. R. & Hasnain, S. S. (1998). X-ray Structure of a Blue-copper Nitrite Reductase in Two Crystal Forms. The Nature of the Copper Sites, Mode of Substrate Binding and Recognition by Redox Partner. *Journal of Molecular Biology* **282, 369-382**.
45. Barrett, M. L., Harris, R. L., Antonyuk, S., Hough, M. A., Ellis, M. J., Sawers, G., Eady, R. R. & Hasnain, S. S. (2004). Insights into redox partner interactions and substrate binding in nitrite reductase from Alcaligenes xylosoxidans: crystal structures of the Trp138His and His313Gln mutants. *Biochemistry* **43**, 16311-9.
46. Boulanger, M. J. & Murphy, M. E. (2003). Directing the mode of nitrite binding to a copper-containing nitrite reductase from Alcaligenes faecalis S-6: characterization of an active site isoleucine. *Protein Sci* **12**, 248-56.
47. Tocheva, E. I., Eltis, L. D. & Murphy, M. E. P. (2008). Conserved Active Site Residues Limit Inhibition of a Copper-Containing Nitrite Reductase by Small Molecules. *Biochemistry* **47**, 4452–4460.
48. Merkle, A. C. & Lehnert, N. (2009). The side-on copper(I) nitrosyl geometry in copper nitrite reductase is due to steric interactions with isoleucine-257. *Inorg Chem* **48**, 11504-6.
49. Ellis, M. J., Dodd, F. E., Sawers, G., Eady, R. R. & Hasnain, S. S. (2003). Atomic Resolution Structures of Native Copper Nitrite Reductase from Alcaligenes xylosoxidans and the Active Site Mutant Asp92Glu. *Journal of Molecular Biology* **328**, 429-438.
50. Hough, M. A., Eady, R. R. & Hasnain, S. S. (2008). Identification of the Proton Channel to the Active Site Type 2 Cu Center of Nitrite Reductase: Structural and Enzymatic Properties of the His254Phe and Asn90Ser Mutants. *Biochemistry* **47**, 13547-13553.
51. Desiraju, G. R. & Steiner, T. (1999). *The Weak Hydrogen Bonds in Structural*

Chemistry and Biology, Oxford University Press, Oxford.

52. Fisher, S. J., Blakeley, M. P., Cianci, M., McSweeney, S. & Helliwell, J. R. (2012). Protonation-state determination in proteins using high-resolution X-ray crystallography: effects of resolution and completeness. *Acta Crystallogr D Biol Crystallogr* **68**, 800-9.
53. Ahmed, H. U., Blakeley, M. P., Cianci, M., Cruickshank, D. W., Hubbard, J. A. & Helliwell, J. R. (2007). The determination of protonation states in proteins. *Acta Crystallogr D Biol Crystallogr* **63**, 906-22.
54. Ibrahim, B. S. & Pattabhi, V. (2004). Role of weak interactions in thermal stability of proteins. *Biochem Biophys Res Commun* **325**, 1082-9.
55. Wang, L., Tang, Y., Wang, S., Liu, R. L., Liu, M. Z., Zhang, Y., Liang, F. L. & Feng, L. (2006). Isolation and characterization of a novel thermophilic Bacillus strain degrading long-chain n-alkanes. *Extremophiles* **10**, 347-56.
56. Lehnert, N., Cornelissen, U., Neese, F., Ono, T., Noguchi, Y., Okamoto, K.-i. & Fujisawa, K. (2007). Synthesis and Spectroscopic Characterization of Copper(II)−Nitrito Complexes with Hydrotris(pyrazolyl)borate and Related Coligands. *Inorg. Chem.* **46**, 3916–3933.

Chapter 3
High-temperature and High-resolution X-ray crystallography of *Gt*NIR

Summary

The 1.50 Å resolution structure of *Geo*NIR was determined at 320 K. The overall high-temperature structure was almost the same as the cryogenic structure. However, the number of water molecules located on the molecular surface was smaller in the high-temperature structure than in the cryogenic structure. Moreover, one of the catalytic residues (His244) showed a rotation of its imidazole ring and hence the catalytic site became wider than in the cryogenic structure. The 1.55 Å resolution C135A-nitrite complex structure was also determined at 320 K. Nitrite was found to display a binding mode similar to those observed in other typical CuNIRs, not the η^1-O,O binding mode, which was observed in the cryogenic structure of the C135A-nitrite complex. This is probably because the catalytic site became wide at 320 K. The imidazole ring of His244 was rotated as was observed in the high-temperature structure of WT and Oδ2 atom of Asp98 was moved slightly. This is the first case that substrate's binding mode different between cryogenic and high-temperature structures was revealed by X-ray crystallography.

3.1. Introduction

It is common sense in the field of structural biology that X-ray diffraction experiment has to be carried out at low temperatures (> 100 K) to reduce radiation damages to

crystals (1, 2). More than 95% crystal structures of proteins were determined using X-ray data collected under 100 K. Thus, they are, so to speak, the cryogenic structures. However, recently, it has been revealed that some enzymes show different structures of amino acid residues involved in their enzymatic activities between cryogenic and room-temperature structures (3-5). Therefore, it is unclear whether we can obtain information about intrinsic dynamics of proteins by knowing cryogenic structures, not to mention that of thermostable enzymes. Apparently, it is necessary to solve "high-temperature structures" of them. As commonly-used techniques to know room- or high-temperature structures of biological macromolecules, two methods are popular: the nuclear magnetic resonance (NMR) analysis which can determine the protein structures in solution (6-8) and the hybrid quantum mechanics/molecular mechanics (QM/MM) approach which allow for studying dynamic processes of proteins (9). Unfortunately, these techniques are not perfect. For example, it is difficult, if not impossible, to apply them to CuNIR because it has a high molecular weight (111 kDa in the trimer) and contains several paramagnetic nuclei. In contrast, X-ray crystallography can be applied to any kind of proteins which can be crystalized. Therefore, the novel method, high-temperature and high-resolution X-ray crystallography, was applied to *Geo*NIR because *Geo*NIR can crystallize in the tough and high-quality crystal.

3.2. Methods

Crystals of WT *Gt*NIR and the C135A-nitrite complex were prepared using the method described in chapter 2. The obtained crystals were coated with paraffin oil to avoid drying. MicroLoops and MicroRT X-ray capillaries (MiTeGen) were used to mount the crystals on the goniometer of beamline BL38B1 at SPring-8. Temperature of the

cryostream controller was set to 320 K. All processes after data collection were the same as those described in chapter 2. The data collection and refinement statistics are summarized in Table III-I.

Table III-I. Data collection and refinement statistics

	WT_{hot}	$C135A\text{-}NO2_{hot}$
Data collection		
Space group	*R*3	*R*3
Unit cell		
a, *b* (Å)	116.34	116.30
c (Å)	85.54	85.65
α, *β* (°)	90	90
γ (°)	120	120
Resolution range (Å)	50.0-1.50 (1.53-1.50)[a]	50.0 -1.55 (1.58-1.55)[a]
R_{merge} (%)[b]	7.2 (38.1)	6.6 (40.4)
Completeness (%)	99.8 (100)	96.6 (98.9)
Unique reflections	68,877 (3,458)	60,565 (3,082)
$\langle I/\sigma(I)\rangle$	18.6 (2.0)	22.2 (2.5)
Redundancy	3.7 (3.7)	3.9 (3.7)
Refinement		
Resolution range (Å)	32.6-1.50	34.8-1.55
R_{work} (%)[c] / R_{free} (%)[d]	10.2/13.4	12.5/14.7
RMSD bond length (Å)	0.028	0.030
RMSD bond angle (°)	2.516	2.941
Average *B* (Å^2)	18.6	19.6

[a] Values in parentheses are for the highest-resolution shell.. [b] R_{merge} is calculated as $\Sigma_{hkl}\Sigma_i | I_i(hkl)-\langle I(hkl)\rangle | / \Sigma_{hkl}\Sigma_i I(hkl)$, where $I_i(hkl)$ is the intensity of an individual measurement of the reflection with Miller indices *hkl* and $\langle I(hkl)\rangle$ is the average intensity from multiple observations. [c] $R_{work} = \Sigma_{hkl} | \, | F_{obs} | - | F_{calc} | \, | / \Sigma_{hkl} | F_{obs} |$, where F_{obs} and F_{calc} are the observed and calculated structure-factor amplitudes, respectively. [d] The free *R* factor, R_{free}, is computed in the same manner as R_{work} but using only a small set (5%) of randomly chosen intensities that were not used in the refinement of the model.

3.3. Results

3.3.1. High-temperature structure of WT *Gt*NIR

The high-quality X-ray diffraction data of WT (WT_{hot}) and the C135A-nitrite complex ($C135A\text{-}NO2_{hot}$) were collected up to 1.50 and 1.55 Å resolution, respectively, which is so-called high resolution. Data collection and refinement statistics are summarized in Table. R_{merge} and $<I>/\sigma<I>$ values indicated that there were no significant radiation damages to the crystals. Each length of the cell was about 1 Å elongated under high temperature. The temperature factor (Debye-Waller or *B*-factor) values were 19 and 20 $Å^2$ in WT_{hot} and $C135A\text{-}NO2_{hot}$, respectively, which were larger than those of cryogenic structures (16 $Å^2$), resolution of which is 1.50 Å. The structure of $C135A\text{-}NO2_{hot}$ was determined at 1.55 Å resolution. R_{work} and R_{free} was 10.2 and 13.4%, respectively. These values indicated the final model showed a good agreement with the experimental data.

The RMSD (Cα) between the WT_{hot} and the cryogenic WT structure (PDB 3WKO, WT_{cryo}) was 0.08 Å, which indicates that the difference of temperature did not dramatically affect the overall structure of *Gt*NIR. A water molecule formed a hydrogen bond with one of the histidyl ligand to T1Cu, His143. The corresponding water molecule in other CuNIR is thought to be important for adjusting redox potential of the T1Cu site (ref). As is described in chapter 2, water molecules lined up from the molecular surface to the catalytic site on one side of the substrate pocket (Fig 3-1). However, there was no electron density of solvent molecules on the other side of the substrate pocket. The proton channel B mentioned in chapter 2 was closed because Val249 remained in the same conformation as that observed in the cryogenic structure.

A water molecule (Wat2 in Fig 3-2) which occupied two positions at low temperature, both of which showed 50% occupancy, was fixed at one position at high temperature. Wat1, located between Asp98 and His244, was fixed at low temperature, whereas a component of it with 50% occupancy, which was closer to His244, was observed at 320 K. His244 also displayed two different conformations, in one of which the imidazole ring slightly rotated and the N^{ε} atom were closer to Thr268 than in other conformation.

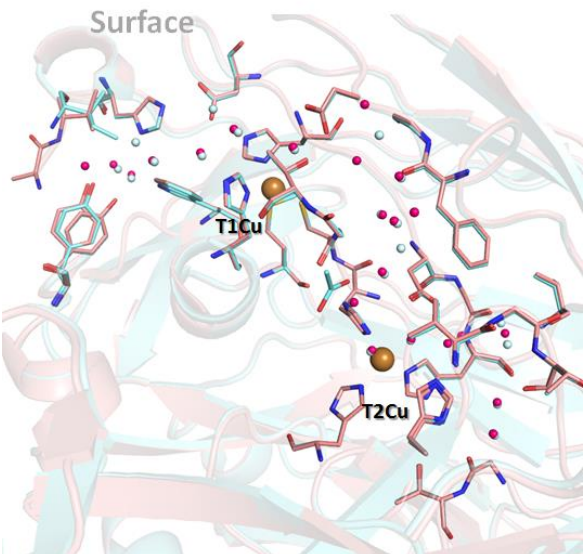

Figure 3-1. Superposition of WThot (sky blue) on WTcryo (pink). Cu atoms and water molecules are illustrated as blown and magenta (WT_{hot}) or pale cyan (WT_{cryo}) spheres.

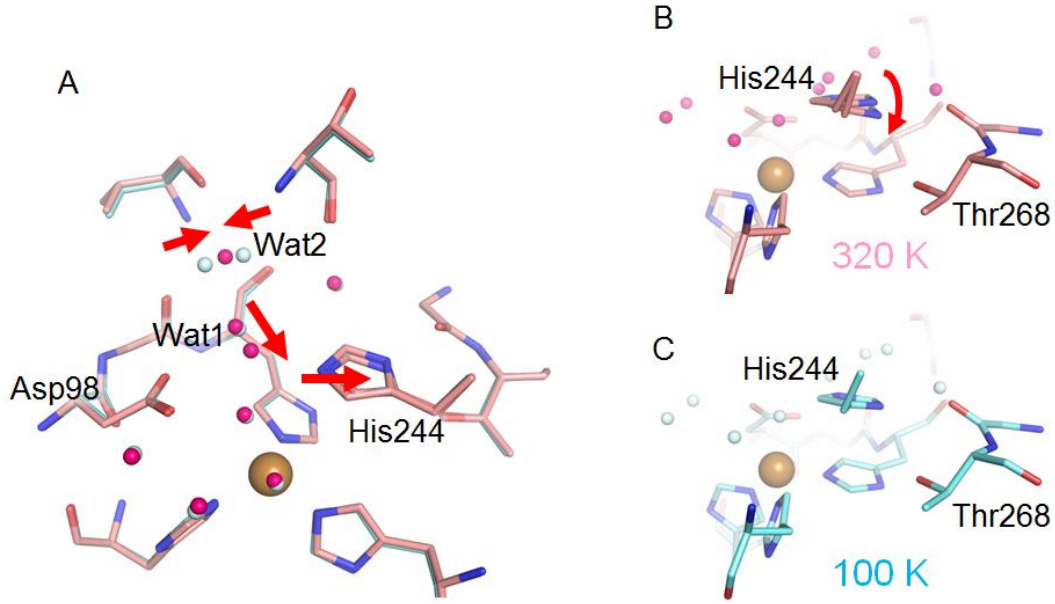

Figure 3-2. Comparison of WT_{hot} (sky blue) with WT_{cryo} (pink). (A) Superposition of the T2Cu site. Movements of molecules are indicated by red arrows. (B) The T2Cu site of WThot. (C) The T2Cu site of WTcryo.Cu atoms and water molecules are illustrated as blown and magenta (WT_{hot}) or pale cyan (WT_{cryo}) spheres.

3.3.2. High-temperature structure of the C135A-nitrite complex

The structure of C135A-NO2$_{hot}$ was determined at 1.55 Å resolution (R_{work} and R_{free} was 12.5 and 14.7%, respectively). The refined model containing a mixture of 50% occupancy nitrite and 50% occupancy water bound to the T2Cu atom produced a good fit to the experimental data. All three atoms of nitrite were located near enough to interact with the T2Cu atom. The distances of Cu-O1, Cu-O2, and Cu-N were 2.64, 2.04, and 2.27 Å, respectively. Nitrite did not adopt complete η^2-O,O mode, which is observed in other CuNIRs, because the O1 atom of nitrite formed a hydrogen bond with Wat6 specifically observed in *Geo*NIR and hence were attracted toward Wat6 (The H-bond distance was 2.44 Å). However, when the binding mode of nitrite in C135A-NO2$_{hot}$ is compared with that in C135A-NO2$_{cryo}$, the difference is obvious. As was observed in WT$_{hot}$, the imidazole ring of His244 showed two conformations. The C$^{\delta}$ atom of His244 0.45 Å moved away from the catalytic center. Moreover, the Oδ2 atom of Asp98 0.46 Å moved away from the catalytic center. These structural changes made the catalytic site wider than in the cryogenic structure.

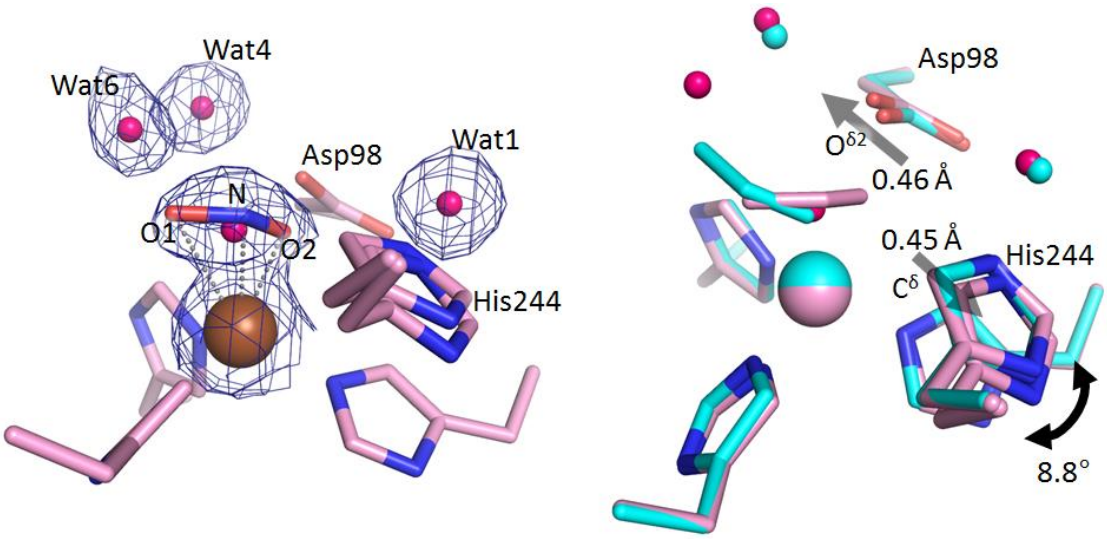

Figure 3-2. (A) The T2Cu site of C135A-NO2$_{hot}$. Cu atoms and water molecules are illustrated as blown and magenta. (C) Superposition of C135A-NO2$_{hot}$ on C135A-NO2$_{cryo}$ (pink)

3.4. Discussion

The pioneering and exclusive work about high-temperature protein X-ray crystallography was carried out by Petsko *et al*, in which the crystal structures were determined for ribonuclease-A at nine different temperatures ranging from 98 to 320 K (10). It reported that an overall expansion of the unit cell with increasing temperature was observed and the increase was linear for the *a*, *b*, and *c* axes, which corresponds to the observation of the increase in cell lengths of *Gt*NIR. Petsko *et al.* also demonstrated the increase in the *B*-factors with increasing temperature. These facts indicate that data collection of WT_{hot} and $C135A\text{-}NO2_{hot}$ were certainly carried out under high temperature. Moreover, low R_{merge} values of WT_{hot} and $C135A\text{-}NO2_{hot}$ data meant that data collection was completed before crystals suffered severe radiation damage.

Water plays important roles in structural stabilization and chemical reactions of proteins(11, 12). Especially, water molecules tightly bound to the protein surface are called structural water and are essential to expression of protein functions. At high temperatures, number of water molecules decrease (10). Thus, water which is found even in high-temperature structures must be expressly important. Water molecules lined up from the molecular surface to the catalytic site on one side of the substrate pocket even at high temperature (Figure 3-1). However, there was no electron density of solvent molecules on the other side of the substrate pocket. This observation indicates that the former side is the proton channel (channel A) as was discussed in chapter 2 and that the latter side is the substrate channel through which nitrite and nitric oxide pass. The conformation of Val249 at high temperature was the same as that in the cryogenic structure and blocked up the proton channel B, which support the belief described in chapter 2 that the channel B is not the main proton channel.

Under high-temperature circumstances, nitrite bound to the T2Cu atom in the near-side-on manner (Figure 3-3A, 3-3B). This is probably because the space above the T2Cu site can be widened in consequence of conformational changes of Asp98 and His244. These residues are fixed by steric hindrance and the unusual CH-O hydrogen bond. However, thermal energy may enable them to move slightly. Because the data was collected at 320 K, which is a little lower than the optimum temperature for *Geobacillus* (60 ℃) (13), it is possible that the *Geo*NIR structure undergo more dynamic structural changes at higher temperatures and nitrite adopt a complete η_2-O,O binding mode.

High-temperature and high-resolution X-ray crystallography unraveled the binding mode of nitrite was different from temperature to temperature. This is the first case which demonstrated that a cryogenic structure of a thermostable enzyme does not always reflect the authentic structure under the physiological environment. Proteins from thermophilic organisms have been used to investigate structure-function relationships of proteins instead of more unstable homologue proteins, because it is easy to express, purify and crystallize them. However, now that it is obvious that some cryogenic structures of thermostable proteins differ from their natural structures at high temperatures. Thus, high-temperature and high-resolution X-ray crystallography should be applied to studies on thermostable proteins other than *Geo*NIR and will open up a new horizon for structural biology.

References

1. Henderson, R. (1990). Cryo-Protection of Protein Crystals against Radiation Damage in Electron and X-Ray Diffraction *Proceedings of the Royal Sosciety B* **241**, 6-8.
2. Garman, E. (2003). 'Cool' crystals: macromolecular cryocrystallography and

radiation damage. *Current Opinion in Structural Biology* **13**, 545-551.

3. Fraser, J. S., Clarkson, M. W., Degnan, S. C., Erion, R., Kern, D. & Alber, T. (2009). Hidden alternative structures of proline isomerase essential for catalysis. *Nature* **462**, 669-73.
4. Weik, M. & Colletier, J. P. (2010). Temperature-dependent macromolecular X-ray crystallography. *Acta Crystallogr D Biol Crystallogr* **66**, 437-46.
5. Fraser, J. S., Bedem, H. v. d., Samelson, A. J., Lang, P. T., Holton, J. M., Echols, N. & Alber, T. (2011). Accessing protein conformational ensembles using room-temperature X-ray crystallography. *Proc Natl Acad Sci U S A* **108**, 16247-16252.
6. Chill, J. H. & Naider, F. (2011). A solution NMR view of protein dynamics in the biological membrane. *Curr Opin Struct Biol* **21**, 627-33.
7. Hong, M., Zhang, Y. & Hu, F. (2012). Membrane protein structure and dynamics from NMR spectroscopy. *Annu Rev Phys Chem* **63**, 1-24.
8. Wuthrich, K. (2003). NMR studies of structure and function of biological macromolecules (Nobel lecture). *Angew Chem Int Ed Engl* **42**, 3340-63.
9. Karplus, M. & Kuriyan, J. (2005). Molecular dynamics and protein function. *Proc Natl Acad Sci U S A* **102**, 6679-85.
10. Robert F. Tilton, J., Dewan, J. C. & Petsko, G. A. (1992). Effects of Temperature on Protein Structure and Dynamics: X-ray Crystallographic Studies of the Protein Ribonuclease-A at Nine Different Temperatures from 98 to 320 IC. *Biochemistry* **31**, 2469-2481.
11. Israelachvili, J. & Wennerström, H. (1996). Role of hydration and water structure in biological and colloidal interactions. *Nature* **379**, 219-225.
12. Levy, Y. & Onuchic, J. N. (2006). Water Mediation in Protein Folding and Molecular Recognition. *Annu. Rev. Biophys. Biomol. Struct.* **35**, 389-415.
13. Feng, L., Wang, W., Cheng, J., Ren, Y., Zhao, G., Gao, C., Tang, Y., Liu, X., Han, W., Peng, X., Liu, R. & Wang, L. (2007). Genome and proteome of long-chain alkane degrading Geobacillus thermodenitrificans NG80-2 isolated from a deep-subsurface oil reservoir. *Proc Natl Acad Sci U S A* **104**, 5602-7.

Chapter 4
Do copper-containing nitrite reductases dream of peptidylglycine α-hydroxylating monooxygenase?

Summary

Copper-containing nitrite reductase (CuNIR) catalyzes the one-electron reduction of nitrite to nitric oxide, and is also believed to reduce oxygen to hydrogen peroxide using two electrons. Here, we provide microspectroscopic evidence that dioxygen binds to the catalytic copper (T2Cu) site of CuNIR, and reveal the first structural basis for the oxygen reduction in CuNIR by determining the 1.20 and 1.50 Å resolution structures of CuNIR displaying side-on dioxygen bound to T2Cu with O-O distances of 1.21 and 1.26 Å, respectively. Moreover, to compare T2Cu of CuNIR with the catalytic Cu_M site of peptidylglycine α-hydroxylating monooxygenase (PHM), at which activated dioxygen abstracts a hydrogen atom from the substrate's carbon atom, we constructed the mutant CuNIR (H294M), in which one of the three histidyl ligands of T2Cu is substituted with methionine in imitation of Cu_M in PHM. The 1.35 Å resolution structure and EPR parameters of H294M suggest that modified T2Cu shared striking similarities with Cu_M in terms of geometry and electronic state, which indicates that methionine is essential to activation of oxygen at the Cu_M site.

4.1. Introduction

Copper is one of the most ubiquitous transition metal elements in living systems. It has

been adopted by all three biological domains, archaea, bacteria, and eukaryote, in the form of copper-containing proteins that take part in various essential processes such as electron transfer and redox reactions of a variety of substrates (1-3). Many mononuclear copper sites in protein structures are generally classified into two groups: type 1 Cu (T1Cu) and type 2 Cu (T2Cu) site (4). The T1Cu site is often found ligated by one cysteinyl, one methionyl, and two histidyl residues, and is responsible for electron-transfer (ET) reactions. In addition, oxidized T1Cu sites display a strong absorption band at about 600 nm because of ligand-to-metal charge transfer (LMCT) from the thiolate sulphur atom of the cysteine ligand to the copper atom (5). The T2Cu site is three to four coordinate, and one or more of the ligands of the copper center are imidazole side chains of histidyl residues. Despite the notable differences of properties among the substrates, diverse reactions can occur at the similar, if not completely identical, T2 Cu sites. For instance, when molecular oxygen is the substrate, the T2Cu centers act as the catalytic sites of oxidases, as is seen in monooxygenase or dioxygenase. Moreover, the T2Cu centers can perform the dismutation of superoxide and reduce nitrite (NO_2^-) to nitric oxide (NO). However, it has long been unclear how the similar T2Cu sites can assume such a wide variety of reactions (6).

Copper-containing nitrite reductase (CuNIR), one of the most extensively investigated copper enzymes, literally catalyses the one-electron reduction of NO_2^- to NO with the expense of two protons ($NO_2^- + 2H^+ + e^- \rightarrow NO + H_2O$) in the denitrification process. CuNIR function as a homotrimer with each monomeric unit containing one T1Cu and one T2Cu site. The T1Cu site gets an electron from a physiological electron donor, and the electron is subsequently consumed by the reduction reaction at the T2Cu site that is coordinated by three histidyl residues, His100, His134, and His294, the last residue of

which comes from the adjacent monomer [the numbers of residues refer to the *Geobacillus thermodenitrificans* CuNIR (*Gt*NIR) sequence] (7). The electrons can be efficiently transferred from T1Cu to T2Cu because two copper sites are connected through adjacent residues, Cys135 and His134, which are the ligands of T1Cu and T2Cu, respectively. Additionally, CuNIR has been known to have the activity of the two-electron reduction of dioxygen to hydrogen peroxide that causes inactivation of CuNIR's original function (8, 9). However, the detailed mechanism of this phenomenon has been unknown because Cu-O_2 complexes decomposes so readily that visualization and observation of them have been difficult.

While a dioxygen molecule functions as an inhibitor in CuNIR, it plays another role in a small class of copper-containing monooxygenases such as peptidylglycine α-hydroxylating monooxygenase (PHM) and dopamine ß-monooxygenase (DßM). These mononuclear-copper oxygenases catalyze the activation of dioxigen to abstract a hydrogen atom on a carbon atom of a substrate to yield imperative chemicals associated with neurotransmission and behavioral development (10). These monooxygenases contain two non-coupled T2Cu sites, namely, the Cu_H and Cu_M site. The Cu_H site is composed of three histidyl residues and is thought to be the electron-acceptor center. The Cu_M site, the catalytic site, is ~11 Å away from the Cu_H site without direct connection such as peptide bond; thus, two copper sites have no electronic coupling. The structure of the Cu_M site is slightly different from the T2Cu site in CuNIR. It is coordinated by two histidyl residues and one methionyl residue and one water molecule in a resting state (11). Although all members of the monooxygenase family of PHM and DßM have a methionine ligand at the Cu_M site, the function of it unfortunately remains controversial and one of the main topics of studies (12-14). In the crystal structure of

PHM equipped with a substrate and a dioxygen species, dioxigen was found to bind to the Cu_M site in an end-on manner (15). However, both oxygen atoms were too distant from the C^{α} atom in the substrate to abstract the hydrogen atom. Therefore, the oxygen molecule is thought to change its direction on the Cu_M site. Theoretical chemistry predicted that a superoxo-Cu(II) complex is one of the intermediate of the reaction and it can adopt the side-on binding mode as well as the end-on manner (16). Although the side-on superoxide bound to the mononuclear copper center has not yet been observed in protein crystal structures, the recently-reported structure of PHM with hydrogen peroxide shows its side-on binding mode (17). Despite intensive efforts, the detailed mechanisms of PHM and DβM have been ambiguous (18).

Here, the author is focusing on *Gt*NIR because it has the widest substrate pocket in known CuNIRs (as described in Chapter 2). The structural feature implies that the T2Cu site of *Gt*NIR is more prone to be bound by oxygen molecules than other CuNIRs, and allows us to easily observe interaction of T2Cu with oxygen species. By combining crystallographic and microspectroscopic techniques, we demonstrate that an oxygen species can bind to the T2Cu site of *Gt*NIR in the side-on manner. Based on the high-resolution structures, we also postulate the feasible mechanism of the oxygen reduction in CuNIR. Moreover, to compare the T2Cu site of CuNIR with the Cu_M site of copper-containing monooxygeneases like PHM and to elucidate the function of methionine in the Cu_M site, we analyzed the H294M mutant of *Gt*NIR using an electron paramagnetism resonance (EPR) method and determined its crystal structure. Our present studies will lead to a comprehensive understanding upon the functions of various T2Cu-containing enzymes as well as that of CuNIR itself.

4.2. Methods

4.2.1. Expression and purification of WT *Gt*NIR and the H294M mutant

Preparation of WT *Gt*NIR was performed using previously described protocols in Chapter 2. The forward and reverse primers for the H294M mutant were 5'-TCCGATCGTTACTATGCAGTTTAATCATGC-3' and 5'-GCATGATTAAACTGCATAGTAACGATCGGA-3', respectively. The sequences of mutant plasmids were confirmed by DNA sequencing before transformation into *E. coli* strain BL21 (DE3) *E. coli*. The mutant was overexpressed and purified following the wild-type protein protocol.

4.2.2. Microspectroscopy

The UV-vis spectra of the WT crystal was measured using a microspectrophotometer connected with an X-ray diffractometer installed at beamline BL38B1 at SPring-8 (Hyogo, Japan). All UV-vis microspectrum data for crystals were measured in a 100 K cryostream and were collected four times to increase signal to noise ratios. UV-vis absorption differences due to different crystal thicknesses were avoided by fixing the direction of the crystals for each measurement.

4.2.3. EPR Spectroscopy

X-band EPR spectra in 40 mM HEPES buffer (pH 7.0) were recorded at 77 K using a JEOL X-band spectrometer (JES-RE1XE). Experimental conditions were the following: microwave frequency, 9.0 GHz ; microwave power, 1.0 mW; field modulation amplitude,

10 G; modulation frequency, 100 kHz. The *g* values were calibrated using an Mn^{2+} marker.

4.2.4. Crystallization, X-ray diffraction data collection, phasing, and refinement

Crystallization of WT and H294M was performed using the previously published crystallization condition (submit). Data sets of WT-OXY1, H294M1 and H294M2 were collected from single crystals at 100 K on beamline BL38B1 at SPring-8 using an ADSC Quantum 315 CCD detector (Area Detector Systems Co., California, USA). Data sets of WT-OXY2 were collected from a single crystal at 100 K on beamline BL1A at Photon Factory (Tsukuba, Ibaraki, Japan) using a Pilatus 2M-F detector (DECTRIS Ltd., Baden, Switzerland). The HKL-2000 package (19) was used to reduce, integrate and scale the collected data. The crystal structure was determined by molecular replacement using the program MOLREP (20) from the CCP4 suite (21). A monomeric subunit of *Gt*NIR determined in our previous study was used as the search model. The resulting *Gt*NIR models were subject to a cycle of positional and individual *B*-factor refinement in REFMAC5 (22). Manual model building was carried out using COOT (23) thorough the refinement process. Water molecules were added to the model using the automated water-searching program built into COOT, and during the refinement of all structures, anisotropic refinement parameters were introduced. The bond distances between the O1 and O2 atoms of oxygen were unrestrained. The final models were checked for stereochemical quality using PROCHECK (24) and MolProbity (25). Data-collection and refinement statistics are summarized in Table IV-I.

Table IV-I. Data collection and refinement statistics

	WT-OXY1	WT-OXY2	H294M1	H294M2
Data collection				
Wavelength (Å)	0.75	0.96	0.90	0.90
Space group	*R*3	*R*3	*R*3	*R*3
Unit cell				
$a = b$, c (Å)	115.0, 84.5	114.9, 84.0	115.0, 84.1	114.9, 84.0
$\alpha = \beta$, γ (°)	90, 120	90, 120	90, 120	90, 120
Resolution range (Å)	50.0-1.50 (1.55-1.15)[a]	100.0-1.20 (1.22-1.20)	50.0-1.35 (1.38-1.35)	50.0-1.55 (1.58-1.55)
R_{merge} (%)[b]	10.3 (31.0)	7.5 (26.3)	10.3 (31.0)	10.9 (28.1)
Completeness (%)	97.0 (99.7)	92.1 (96.8)	97.0 (99.7)	99.5 (100)
Unique reflections	64,781 (6639)	120,357 (6323)	64,781 (6639)	60,917 (3087)
$\langle I/\sigma(I)\rangle$	14.3 (2.9)	16.6 (3.0)	14.3 (2.9)	22.0 (7.3)
Redundancy	2.9 (2.8)	3.5 (3.3)	2.9 (2.8)	3.7 (3.7)
Refinement				
Resolution range (Å)	42.9-1.50	28.7-1.20	18.4-1.35	25.35-1.55
R_{work} (%)[c]/ R_{free} (%)[d]	10.8/14.9	12.0/14.6	10.9/13.2	13.0/15.0
RMSD bond length (Å)	0.026	0.031	0.024	0.032
RMSD bond angle (°)	2.198	2.439	2.398	2.804

[a] Values in parentheses are for the highest-resolution shell.. [b] R_{merge} is calculated as $\Sigma_{hkl}\Sigma_i | I_i(hkl)-\langle I(hkl)\rangle | / \Sigma_{hkl}\Sigma_i I(hkl)$, where $I_i(hkl)$ is the intensity of an individual measurement of the reflection with Miller indices *hkl* and $\langle I(hkl)\rangle$ is the average intensity from multiple observations. [c] $R_{work} = \Sigma_{hkl} | | F_{obs} | - | F_{calc} | | / \Sigma_{hkl} | F_{obs} |$, where F_{obs} and F_{calc} are the observed and calculated structure-factor amplitudes, respectively. [d] The free *R* factor, R_{free}, is computed in the same manner as R_{work} but using only a small set (5%) of randomly chosen intensities that were not used in the refinement of the model.

4.3. Results

4.3.1. Microspectroscopic analysis

The UV-vis spectrum of the WT crystal before X-ray irradiation (red line in Figure 4-1A) shows absorption bands with peaks at around 450 and 600 nm, which correspond to peaks observed in the UV-vis spectrum of *Geobacillus* CuNIR recorded in solution (26). These bands are derived from ligand-to-metal charge transfer (LMCT) transitions from the sulpher atom of ligand Cys135 to the oxidized T1Cu (Cu^{2+}) center. Moreover, the weak absorbance originating from a d-d transition of Cu was observed between 650 and 750 nm, and a shoulder appeared between 300 and 400 nm (Figure 4-1A).

As the dose of X-ray to which the WT crystal was exposed increased, the intensities of

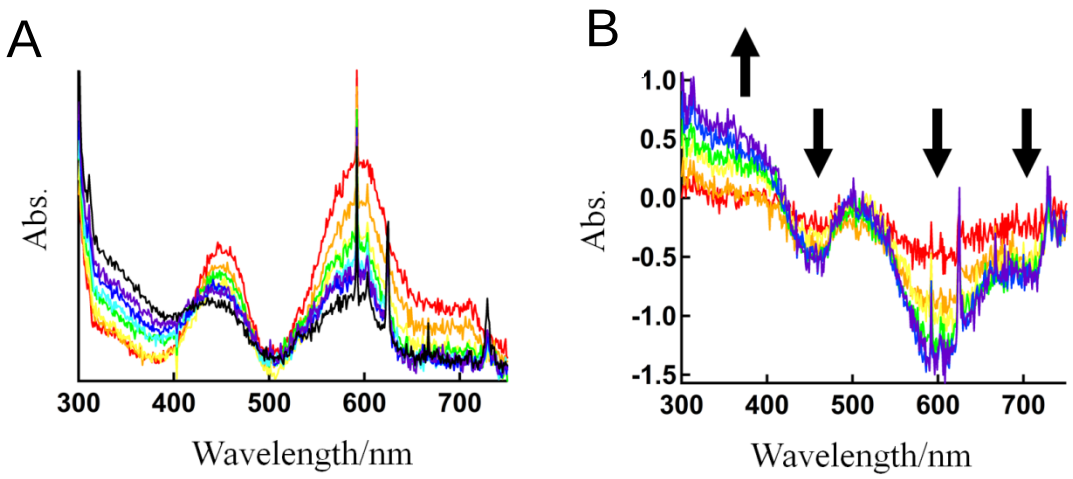

Figure 4-1. (A) Microspectroscopic ultraviolet-visible spectra of *Gt*NIR crystals. (A) X-ray-induced reduction of a crystal of *Gt*NIR using 0.75-Å radiation. The red line shows the spectrum before X-ray irradiation. The spectra from orange to purple were recorded every 45 s. The black line illustrates the spectrum recorded after a 9-min exposure. The absorption peaks at 455 and 600 nm are attributed to the T1Cu center. (B) The difference spectra of the *Gt*NIR crystal. The significant changes in intensity of spectra are shown by black arrows.

absorption at around 450 and 600 nm became weaker (Figure 4-1A, 4-1B). The band of the d-d transition also decreased. Conversely, the band between 300 and 400 nm

increased during exposure of the crystal to X-ray. These changes occurred sequentially. In other words, the decreases of absorption derived from oxidized copper sites (at 450, 600, and ~700 nm) were first recorded and then the increase of absorption between 300 and 400 nm became conspicuous. The rate of decrease in absorption at 450 and 600 nm gradually became slower, and the bands never disappeared even after excess X-ray irradiation (black line in Figure 4-1A).

4.3.2. The X-ray crystal structures of WT and H294M

The X-ray diffraction data sets were collected from the same crystal of WT as that used in the microspectroscopic analysis, and its crystal structure (WT-OXY1) was determined at 1.50 Å resolution. The higher resolution structure (WT-OXY2) was determined at 1.20 Å resolution using the crystal which grew under the same crystallization condition. In both electron density maps of WT-OXY1 and WT-OXY2, a clear ellipsoidal form of electron density was observed above the T2Cu site, which could best be modeled as a diatomic molecule (Figure 4-2A). In both cases, they were modeled as dioxygen molecules coordinated to the T2Cu centers with 80 % occupancy (Figure 4-2A, 4-2B). The binding mode of dioxygen observed in *Gt*NIR was more side-on than end-on because the distances between the oxygen atoms and the copper atom were 2.35 and 1.96 Å (WT-OXY1) or 2.40 and 2.13 Å (WT-OXY2), respectively. In both WT-OXY1 and WT-OXY2 structures, the water molecules (Wat0) with 20 % occupancy were located next to the oxygen molecule. In the WT-OXY2 structure, another water molecule (Wat0') with 20 % occupancy existed at the same position as the O1 atom (the farther atom from the T2Cu center) of the oxygen molecule. The distances between oxygen atoms, which were not restrained in the refinement processes, were 1.26 and 1.25 Å in the WT-OXY1

and WT-OXY2 structure, respectively.

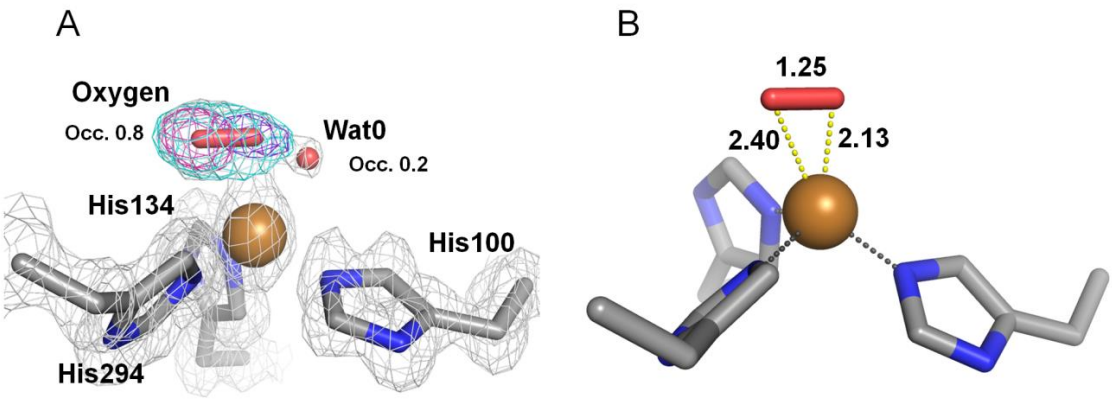

Figure 4-2. (A) Side-on oxygen species on the T2Cu site observed in the *Gt*NIR structure determined at 1.20 Å resolution (WT-OXY2). The $2F_o$-F_c map (contoured at 1.5 σ) is represented by a gray mesh. Difference omit maps leaving out both oxygen atoms (cyan mesh) and either the distal oxygen (magenta mesh) or the proximal oxygen (purple mesh) are shown contoured at 8.0 σ. (B) Coordination geometry of the oxygen species in WT-OXY2. Distances from Cu atoms to coordinating protein atoms and oxygen atoms are expressed in angstroms and are shown as dotted black and yellow lines, respectively. The Cu ion is shown as a brown sphere. Carbon, oxygen, and nitrogen atoms are shown in gray, red and blue, respectively.

Two structures of the H294M mutant, H294M1 and H294M2, were determined at 1.35 and 1.55 Å resolution, respectively. The crystal structure of the T2Cu site of H294M1 is illustrated in Figure 4-3A. The point mutation of the ligand to the T2Cu center caused no significant perturbation of the overall structure (Cα RMSD to WT is 0.07 Å) and the geometry of the T1Cu site (Table IV-II). On the other hand, the T2Cu center showed obvious geometrical changes. In the WT structures, three histidyl residues were coordinated to the T2Cu atom with almost equal distances (~ 2.0 Å) whereas in H294M1, the sulphur atom of methionine was farther from the T2Cu atom (2.28 Å) than the two nitrogen atoms of His100 and His134 (2.00 and 2.05 Å, respectively). In addition, one water molecule (Wat0) was found axially coordinated to the T2Cu in the H294M

structure (2.19 Å). An acetate molecule was located near the T2Cu site to form hydrogen bonds with the Oδ2 atom of Asp98 and Wat0 in H294M1 (Figure 4-3A).

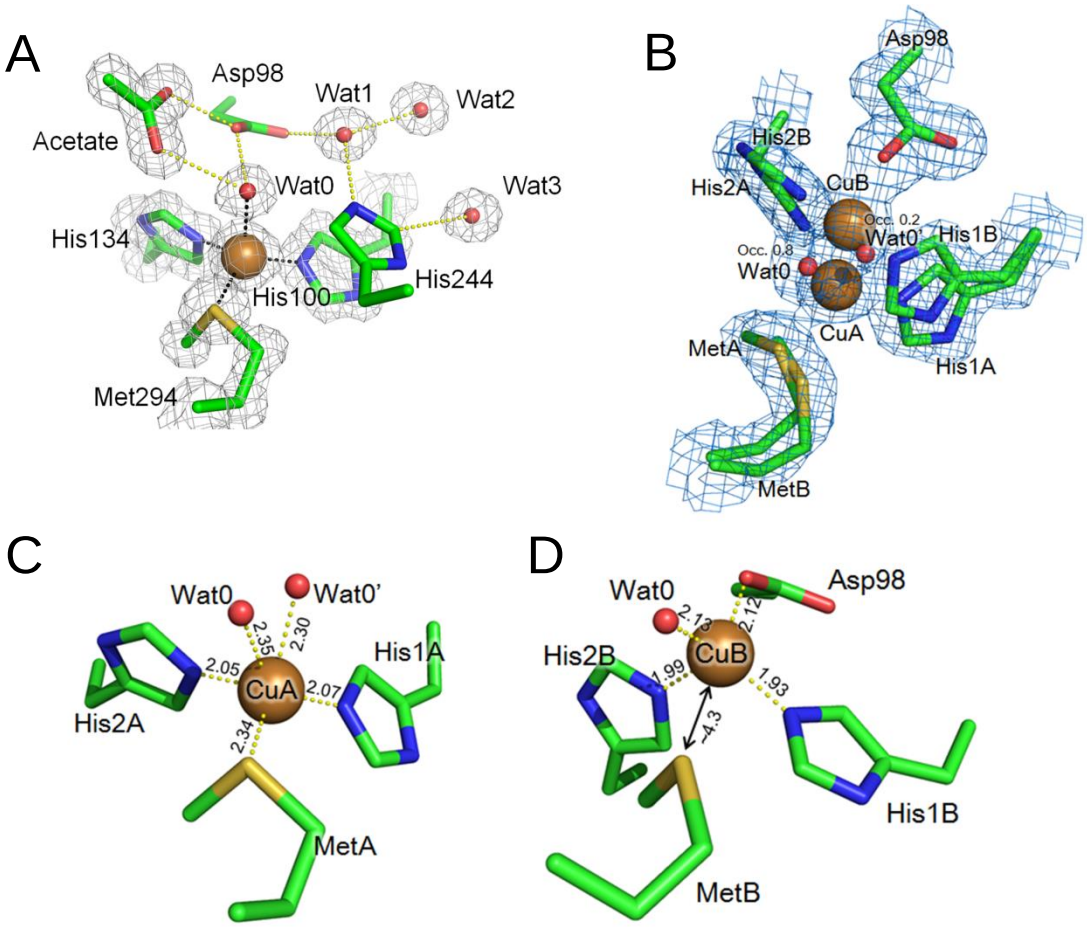

Figure 4-3. The T2Cu site of the structure of (A) H294M1 and (B) H294M2. The Cu ion and the water molecule are shown as brown and red spheres. The detailed structure of (C) the CuA and (D) CuB site of H294M2. Carbon, oxygen, nitrogen, and sulphur atoms are shown in green, red, blue, and yellow, respectively. Distances from Cu atoms to coordinating atoms are shown as dotted yellow lines. The $2F_o$-F_c maps (contoured at 1.5 σ) are represented by gray or blue meshes.

Although the crystal of H294M2 was grown in the same crystallization drop as the crystal of H294M1, the structure of the T2Cu site in H294M2 was different from that of H294M1. There were two positions of the copper atom, Cu1 and Cu2, as illustrated in Figure 4-3B. Each copper atom showed 50 % occupancy. The Cu1 atom was coordinated

by His100, His134 and Met294 as was observed in H294M1 (Figure 4-3C). On the other hand, Cu2 showed a novel coordination structure (Figure 4-3D); that is, it was coordinated by His100, His134, and Asp98, which acts as a catalytic residue in the nitrite reduction. Two water molecules, Wat0 and Wat0', were observed at the apical position of the T2Cu site in H294M2 with 80 and 20 % occupancy, respectively. Wat0 can bind to the Cu1 atom as well as the Cu2 atom. Wat0' can only bind to the Cu1 because the distance between the Cu2 atom and Wat0' was too short (1.56 Å). The geometries of the T2Cu sites are summarized in Table IV-II.

Table IV-II. Copper site geometries

Parameter	H294M1	H294M2	WT-OXY1	PHM (1PHM)
	I. Type 1 Cu-Ligand Distances (Å)			
T1Cu-H95N$^{\delta 1}$	1.97	2.01	2.04	n/a
T1Cu-C135S$^{\gamma}$	2.18	2.14	2.16	n/a
T1Cu-H143N$^{\delta 1}$	2.00	1.94	1.99	n/a
T1Cu-M148S$^{\delta}$	2.59	2.61	2.61	n/a
	II. Type 2 Cu-Ligand Distances (Å)			
T2Cu-H100N$^{\varepsilon 2}$	2.00	2.07/1.93[a]	1.97	1.91[b]
T2Cu-H134N$^{\varepsilon 2}$	2.06	2.05/1.99[a]	2.03	2.09[c]
Cu-H294N$^{\varepsilon 2}$ (M249S$^{\delta}$ /D98O$^{\delta 2}$)	2.28	2.34/2.12[a]	2.02	2.42[d]
T2Cu-Wat0 (Wat0')	2.19	2.35/2.13[a] (2.30)	2.23	2.28

[a] The right value is for CuA and the left for CuB.[b] The distances between Cu_M and His242N$^{\varepsilon 2}$, [c] The distances between Cu_M and His244N$^{\varepsilon 2}$, [d] The distances between Cu_M and Met314S$^{\delta}$.

4.3.3. EPR spectroscopy

The spectrum of WT showed clear hyperfine splitting signals originating from the T2Cu site and less clear signals of the T1Cu site because of overlapping with the T2Cu signals (Figure 4-4A). The EPR parameters of the T2Cu sites are summarized in Table IV-III.

The values of $A_{//}$ and $g_{//}$ of T2Cu in WT were similar to those measured for other typical

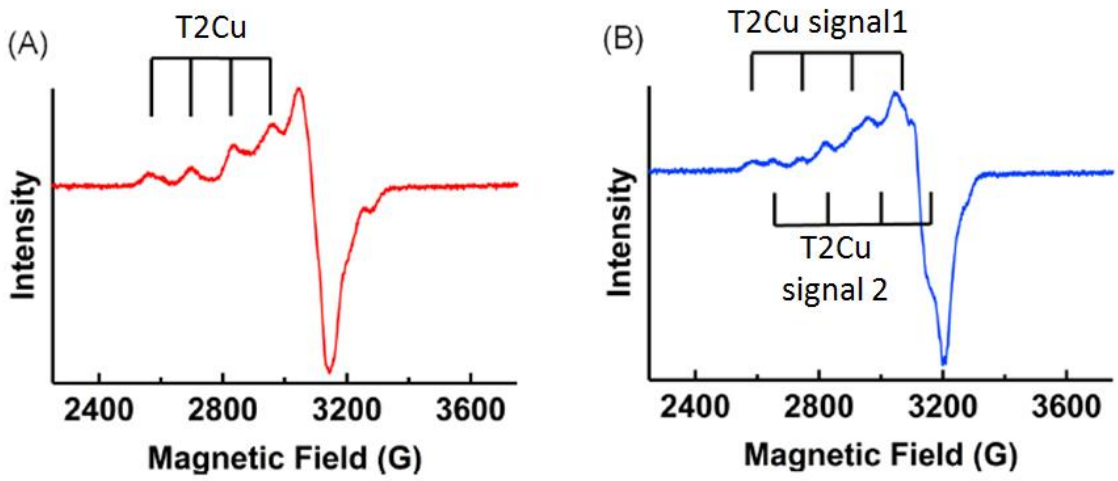

Figure 4-4. EPR spectra of *Gt*NIR in 40 m*M* HEPES buffer (pH 8.0) recorded at 77 K. (A) The EPR spectrum of WT. (B) The EPR spectrum of the H294M mutant.

CuNIRs (27). The shape of the EPR spectrum of H294M was significantly different from that of WT (Figure 4-4B). H294M showed two types of signals in the region where signals of the T2Cu site appear. The EPR parameters calculated from both types of signals of the T2Cu site in H294M were different from those of WT (Table IV-III). The T2Cu site in H294M showed larger $A_{//}$ and smaller $g_{//}$ values than those in WT do.

Table IV-III. EPR parameters of T2Cu or Cu_M

parameter	WT	H294M signal 1	H294M signal 2	*Ac*NIR/*Ax*NIR[a]	PHM
$A_{//}$ (mT)	13.3	16.8	15.5	13.0/12.8	16.7[b]/15.7[c]
$g_{//}$	2.33	2.28	2.24	2.33/2.32	2.25[b]/2.28[c]

[a] Reference 27. *Ac*NIR and *Ax*NIR are CuNIRs from *Acromobacter cycloclastes* and *Achromobacter xylosoxidans*, respectively. [b] Reference 28, [c] Reference 29.

4.4. Discussion

4.4.1. Side-on oxygen species was trapped on the T2Cu atom during X-ray irradiation and visualized by the crystallographic method.

The UV-vis spectrum of the crystal of WT *Gt*NIR showed absorption bands with peaks at around 450 and 600 nm before X-ray irradiation (red line in Figure 4-1A), which corresponds to the reported ultraviolet-visible spectrum of Geobacillus CuNIR recorded in solution (6). These bands are derived from ligand-to-metal charge transfer (LMCT) transitions from the S atom of the ligand Cys135 to the T1Cu atom in the oxidized form. Moreover, the weak absorbance originating from a d-d transition in Cu^{2+} was observed at around 700 nm. The intensities of these bands decreased during X-ray irradiation (Figure 4-1A, 4-1B), which demonstrated that the T1Cu site changed from a greenish-blue oxidized state to a colorless reduced state during the experiment (7). However, the rate of the decreases in band intensities gradually became slow, and T1Cu was never completely reduced even after excess X-ray irradiation (black line in Figure 4-1A). One explanation may be because electrons flowed from the T1Cu to the T2Cu site and hence the T1Cu atom was re-oxidized. Another spectral change noticed during the course of the experiment was that the absorption band between 300 and 400 nm became more obvious. Although the cryo-solution containing 2-metyl-2,4-pentanediol (MPD) is known to show the increase in absorption between 240 and 350 nm when the exposure time of X-ray is long (8), there was no spectral change in the absorption spectrum of the cryo-solution only after X-ray irradiation under the same conditions. These facts implied that an unknown ligand bound to the T2Cu atom and it caused a LMCT transition. It is speculated that it was a side-on oxygen species because CuNIR is known to interact with oxygen species and a side-on superoxo-Cu(II) complex has an absorption

band at 352 nm, which was previously assigned to the LMCT transition from superoxide to the copper atom (9). Many other copper(II)-O_2 complexes also show absorption bands between 300 and 400 nm (10,11).

WT *Gt*NIR crystal structures (WT-OXY1 and WT-OXY2) support the belief that it was a side-on oxygen species because the ellipsoidal electron density maps clearly exhibited the existence of a diatomic molecule above the T2Cu site, and excluded the possibility that it was assigned to two water molecules close to each other (Figure 4-2A). The diatomic molecule could not be N_2, CO, or NO because these were only present in trace amounts in the buffer used for the experimental processes. Thus, the electron densities were assigned to dioxygen molecules with 80% occupancy, the temperature factors of which were 21 and 18 $Å^2$ in WT-OXY1 and WT-OXY2, respectively. The dioxygen molecules in both WT-OXY1 and WT-OXY2 had O-O distances refined to values of 1.26 and 1.25 Å, respectively. These are compatible with typical O-O distances of neutral dioxygen or superoxide (1.2-1.3 Å) coordinating to a copper atom, but not with that of peroxide (1.4-1.5 Å) (12). NO is known to adopt a side-on binding mode in CuNIR (4,5); therefore, in a similar fashion, O_2 is likely to prefer the side-on binding mode in CuNIR. Although for more than 30 years oxygen molecules have been thought to be reduced by CuNIR to yield hydrogen peroxide, which inhibits the activity of CuNIR (2), there was no direct evidence that oxygen species interact with CuNIR. In this study, oxygen species bound to the T2Cu atom in CuNIR were visualized for the first time. Raman microspectroscopic analysis will provide further evidence that the external ligand which coordinated to the T2Cu site during the experiment is the dioxygen molecule.

Most T1Cu and T2Cu sites in the *Gt*NIR crystal were thought to exist in their oxidized forms before X-ray irradiation because LMCT and d-d transition absorption bands were

evident prior to the start of the experiment. This indicated that only a small number of oxygen molecules could coordinate to the T2Cu sites prior to the experiment because neutral oxygen molecules usually only bind to reduced copper (Cu^+) atoms. This view is supported by the small shoulder observed between 300 and 400 nm prior to X-ray irradiation (Figure 4-1A). The increase of absorption became evident only after the decrease of absorption derived from the oxidized copper sites (at 450, 600, and ~700 nm) occurred (red and orange lines in Figure 4-1A, 4-1B). This phenomenon corresponds to the expectation that the T2Cu sites have to be reduced first by the electrons relayed from the T1Cu sites so that the dioxygen molecules can bind to the T2Cu sites.

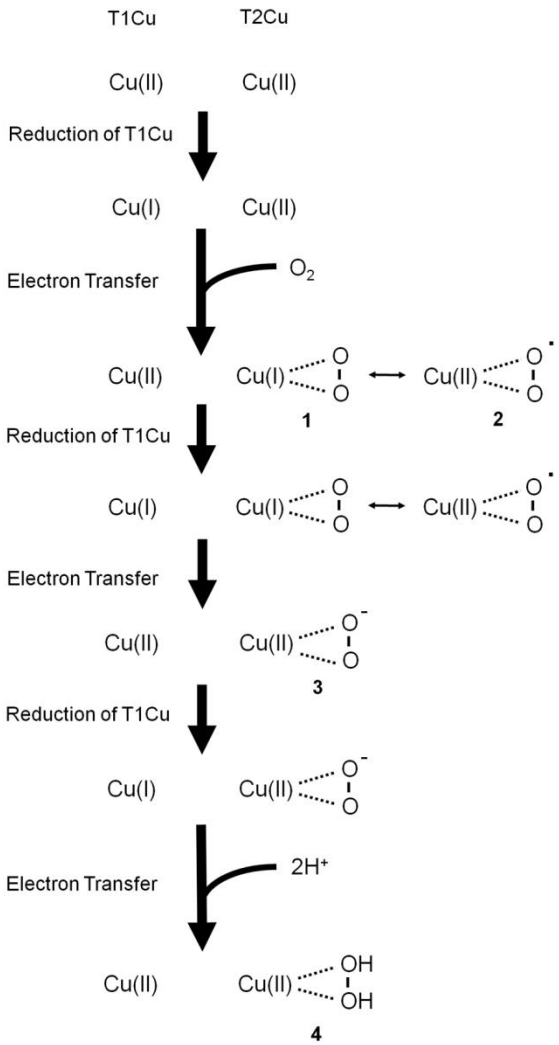

Scheme 4-1

Once an oxygen molecule binds to the T2Cu site, it can accept electrons and be reduced. The proposed reaction mechanism of intramolecular ET and the reduction of oxygen species in CuNIR are summarized in Scheme 4-1. The T2Cu site in CuNIR is known to be resistant to reduction by a hydrated electron generated by X-ray irradiation because it is far away from the molecular surface (7). Thus, the T1Cu site located near the molecular surface is always reduced first. The

oxygen species observed in the WT structures may be a mixture of **1** (neutral oxygen), **2**, and **3** (superoxide) (Scheme 4-1). If species **3** is further reduced, a peroxide anion will be produced. When CuNIR reduces NO_2^- ($NO_2^- + 2H^+ + e^- \rightarrow NO + H_2O$), two protons are provided by the side chains of nearby residues or water molecules around the T2Cu site (13). Thus, the peroxide anion could be similarly converted to hydrogen peroxide (H_2O_2, **4**) by gaining two protons.

Recently, an artificial T2Cu center coordinated by three histidyl residues was constructed in an α-helical coiled coil architecture and found to catalyze the reduction of nitrite (14). Our results indicate that such a copper site can act as a catalyst capable of reducing dioxygen to hydrogen peroxide. As a promising green oxidant, there is an increasing commercial demand for hydrogen peroxide (15). However, current synthetic processes are costly or harmful. Thus, more economical and safer methods for the production of hydrogen peroxide are required. Copper enzymes may be a good candidate for incorporating into a new synthetic method to produce hydrogen peroxide, and the results described herein provide a structural foundation for achieving such a new enzyme.

4.4.2. A comparison of the mutated T2Cu site in H294M with the Cu_M site in PHM.

The geometrical structure of the T2Cu site of the H294M mutant differs from that of the WT structure (Figure 4-3, Table IV-II). The distance between the sulphur atom of Met294 and the copper atom is significantly longer than the distances between the N^{ε} atoms of His100 and His134. Further, in contrast to the WT structure, the water

molecule exists as an axial ligand with a Cu-O distance of 2.19 Å. These structural characters, i.e. two close histidyl residues and one far methionyl residue and one far water ligand, is observed in the catalytic copper (Cu_M) site of PHM (Table IV-II) (11), which means that the geometry of the T2Cu site in the H294M mutant deviated from that of the T2Cu site in CuNIR toward that of the Cu_M site in PHM.

The difference between the EPR spectrum of WT and H294M was thought to come only from the change in the coordination geometry of the T2Cu site because the H294M structure confirmed that the T1Cu site was not perturbed by the point mutation. The two different signals of H294M may be due to the different states of the T2Cu site. This speculation is supported by the crystal structure of H294M2 displaying two different copper-center structures at the T2Cu site. Both EPR signals from T2Cu of H294M showed the larger $A_{//}$ value and the smaller $g_{//}$ value than the corresponding values of WT. The Cu_M site in PHM has been known to show a larger $A_{//}$ and smaller $g_{//}$ value than the T2Cu sites in CuNIRs do (Table IV-III) (28, 29). The replacement of His294 at the T2Cu site with methionine, thus, significantly altered not only the geometrical structure but also the electronic state of the T2Cu atom, and made the mutated T2Cu site in *Gt*NIR quite close to the Cu_M site in PHM. These geometric and electronic structures provided by methionine may be needed for the activation of oxygen molecules in PHM.

4.4.3. Can CuNIRs be utilized for a mold of a novel copper enzyme?

The methionyl ligand of the Cu_M site of PHM has been known to adopt two conformations, bound and unbound forms. The structure of H294M2 indicated that Met294 can assume two conformations, and they were bound and unbound forms. Thus,

again, the T2Cu site in H294M seems to behave similarly to the Cu_M site in PHM. However, in the mutated T2Cu site, Asp98 tends to bind to the T2Cu atom. Every CuNIR contains this aspartate above the T2Cu site because it is one of the essential residues to the nitrite reduction. We, therefore, concluded that although it is known that the nitrite reduction can occur at the N_2S site in a model complex of CuNIR (30), it cannot function as a stable catalytic site in the CuNIR architecture.

While the Cu_M site in PHM is located near the molecular surface, the T2Cu site of CuNIR is embedded in the protein architecture, and the substrate pocket of CuNIR is optimized to accommodate nitrite composed of three atoms. Therefore, it is probably difficult for H294M to activate a C-H bond of large substrates which are hydroxylated by PHM. As a matter of fact, our H294M mutant did not show a significant activity of oxidation of 2-aminophenol (data not shown), which is often used for the assay of PHM, probably because the catalytic site of *Gt*NIR cannot accommodate such a large compound. However, if the substrate pocket of H294M is further widened by genetic engineering, it is feasible to construct a new CuNIR that functions like PHM or other oxygenases. In fact, widening of the substrate pocket of CuNIR by site directed mutagenesis was accompanied with an accelerated rate of *o*-dianisidine oxidation with dioxygen (9). Additionally, when we make a functional Cu_M site in CuNIR, we have to eliminate Asp98 located above the T2Cu site because this residue can bind to a copper atom and may wreck the constructed Cu_M site.

As mentioned above, the artificial N_3 copper site constructed in the protein architecture is known to catalyze nitrite reduction (31, 32). The present results show that the substitution of histidine with methionine at the T2Cu site can dramatically alter the property of the copper center, and hence will provide new guidance for

achieving a novel copper enzyme.

References

1. Ridge, P. G., Zhang, Y. & Gladyshev, V. N. (2008). Comparative Genomic Analyses of Copper Transporters and Cuproproteomes Reveal Evolutionary Dynamics of Copper Utilization and Its Link to Oxygen. *PLoS ONE* **3**, e1378.
2. Andreini, C., Bertini, I., Cavallaro, G., Holliday, G. L. & Thornton, J. M. (2008). Metal ions in biological catalysis: from enzyme databases to general principles. *J Biol Inorg Chem* **13**, 1205-18.
3. Andreini, C., Banci, L., Bertini, I. & Rosato, A. (2008). Occurrence of Copper Proteins through the Three Domains of Life: A Bioinformatic Approach. *The Journal of Proteome Research* **7**, 209–216.
4. Solomon, E. I., Sundaram, U. M. & Machonkin, T. E. (1996). Multicopper Oxidases and Oxygenases. *Chemical Reviews* **96**, 2563–2605.
5. Solomon, E. I., Baldwin, M. J. & Lowery, M. D. (1992). Electronic Structures of Active Sites in Copper Proteins: Contributions to Reactivity. *Chem Rev* **92**, 521-542.
6. MacPherson, I. S. & Murphy, M. E. (2007). Type-2 copper-containing enzymes. *Cell Mol Life Sci* **64**, 2887-99.
7. Suzuki, S., Kataoka, K. & Yamaguchi, K. (2000). Metal Coordination and Mechanism of Multicopper Nitrite Reductase. *Acc. Chem. Res.* **33**, 728-735.
8. Kakutani, T., Beppu, T. & Arima, K. (1981). Regulation of Nitrite Reductase in the Denitrifying Bacterium Alcaligenes faecalis S-6. *Agric. Biol. Chem.* **45**, 23-28.
9. MacPherson, I. S., Rosell, F. I., Scofield, M., Mauk, A. G. & Murphy, M. E. (2010). Directed evolution of copper nitrite reductase to a chromogenic reductant. *Protein Eng Des Sel* **23**, 137-45.
10. Klinman, J. P. (2006). The copper-enzyme family of dopamine beta-monooxygenase and peptidylglycine alpha-hydroxylating monooxygenase: resolving the chemical pathway for substrate hydroxylation. *J Biol Chem* **281**, 3013-6.
11. Prigge, S. T., Kolhekar, A. S., Eipper, B. A., Mains, R. E. & Amzel, L. M. (1997). Amidation of Bioactive Peptides: The Structure of Peptidylglycine -Hydroxylating Monooxygenase. *Science* **278**, 1300-1305.
12. Bauman, A. T., Broers, B. A., Kline, C. D. & Blackburn, N. J. (2011). A copper-methionine interaction controls the pH-dependent activation of

peptidylglycine monooxygenase. *Biochemistry* **50**, 10819-28.

13. Hess, C. R., Klinman, J. P. & Blackburn, N. J. (2010). The copper centers of tyramine beta-monooxygenase and its catalytic-site methionine variants: an X-ray absorption study. *J Biol Inorg Chem* **15**, 1195-207.
14. Bauman, A. T., Jaron, S., Yukl, E. T., Burchfiel, J. R. & Blackburn, N. J. (2006). pH Dependence of Peptidylglycine Monooxygenase. Mechanistic Implications of Cu-Methionine Binding Dynamics. *Biochemistry* **45**, 11140-11150.
15. Prigge, S. T., Eipper, B. A., Mains, R. E. & Amzel, L. M. (2004). Dioxygen binds end-on to mononuclear copper in a precatalytic enzyme complex. *Science* **304**, 864-7.
16. Chen, P. & Solomon, E. I. (2004). O2 activation by binuclear Cu sites: noncoupled versus exchange coupled reaction mechanisms. *Proc Natl Acad Sci U S A* **101**, 13105-10.
17. Rudzka, K., Moreno, D. M., Eipper, B., Mains, R., Estrin, D. A. & Amzel, L. M. (2013). Coordination of peroxide to the Cu(M) center of peptidylglycine alpha-hydroxylating monooxygenase (PHM): structural and computational study. *J Biol Inorg Chem* **18**, 223-32.
18. Rolff, M. & Tuczek, F. (2008). How do copper enzymes hydroxylate aliphatic substrates? Recent insights from the chemistry of model systems. *Angew Chem Int Ed Engl* **47**, 2344-7.
19. Otwinowski, Z. & Minor, W. (1997). [20] Processing of X-ray diffraction data collected in oscillation mode. *Methods Enzymol.* **276**, 307-326.
20. Vagin, A. & Teplyakov, A. (2010). Molecular replacement with MOLREP. *Acta Crystallogr D Biol Crystallogr* **66**, 22-5.
21. Winn, M. D., Ballard, C. C., Cowtan, K. D., Dodson, E. J., Emsley, P., Evans, P. R., Keegan, R. M., Krissinel, E. B., Leslie, A. G., McCoy, A., McNicholas, S. J., Murshudov, G. N., Pannu, N. S., Potterton, E. A., Powell, H. R., Read, R. J., Vagin, A. & Wilson, K. S. (2011). Overview of the CCP4 suite and current developments. *Acta Crystallogr D Biol Crystallogr* **67**, 235-42.
22. Murshudov, G. N., Skubak, P., Lebedev, A. A., Pannu, N. S., Steiner, R. A., Nicholls, R. A., Winn, M. D., Long, F. & Vagin, A. A. (2011). REFMAC5 for the refinement of macromolecular crystal structures. *Acta Crystallogr D Biol Crystallogr* **67**, 355-67.
23. Emsley, P., Lohkamp, B., Scott, W. G. & Cowtan, K. (2010). Features and development of Coot. *Acta Crystallogr D Biol Crystallogr* **66**, 486-501.
24. Laskowski. R. A., MacArthur. M. W., Moss. D. S. and Thornton. J. M. (1993). PROCHECK - a program to check the stereochemical quality of protein structures. *J. App. Cryst.* **26**, 283-291.

25. Chen, V. B., Arendall, W. B., 3rd, Headd, J. J., Keedy, D. A., Immormino, R. M., Kapral, G. J., Murray, L. W., Richardson, J. S. & Richardson, D. C. (2010). MolProbity: all-atom structure validation for macromolecular crystallography. *Acta Crystallogr D Biol Crystallogr* **66**, 12-21.

26. Fukuda, Y., Tamada, T., Takami, H., Suzuki, S., Inoue, T. & Nojiri, M. (2011). Cloning, expression, purification, crystallization and preliminary X-ray crystallographic study of GK0767, the copper-containing nitrite reductase from Geobacillus kaustophilus. *Acta Crystallogr Sect F Struct Biol Cryst Commun* **67**, 692-5.

27. Suzuki, S., Kataoka, K., Yamaguchi, K., Inoue, T. & Kai, Y. (1999). Structure–function relationships of copper-containing nitrite reductases. *Coordination Chemistry Reviews* **190-192**, 245-265.

28. Eipper, B. A., Quon, A. S. W., Mains, R. E., Boswel, J. S. & Blackburn, N. J. (1995). The Catalytic Core of Peptidylglycine α-Hydroxylating Monooxygenase: Investigation by Site-Directed Mutagenesis, Cu X-ray Absorption Spectroscopy, and Electron Paramagnetic Resonance. *Biochemistry* **34**, 2857-2865.

29. Chen, P., Bell, J., Eipper, B. A. & Solomon, E. I. (2004). Oxygen Activation by the Noncoupled Binuclear Copper Site in Peptidylglycine α-Hydroxylating Monooxygenase. Spectroscopic Definition of the Resting Sites and the Putative CuIIM-OOH Intermediate. *Biochemistry* **43**, 5735-5747.

30. Maji, R. C., Barman, S. K., Roy, S., Chatterjee, S. K., Bowles, F. L., Olmstead, M. M. & Patra, A. K. (2013). Copper complexes relevant to the catalytic cycle of copper nitrite reductase: electrochemical detection of NO(g) evolution and flipping of NO2 binding mode upon Cu(II) --> Cu(I) reduction. *Inorg Chem* **52**, 11084-95.

31. Tegoni, M., Yu, F., Bersellini, M., Penner-Hahn, J. E. & Pecoraro, V. L. (2012). Designing a functional type 2 copper center that has nitrite reductase activity within α-helical coiled coils. *Proc Natl Acad Sci U S A* **109**, 21234-21239.

32. Yu, F., Penner-Hahn, J. E. & Pecoraro, V. L. (2013). De Novo-Designed Metallopeptides with Type 2 Copper Centers: Modulation of Reduction Potentials and Nitrite Reductase Activities. *J Am Chem Soc*.

Conclusion

In chapter 1, using X-ray crystallography, the first atomic-resolution crystal structure of CuNIR from thermophilic bacterium (*Geo*NIR) was determined and analyzed in detail. *Geo*NIR, showed several unique structures: the short tower loop, the extra loop, and the N-terminal structure. The part of the N-terminal structure forming an α-helix was located on the putative interaction surface between *Geo*NIR and its physiological electron donor, cytochrome c_{551}. Using the stopped-flow technique, it was unclosed that the N-terminal structure inhibits non-specific interaction of *Geo*NIR with a non-physiological electron-transfer protein, but it facilitates specific interaction of the physiological electron-transfer pair.

Chapter 2 described the cryogenic *Geo*NIR structure in complex with nitrite and it was compared with other CuNIR:nitrite complex structures. Nitrite adopted the η^1-O binding mode in *Geo*NIR, which has never been observed in other typical wild-type CuNIRs, because the catalytic site of *Geo*NIR is tight and compacted to prevent nitrite intruding deeply. However, as described in chapter 3, high-temperature and high-resolution X-ray crystallography demonstrated that nitrite can assume the binding mode similar to those observed other CuNIRs at high temperature. This is because the space above the T2Cu is widened at high temperature. Especially, two catalytic residues, Asp98 and His244, undergo conformational changes. Thus, in conclusion, the reaction mechanism of *Geo*NIR is thought to be the same as other CuNIRs'. Therefore, though *Geo*NIR apparently looks much different from other known CuNIRs, to borrow a famous phrase in Gertrude Stein's poem, CuNIR is a CuNIR is a CuNIR is a CuNIR. In this thesis, it was unraveled for the first time using X-ray

crystallography that the binding mode of a substrate is different from temperature to temperature. In the field of structural biology, proteins from thermophilic organisms have been used as model proteins instead of more unstable homologue proteins because it is easy to express, purify and crystallize them. However, the present result indicated that some cryogenic structures of thermostable proteins do not always reflect their natural structures in the physiological environment. Thus, this novel technique is applicable and should be applied to studies on other thermostable proteins.

In chapter 4, the crystal structure of CuNIR in complex with a dioxygen molecule, which has been unknown for a long time, was determined. The structure of the T2Cu site with coordinating dioxygen is useful to understand reaction mechanisms of other copper proteins, a substrate of which is dioxygen. Moreover, a methionyl residue was introduced in the T2Cu site of *Geo*NIR to mimic the Cu_M site of PHM. In other words, the Cu_M site was constructed in the thermostable protein architecture and the base for an artificial copper enzyme was obtained. Although the enzymes containing the Cu_M site such as PHM and DβM are generally difficult to treat and to study using X-ray crystallography, the constructed Cu_M site in CuNIR is easy to investigate at an atomic level. Therefore, this experimental system made through the study is applicable to understanding the reaction mechanism of PHM and DβM.

New structural insights into the copper-containing nitrite reductase were provided by the study here, through which the novel X-ray crystallographic method was invented. Moreover, CuNIR was found to be a good mold for an artificial copper enzyme. The present results will lead to deeply understanding the nitrogen cycle and supply a new foundation for creating a novel artificial copper enzyme.

List of publications

1. Cloning, expression, purification, crystallization and preliminary X-ray crystallographic study of GK0767, the copper-containing nitrite reductase from *Geobacillus kaustophilus*
Yohta Fukuda, Taro Tamada, Hideto Takami, Shinnichiro Suzuki, Tsuyoshi Inoue and Masaki Nojiri
Acta Crystallographica, 2011, **F67**, 640-733

2. Structural insights into the function of a thermostable copper-containing nitrite reductase
Yohta Fukuda, Ka Man Tse, Masami Lintuluoto, Yoshifumi Fukunishi, Eiichi Mizohata, Hiroyoshi Matsumura, Hideto Takami, Masaki Nojiri and Tsuyoshi Inoue
The Journal of Biochemistry, 2014, **155**, 123-135

3. Structural and functional characterization of the *Geobacillus* copper nitrite reductase: roles of the unique N-terminal region on the interprotein electron transfer with its redox partner
Yohta Fukuda, Hiroyasu Koteishi, Ryohei Yoneda, Taro Tamada, Hideto Takami, Tsuyoshi Inoue and Masaki Nojiri
Biochimica et Biophysica Acta Bioenergetics, 2014, **1837**, 396-405

4. Crystallographic evidence for side-on dioxygen trapped on type 2 copper in a copper-containing nitrite reductase
Yohta Fukuda, Ka Man Tse, Yuji Kado, Eiichi Mizohata, Hiroyoshi Matsumura and Tsuyoshi Inoue
The Journal of Biochemistry (*submitted*)

5. Construction of the Cu_M site of peptidylglycine α-hydroxylating monooxygenase in a copper-containing nitrite reductase
Yohta Fukuda, Kei Ohkubo, Ka Man Tse, Yuji Kado, Eiichi Mizohata, Hiroyoshi Matsumura, Shunichi Fukuzumi and Tsuyoshi Inoue
in preparation

List of supplementary publications

1. Structural and mechanistic insights into the electron flow through protein for cytochrome *c*-tethering copper nitrite reductase
Aiko Tsuda, Ryosuke Ishikawa, Hiroyasu Koteishi, Kosuke Tange, **Yohta Fukuda**, Kazuo Kobayashi, Tsuyoshi Inoue and Masaki Nojiri
The Journal of Biochemistry, 2013, **154**, 51-60

2. Archaeal N,N′-diacetylchitobiose deacetylase: Expression from an engineered *Escherichia coli* chromosome and crystallographic study
Shouhei Mine, Mayumi Niiyama, Wakana Hashimoto, Takahisa Ikegami, Daisuke Koma, Takashi Ohmoto, **Yohta Fukuda**, Tsuyoshi Inoue, Yoshito Abe, Tadashi Ueda, Junji Morita, Koichi Uegaki, and Tsutomu Nakamura
The Journal of Biological Chemistry (submitted)

Acknowledgements

The study presented in this thesis has been carried out from April 2011 to March 2014 at Department of Applied Chemistry, Graduate School of Engineering, Osaka University, under the direction of Professor Tsuyoshi Inoue. This study could not have been possible without the help and involvement of many people.

In particular, the author would like to express his sincerest gratitude to Professor Tsuyoshi Inoue for his appropriate guidance, valuable discussions, and warm encouragement through this thesis. The author would like to express his deep gratitude to Dr. Hiroyoshi Matsumura and Dr. Eiichi Mizohata, Department of Applied Chemistry, Graduate School of Engineering, Osaka University, and Dr. Masaki Nojiri, Department of Chemistry, Graduate School of Science, Osaka University, for their valuable suggestions, constant discussions through this research. The author would like to express his deep gratitude to Dr. Taro Tamada, Japan Atomic Energy Agency, for his valuable discussions and enthusiastic support.

The author acknowledges to Professor Takashi Hayashi and Professor Takahiro Kozawa for reviewing this thesis and valuable discussions.

Thanks also go to Prof. Atsushi Nakagawa, Dr. Mamoru Suzuki, Dr. Masato Yoshimura and Dr. Eiki Yamashita, beamline BL44XU at SPring-8, and Dr. Naohiro Matsugaki and Dr. Yusuke Yamada, beamline BL1A at Photon Factory, for their support in the collection of X-ray data. The author would like to thank Dr. Kiyoshi Baba, Dr. Nobuhiro Mizuno and Dr. Hideo Okumura, beamline BL38B1 at SPring-8, for their support in the collection of X-ray data and measurement of microspectroscopic spectra.

Dr. Hideto Takami, Microbial Genome Research Group, Japan Agency of

Marine-Earth Science and Technology for the sample of *Geobacillus kaustophilus* HTA426 is gratefully acknowledged. The author greatly appreciate Dr. Masami Lintuluoto, Faculty of Life and Environmental Sciences, Department of Environmental Information, Kyoto Prefectural University, and Dr. Yoshifumi Fukunishi, Molecular-Recognition Structure Analysis Team, Molecular Profiling Research Center for Drug Discovery (molprof), National Institute of Advanced Industrial Science and Technology (AIST), for their support in MD simulation and valuable discussions. The author also indebted to Professor Shunichi Fukuzumi and Dr. Kei Okubo, Department of Material and Life Science, Division of Advanced Science and Biotechnology, Graduate School of Engineering, Osaka University, for their support in measurement and interpretation of EPR spectra.

The author owes a lot as well to Dr. Hiroyasu Koteishi, Laboratory for Cell Signaling Dynamics, RIKEN Quantitative Biology Center, who gave valuable suggestions and kind advices, which led the author to the right direction. Acknowledgement is also made to all members to Professor Tsuyoshi Inoue's lab (from April 2011 to March 2014) and all members to Bioinorganic Chemistry lab of Department of Chemistry, Graduate School of Science, Osaka University (from April 2011 to Oct 2012). The author furthermore offers thanks to his friends who devoted their precious time to talk and drink together to refresh him.

The studies have been financially supported by the Japan Society for the Promotion of Science (JSPS) Research Fellowships for Young Scientists.

Finally, the author owe a special debt of gratitude to his family, who deeply understand what he wanted to do but never asked too often what exactly he was doing and worrying about so that he can determine his own way all by himself.